AERODYNAMICS AND AEROSOL TRANSPORTATION IN HUMAN AIRWAYS

KWEK JIN WANG

NATIONAL UNIVERSITY OF SINGAPORE

2006

AERODYNAMICS AND AEROSOL TRANSPORTATION IN HUMAN AIRWAYS

KWEK JIN WANG

B. Eng. (Hons.) (NUS)

A THESIS SUBMITTED

FOR THE DEGREE OF MASTER OF ENGINEERING

DEPARTMENT OF CHEMICAL & BIOMOLECULAR ENGINEERING

NATIONAL UNIVERSITY OF SINGAPORE

2006

Acknowledgments

First, I would like to express my gratitude to my supervisor, A/P Reginald Tan, for providing valuable inputs to this project.

I am also grateful that Dr Zhu Kewu from the Institute of Chemical and Engineering Sciences (ICES) had guided me on the analyses of the flow field as well as the particle deposition results.

In addition, I would like to thank Mr. Samit Saha from Fluent India for his kind assistance on the initial creation of the configuration.

Last but not least, I would like to thank the Institute of Chemical and Engineering Sciences (ICES) for the computing resources that were made available to me for the CFD simulations.

Contents

List of Figures

List of Tables

Summary

A numerical study of the airflow and particle deposition in a simulated human airway system from generations G3 to G5 using Weibel's (1963) Model A was done. The bifurcation angle between one branch of G4 and G3 was varied from 20, 30 to 40 degrees. The air flow at the inlet was assumed to be inspiratory, laminar and incompressible. Using FLUENT 6.1, the inlet Reynolds numbers of 514, 1070 and 2194 were chosen to represent resting, light and moderate activities respectively. For the particle deposition analyses, the particle sizes selected were 1, 3 and 5 μm in diameter, and the particle release profiles at the inlet of G3 were monodispersed parabolic, monodispersed homogeneous and polydispersed parabolic.

The numerical model was validated with experimental results [Zhao et al, 1994] of a singly bifurcated configuration and was found to be valid. Air flow recirculation was found to occur earlier in G4 at lower Re number for configurations with larger bifurcation angle. Secondary currents in the form of primary double vortices were present in G4 branches and their intensities increased with bifurcation angle. Weak secondary double vortices were found in G5 at various Re number for different bifurcation angles. Particle deposition results showed that as Stokes number increased, significant difference could be found between configurations with bifurcation angles of 20 and 30 degrees. Polydispersed parabolic release profile would give the highest deposition efficiency (DE) at the highest Stokes number while monodispersed homogeneous release profile would give the lowest DE.

1. Introduction and Scope

It is important to have a detailed knowledge of the airflow and particle deposition in the human lungs for the risk assessment of airborne particulate pollutants in inhalation toxicology as well as for the targeted delivery of respirable drug particles in aerosol therapy. In order to have a realistic representation of the airflow and particle transport in the human lungs, an accurate geometric model of the airways is first required.

There are several geometric configurations used to approximate the human respiratory airways. By far, the most widely adopted model for studying the aerosol transport in human lungs is the Model A proposed by Weibel (1963). The repeatedly bifurcating and symmetrical model was based on "regular" features of the branching structure from the trachea to the alveoli. The airways were labeled by generation (starting from generation 0 from the trachea) and each generation was assigned an average diameter and length [Phillips et al, 1994]. Even though Weibel's work had been deemed as sketchy, his symmetrical model had been adopted universally for theoretical as well as experimental studies of the transport in human lungs. Some of the many examples that used the Weibel's Model A were the experimental studies using glass tube models [Kim et al, 1994, 1999] and the theoretical studies using singly and doubly bifurcated models [Balashazy et al, 1991, Lee et al, 1996, Zhao et al, 1997, Comer et al, 2000, 2001] on the airflow and particle deposition patterns in selected regions of the human lungs. However, these studies were based on bifurcations having a symmetrical branching angle. Anatomical studies [Sauret et al, 2002] on a lung cast and the lungs of a healthy adult male showed that the bifurcation angles in most generations had a range of values, indicating possible asymmetries in the bifurcation

angles. The geometrical asymmetries in terms of the bifurcation angles might affect the airflow and particle deposition in the human airways. In addition, most studies used a monodispersed parabolic distribution of particles for the release profile at the inlet. Different particle release profile at the inlet of the human airways might have significant effects on the particle deposition patterns in the downstream bifurcations.

In this study, we examined the effects of geometrical asymmetry on the airflow and particle deposition patterns by varying the bifurcation angle between Generation 3 and a branch of Generation 4 for doubly bifurcated configurations, and then compared the simulated CFD results of the asymmetrical configurations with the symmetrical configuration. Generations 3 to 5 were selected for the configurations as cytological studies of uranium miners revealed that lung cancers have usually developed in these generations [Balashazy et al, 2000, Health Phys.]. In addition to investigating the effects of geometrical asymmetries, various particle release profiles such as a homogeneously monodispersed particle distribution and a particle distribution with discrete particle sizes of 1, 3 and 5μm had been used to study the effects of these profiles on the particle deposition.

2. Literature Survey

The early studies on flow in bifurcations were carried out in curved tubes. These studies provide understanding on the flow characteristics through curved tubes and hence provided the first step in modeling particle transport and deposition processes in respiratory systems. However curved tubes did not serve as an accurate representation of the morphometry of the human lungs, and thus experimental as well as computational studies on single and double bifurcations were used to further our understanding on the flow development and particle transport and deposition in sections of the human lungs.

2.1 Flow in Curved Tubes

Understanding the flow characteristics through curved tubes was a first step in modeling particle transport and deposition processes in respiratory systems. Dean (1927, 1928) examined fully developed flow in a curved pipe and concluded that the fluid motion characterization depended on a dimensionless parameter known as Dean's number (κ). Flow entering a curved pipe would cause a boundary layer to develop on the wall. The boundary layer would cause the flow in the center to accelerate, hence resulting in secondary flow motion in the cross section. But Dean's analyses were only limited to small values of κ. The Dean's number, κ, was defined in the paper by Guan et al (2000) as a function of the tube cross sectional diameter, a, radius of curvature of the tube, R, and the Reynolds number at the inlet of the tube, Re:

$$\kappa = \sqrt{\frac{a}{R}}\,\mathrm{Re} \qquad (1)$$

For high Dean's numbers, the centrifugal forces were as important as viscosity and inertia [Zhao et al, 1994] and the axial velocity was a maximum near the inner wall [Agrawal et al, 1978]. This local maximum of the axial velocity near the inner wall was also observed when Synder et al (1985) showed experimentally that the skewed axial velocity first occurred near the inner wall but soon shifted outwards with increasing bend angle due to the cumulative action of the centrifugal acceleration. Soh et al (1984) observed that for high Dean's number, the axial velocity became a two-step plateau and the velocity profiles along lines parallel to the plane of symmetry were double-peaked or "m"-shaped. This was in agreement with the experimental results of Agrawal et al (1978). Secondary currents, that gradually developed into a double vortex pattern, were observed when Guan et al (2000) studied, using a computational fluid dynamics software package, the transitional character of fluid flow in a bend. The intensities of the secondary motion increased with Dean's number and the centers of the double vortices shifted towards the bounding walls.

From the ideal flow results, inertial impaction equations were derived for the calculation of particle deposition and it was found that the Stokes number and the branching angle were determining factors in the bend models [Landahl, 1950; Yeh, 1974]. The presence of secondary flows was found to cause a decrease in deposition at low Stk but an increase at high Stk. However, bend models were unable to provide information about spatial resolution of the deposition along the tube [Balashazy et al, 1991]. Hence, a bifurcation that was represented by three straight tubes connected by two curved ones was used to observe deposition in the tubes, especially at the carinal ridge.

2.2 Flow in Single Bifurcated Airways

Zhao et al (1994) used a cast of clear silicon rubber to create an idealized single, symmetric bifurcation with a well defined flow divider between the parent and the daughter branches. Detailed descriptions of the geometrical construct would be covered in section 3.1.2. Using laser Doppler anemometry and glycerine-water mixture as the working fluid, the flow velocities and their structures were examined at various sections of the bifurcation. Steady and parabolic inspiratory flow at Reynolds numbers of 518, 1036 and 2089 that corresponded to Dean numbers of 98, 196 and 395 were used at the inlet of the bifurcation. The results were examined in terms of the axial velocity profiles in the bifurcation plane, transverse to the bifurcation plane, and the secondary flow patterns that developed as a result of the curved geometry.

From the axial velocity profiles in the bifurcation plane, it was noted that for all the three Reynolds numbers, the velocity profiles followed the same trend starting with parabolic velocity distributions at the inlet, skewed profiles with maximum velocity at the inner walls of bifurcation as flow just entered the daughter branches, and ending with the velocity profiles becoming parabolic again near the outlets of the daughter branches. As the flow curved around the bend in the daughter branches, an inflection point that was caused by the adverse pressure gradient began to develop in the velocity profiles and this development of the inflection point occurred earlier in the daughter branches when the Reynolds numbers increased. Just before the daughter branches became straight, the velocity profiles assumed a shape of two-step plateaus with another maximum velocity near the outer wall of bifurcation at high Re of 1036 and 2089.

In the transverse plane to the bifurcation, the axial velocity profiles in the daughter branches eventually changed from parabolic to “m” shaped in which the velocity at the center decreased while that near the walls increased. The “m” shaped profiles occurred further downstream in the daughter branches with decreasing Re. This development of the “m” shaped profiles also allowed Zhao et al (1994) to quantify the difference in the shape of the velocity profiles between the branches. They introduced a parameter called the shape ratio (SR) that was defined as the ratio of the lowest velocity in the neighbourhood of the centerline to the highest velocity in the vicinity of the wall at a particular section in the daughter branches. The minimum SR for velocity profiles in the plane transverse to the bifurcation for both the left and right daughter branches was compared. It was found that the “m” shape was accentuated by up to 44% in the right branch than the left for high Re but for low Re, the difference was only less than 10%. This illustrated that even though the two branches were symmetrically divided from the parent branch, there was a slight difference in the flow rates even at the lowest Re. The increase in SR with decreasing Re seemed to indicate that the “m” shape was strongly dependent on Reynolds number.

Secondary flows were caused by the curved geometry. A force was required to balance the centrifugal force that was induced by the circular motion of the fluid particles and this force was provided mainly by the pressure gradient in the cross section. Fluid particles having a higher velocity would tend to turn with a larger radius and those having a lower velocity would turn with a smaller radius. Hence, fluid particles moving with small axial velocities near to the top and bottom of the branch would travel toward the outer wall of bifurcation where the turning radius was smaller. The fluid near the centerline will be moving with a higher velocity and hence

would travel to the inner wall of bifurcation where the turning radius was larger. This would induce the skewness of the axial velocity profiles as described earlier in the daughter branches. The magnitude of the secondary velocities was observed to be decreasing with a decrease in Reynolds number. Symmetric vortices were also observed in the daughter branches at all Re.

2.3 Factors Affecting Particle Deposition in Single Bifurcated Airways

Although the study done by Zhao et al (1994) did not base his experimental construct on any realistic sections in the lungs, the flow features that developed have important implications on the particle deposition patterns. The presence of vortices, for example, can cause the particles to be pulled away from their centres and deposit on the wall. These flow features and the particle deposition can, in turn, be affected by varying geometrical construct, inlet velocity profile, the Reynolds number, and the particle Stokes number. Cai et al (1988) used the concept of stop distance and interception distance of a particle in the cross-section of the daughter tube to calculate the inertial and interceptional deposition of spherical particles and fibers in a single bifurcation. They postulated that as airflow makes a turn at the transition from parent to daughter branch, the aerosol particles could not follow the streamlines due to inertia and only those particles within the component of the stop distance normal to the wall of the daughter tube will deposit on the wall. Both uniform and parabolic flow profiles were used at the inlet to the parent branch and the branching angle was initially set at 35 degrees. From their theoretical calculations, they found that as the branching angle increased, the particle deposition also increased. Besides the dependence of deposition on branching angle, they also found that deposition increased with increasing Stokes

number and that both the daughter to parent tube diameter ratio and the entrance velocity profile can affect the particle deposition efficiency. However, secondary flow effects were not considered in the works of Cai et al (1988). Furthermore, Lee et al (1992) found in their three dimensional numerical studies that secondary flows, branching angle, geometry, inlet velocity profile and Reynolds number affected the particle deposition. The increase in deposition was significantly noticeable with large branching angles such as 60 and 90 degrees and they attributed this effect to flow circulations and secondary flows.

Balashazy et al (1991) developed a three dimensional single and symmetric bifurcated theoretical model of the human lung based on the symmetrical Model A of Weibel (1963) to study the effect of airway variability and asymmetry on the particle deposition in the human lung. They defined the “effective” branching angle as the angle between dividing streamlines rather than between the longitudinal axes of the parent and daughter branches. The effect of the airway branching angle upon the particle deposition was compared to the experimental data of Kim and Iglesias (1989a) in the following figure.

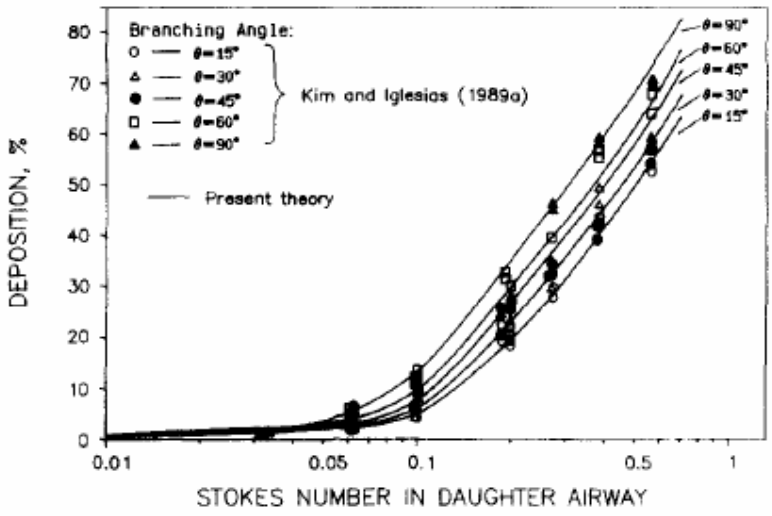

Fig. 2.1: Deposition efficiency as a function of the Sotkes number for different branching angles [Balashazy et al, 1991]

From the theoretical results, it showed that there was only slight dependence of branching angle on the deposition. Branching angle variations did not significantly affect particle deposition efficiencies, except when small diameter ratios and high inspiratory flow rates were involved. However, it was found that varying the diameter ratio between the daughter and the mother branches had significant effects on the particle deposition especially at high flow rates. In addition, Stokes number was found to be the most important factor for deposition.

Kim et al (1994) experimentally created several Y-shaped single and symmetric bifurcation glass tube models. One of the purposes of the experiments was to investigate the deposition characteristics with varying branching angle, daughter to parent tube diameter ratio and local obstruction. The branching was symmetric and the branching angle was 30 and 45 degrees. Monodisperse oleic acid droplets tagged with uranine were generated by an orifice aerosol generator and the flow used was between laminar and transitional with Reynolds in the range of 566 and 3397. It could

be seen in the following figure that particle deposition efficiency values increased monotonically with Stk but the deposition efficiency was essentially identical, indicating that the branching angles apparently had no significant effect on the deposition efficiency.

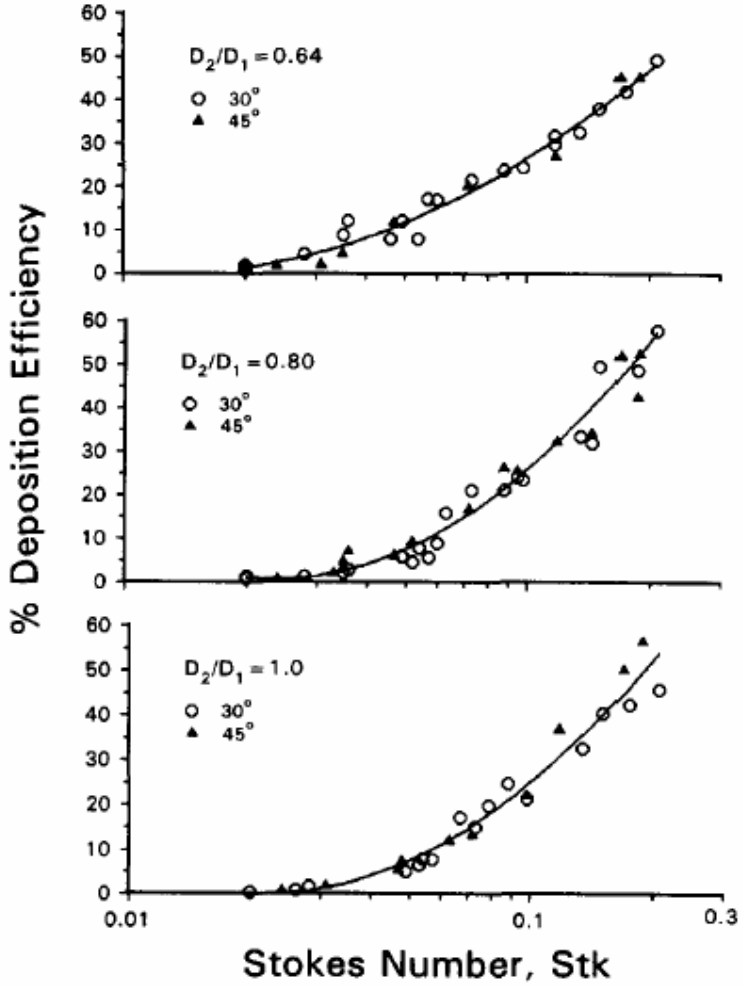

Fig. 2.2: Comparison of deposition efficiencies between 30° and 45° branching angle for models with different daughter to parent tube diameter ratios [Kim et al, 1994]. Each symbol represents a single data point.

However, if different diameter ratios (DR) between parent and daughter branches were used, deposition efficiencies for the diameter ratio of 0.64 showed considerable deviation from those of larger DR (0.8 and 1.0). Deposition efficiency was greater in configurations with obstructions than those without.

As described above, all the authors agreed that the particle Stokes number can affect the particle deposition significantly. However, there were discrepancies in whether the branching angle will affect the particle deposition significantly. Cai and Lee argued that theoretically the branching angle was important in particle deposition but Cai ignored secondary flow effects. On the other hand, Balashazy and Kim suggested that the branching angle was minimal in affecting the particle deposition besides Stokes number. Kim even added that even though theoretical studies had shown branching angle to be important in particle deposition, experimental results showed a good correlation of deposition efficiency with Stk alone in spite of a wide variation of branching angle and pattern. But we should take note that both Kim and Balashazy varied the branching angles of both the daughter tubes and in our studies, we varied only the branching angle of one of the daughter tubes. Kim suggested that the airway branching system *in vivo* was complex and the branching might not be symmetrical as perceived. Horsfield et al (1967) reported that the branching angle of the human airways had been in the range of $10 - 90^{o}$ with an average of $30 - 40^{o}$ in the large airways. Furthermore, the configuration we adopted for our study was double bifurcated.

2.4 Double Bifurcated Airways

Kim et al (1999) made sequential double bifurcating glass tubes so as to study the deposition characteristics of aerosol particles in a physiologically realistic model. The dimensions of the configurations were modeled after the third to fifth generation human bronchial airways as described by Weibel (1963). They used two geometric models in which one model (Model B) had its first bifurcation 90^{o} out of plane with the second bifurcation while the other geometric model (Model A) had its first

bifurcation that was in the same plane as the second bifurcation. Both symmetric and asymmetric flow ratios were generated in the first bifurcation for both models.

They showed that with increasing Stokes number, the deposition efficiencies increased accordingly and it could be fitted with modified logistic functions. When the flow was symmetric in both bifurcations, the deposition efficiency (DE) was smaller in the second than the first bifurcation in the symmetric model. It was suggested that the cause for the smaller DE was probably due to the skewed axial velocity profiles toward the inner wall in the daughter tubes. Particles having high inertia would move away from the carina at the second bifurcation. Furthermore, the axial velocity profile on the vertical plane was lowest in magnitude in the central region in the 'M' shape and this would cause the particles' inertia to weaken upon approaching the carina. However, with the 90^{o} out of plane model B, DE was almost similar between the first and second bifurcation as particles could not veer away from the carina at the second bifurcation. Secondary flows might change the particle distribution patterns by redirecting particles towards regions with high probability of impaction or by decreasing particle deposition in asymmetric flows. They also showed that with asymmetric flows, DE was higher in the low-flow side as compared to the high-flow side at low Stk and it was higher in the high-flow side as compared to the low-flow side at high Stk. Highly localized deposition was seen to be on and in the immediate vicinity of the bifurcation ridge for a wide range of Stk numbers.

Comer et al (2001) used the experimental models of Kim (1999) to simulate the airflow and particle deposition patterns for double bifurcated configurations at both low and high Re numbers. The configurations were based on Weibel's (1963)

symmetric lung model from Generations 3 to 5. They also explored the differences in the flow structures with rounded and sharp bifurcation transition ridges. Steady, incompressible and laminar parabolic flow was specified at the inlet of G3 with Reynolds number of 500 and 2000. For the particle deposition studies, the inlet particle release profile was parabolic and monodispersed with particle diameters ranging from 3 to 7 μm.

In the bifurcation plane, Comer noted that there was a distinct shear layer along the inner wall after the first carina and this layer would get thinner at high flow rate. In addition, a recirculation zone was observed at the outer wall where it got larger with flow rate. As the flow began to enter the first bifurcation, the highest axial velocity was next to the inside wall of bifurcation while the secondary flow structure was in the form of a main vortex which moved the high speed flow around the top of the branch to the outside of bifurcation and the low speed flow from the outside of the bifurcation along the symmetry plane to the inside of the bifurcation. At higher Re number, a secondary vortex could be seen near the outside of the bifurcation. As the flow progressed downstream in the first bifurcation, the stronger secondary flow for the high Re number had wrapped the high velocity flow around the outside of the tube engulfing the slow moving fluid and pushing it to the tube centre, hence resulting in a double peak axial flow profile. The flow for the lower Re number did not show the axial double peak velocity profile due to the relatively weaker secondary flow. The presence of the vortex would push the particles toward the walls of the bifurcation and with the increase in the Re numbers, the particles would be pulled away from the vortex centres, generating distinct particle-free zones in the branch central region.

As the flow entered the second bifurcation in the lateral branches, the maximum axial velocity had shifted back to the centre of the bifurcation at low Re numbers but at high Re numbers, it wrapped itself around the top/bottom of the branch. In the median branches, the maximum axial velocity was located off the symmetry plane near to the top and bottom of the bifurcation at both low and high Re number. A narrow secondary vortex also started to appear on the outside of the second bifurcation and this was a result of the upstream flow field, the bifurcation curvature or the Dean's effect, and the effect of the carinal ridge shape. The intensity of the primary and secondary vortices was stronger in the median branches than the lateral ones. As the flow progressed further downstream in both the lateral and median branches, the maximum velocity region continued to shift back toward the centre of the daughter tube at low Re number but it remained around the top of the daughter tube at high Re number. The presence of the secondary vortex can also be seen in the cross sectional particle flow distributions as two distinct vortex regions can be seen in the median branches. Fontana et al (2005) also reported the presence of secondary vortices in his simulation of his double bifurcation.

Besides the co-planar configuration, Comer et al (2001) also created a configuration that had its second bifurcation 90^{o} out of plane with the first bifurcation. The main differences in the flow structures between these two configurations were that the flow field was not symmetric about the bifurcation plane and strong axial and secondary flows were formed near the bottom of the second daughter tube instead of the tube centre. The effect of the carinal ridge shape on the flow structures was found to be insignificant in both configurations.

Although both Comer and Kim did extensive computational and experimental works on the flow and particle transport in double bifurcations, their configurations were geometrically symmetric about the first bifurcation. Since most bronchial bifurcations were somewhat symmetric as suggested by Horsfield et al (1971) and Phillips et al (1997), there might be an effect of the geometric asymmetry on the flow structures and particle deposition. Furthermore, there were no available studies that examined the effect of geometric asymmetry. Therefore, it would be interesting to investigate the effect of geometric asymmetry and in addition, the effect of different particle release profile at the inlet on the flow structures and particle deposition patterns.

3. Modeling

3.1 Geometric Modeling

In this work, symmetrical and asymmetrical configurations of the human lungs in Generations 3 to 5 were constructed. The asymmetry in the configurations referred to the bifurcation angle between the mother branch G3 and one of the daughter branches in G4. The motivation and details for the construction of the symmetric and asymmetric configurations would be discussed. Next, details on the construction of a symmetric, singly bifurcated configuration with the dimensions as stated by Zhao et al (1994) for numerical validation would be elaborated. Certain planes and profiles that were critical for the analyses of the air flow fields and particle deposition patterns would then be defined.

3.1.1 Configurations for Generations G3 to G5

The human lungs can be regarded as a complex network of repeatedly bifurcating tubes having dimensions and flow rates in a decreasing fashion [Weibel 1963]. Generations G3 to G5 as found in Weibel's classification scheme were used in the geometrical configurations. The symmetrical configurations were also used in the experimental glass tube models utilized in Kim et al (1999) and also later used in the flow and particle deposition simulations of Comer et al (2000, 2001).

Only smooth and rigid wall configurations were considered since cartilaginous rings, often present in the larynx and trachea, hardly protruded into the airway lumen from G3 onwards [Kleinstreuer, C., 2001]. Asymmetries at the bifurcation of G3 to G4 were modeled for different bifurcating angles to investigate the effects of the

branching angle asymmetries on the flow and particle deposition both in the vicinity of the bifurcation and the bifurcations downstream. The construction of the asymmetrical and the symmetrical configurations was based on the symmetrical configuration as illustrated in detail by Comer et al (2001). Descriptions of the construction of both the symmetrical and asymmetrical configurations were given in the following paragraphs.

Previous studies had focused on constructing a physiologically correct bifurcation model for various generations in the human lungs. In a study by Sauret et al (2002), computed tomography (CT) images of both the human tracheobronchial tree cast and a healthy male volunteer were measured for the length, diameter, gravity, coronal and sagittal angles for various generations. Sauret defined the trachea as generation 1 and since our definition of the trachea was generation 0, generation 3 would be generation 4 in Sauret's model, generation 4 would be generation 5 and so on. The following figure illustrated the results of the measurements made for the branching angle from generation 2 to generation 9. In this study, we were interested in the branching angle corresponding to generation 5 as indicated by the arrows in the figure.

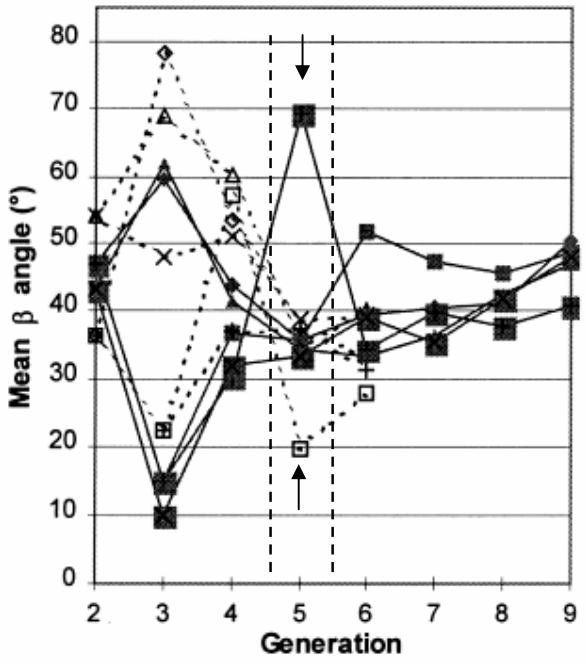

Fig. 3.1: Mean branching angle per generation. "Closed/open diamonds": Cast/Volunteer right upper lobe. "Closed/open squares": Cast/Volunteer right middle lobe. "Closed/open crosses": Cast/Volunteer right lower lobe. "Closed/open triangles": Cast/Volunteer left upper lobe. "Closed/open X's": Cast/Volunteer left lower lobe. The solid lines link the cast data, the dashed lines link the volunteer data. [Sauret et al, 2002].

The branching angle defined by Sauret was the angle formed between the parent airway direction and the studied airway direction. From the above figure, most of the points for the mean branching angle at Generation 5, corresponding to Generation 4 in our studies, were from 20 degrees to about 40 degrees, with only one point at 70 degrees.

In another study by Yeh et al (1980), the branching angle corresponding to Generation 4 was given as 20 degrees. Comer et al (2001) gave the branching angle between G3 and G4 as 30 degrees for the symmetrical configuration. Hence, in our study, we would vary the bifurcation angle of one branch at G3 to G4 from 20, 30 to 40 degrees respectively while keeping the bifurcation angle of the other branch at G3 to G4

constant at 30 degrees. This would produce two asymmetrical configurations of bifurcation angles 20 and 40 degrees and one symmetrical configuration of bifurcation angle of 30 degrees.

The asymmetrical and symmetrical configurations were generated and meshed using a commercially available pre-processor package GAMBIT 2.0.4. The dimensions and method involved in creating the configurations were adopted and modified from Comer et al (2001). Basically, the straight sections of the parent branch of G3 and daughter branches of G4 and G5 were cylinders of constant cross sections. After the parent branch was constructed, bifurcation radii of curvatures and bifurcation angles were defined so as to define the transition geometries connecting the parent branch to the daughter branches. The method critical in defining the transition geometries was illustrated in Comer et al (2001) in detail. It involved defining a conic face with modified dimensions. The symmetric configuration with a bifurcation angle of 30 degrees between G3 and G4 was labeled as C1. The asymmetric configurations having bifurcation angle of 20 and 40 degrees between G3 and one branch of G4 were labeled as C2 and C3 respectively. The following figures and table illustrated the construction of the configurations and their respective dimensions.

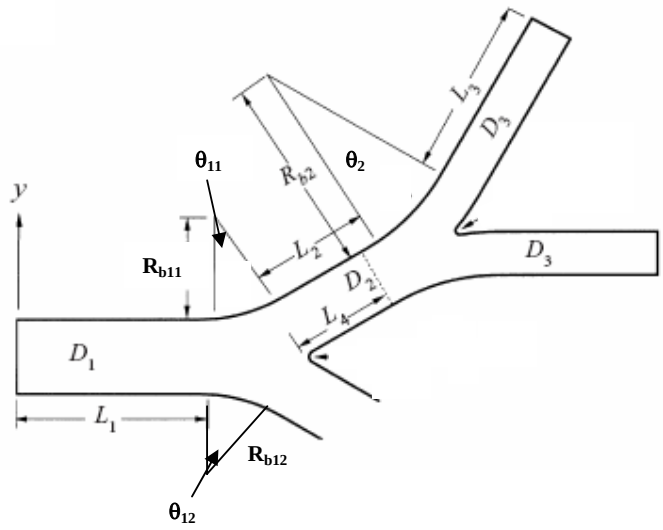

Fig. 3.2: Definition of geometrical parameters at the symmetry plane (z = 0) [Comer et al, 2001].

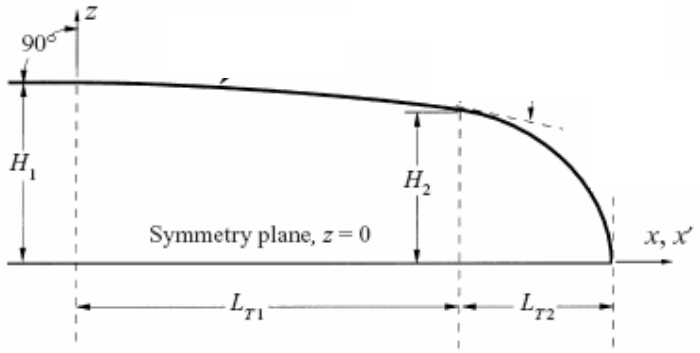

Fig. 3.3: Bifurcation symmetry plane [Comer et al, 2001].

Table 3.1: Geometric parameters for various models.

Parameter	**C1**	**C2**	**C3**
G3 Diameter, D_1 (cm)	0.6	0.6	0.6
G4 Diameter, D_2 (cm)	0.5	0.5	0.5
G5 Diameter, D_3 (cm)	0.35	0.35	0.35
G3 Length, L_1 (cm)	2.4	2.4	2.4
G4 Length, L_2 (cm)	0.836	0.836	0.836
$G5^+$ Length, L_3 (cm)	0.437	0.437	0.437
Extent of daughter tube for 1st bifurcation deposition calculations, L_4 (cm)	0.6	0.6	0.6
G3-G4 bifurcation angle, θ_{11} (degrees)	**30**	**20**	**40**
G3-G4 bifurcation angle, θ_{12} (degrees)	30	30	30
G4-G5 bifurcation angle, θ_2 (degrees)	30	30	30

G3-G4 bifurcation radius of curvature, R_{b11} (cm)	1.35	3	1.013
G3-G4 bifurcation radius of curvature, R_{b12} (cm)	1.35	2	1.35
G4-G5 bifurcation radius of curvature R_{b2} (cm)	1.645	1.645	1.645
G3-G4 carinal transition region length L_{T1}, L_{T2} (cm)	0.55, 0.25	0.64, 0.25	0.55, 0.2
G4-G5 carinal transition region length L_{T1}, L_{T2} (cm)	0.45, 0.15	0.45, 0.15	0.45, 0.15
G3-G4 carinal ridge height, H_1, H_2 (cm)	0.6, 0.2	0.6, 0.255	0.6, 0.2
G4-G5 carinal ridge height, H_1, H_2 (cm)	0.5, 0.1	0.5, 0.1	0.5, 0.1

Curved edges were created to connect the parent branch to the daughter branch at G3 to G4, circular faces of radii 0.25 cm were defined at the end face of the parent branch and then swept along the curved edges to generate curved tubes. The conic face defined at G3-G4 was rotated around the x-axis to generate a volume. The conic volume and the curved tubes were boolean united to form the final transition volume at G3-G4. The same procedures were adopted for G4-G5.

Since geometry was complex at the bifurcation, the models were meshed using the unstructured tetrahedral meshing scheme with an interval size of 0.05 to fulfill an absolute minimum of 10,000 to 15,000 elements per bifurcation [Nowak et al, 2003].

3.1.2 Configuration for Model Validation

In order to validate the numerical model used, configuration for model validation was constructed. The experimental flow results of a single and symmetric bifurcating configuration in an article by Zhao et al (1994) were used for the model validation. The singly bifurcated configuration consisted of a cylindrical parent branch and its two daughter branches joined together by a flow divider. The flow divider basically

consisted of curved tubes with two different bifurcation radii of curvature and bifurcation angles. The total bifurcation angle for each daughter branch was 35 degrees. The geometrical configuration was meshed using the unstructured tetrahedral scheme with an interval size of 0.05. The following table and figure summarized the airway parameters and the geometrical configuration used for numerical model validation:

Table 3.2: Airway parameters for the validation configuration.

Model	Validation Configuration
Total Bifurcation Angle (degrees)	35
Length of G3, L_{G3} (cm)	6.668
Radius of G3, R_{G3} (cm)	1.905
1st Bifurcation Radius of Curvature, R_1 (cm)	11.18
1st Bifurcation Angle, θ_1 (degrees)	20
2nd Bifurcation Radius of Curvature, R_2 (cm)	17.511
2nd Bifurcation Angle, θ_2 (degrees)	15
Length of G4, L_{G4} (cm)	2.54
Radius of G4, R_{G4} (cm)	1.347

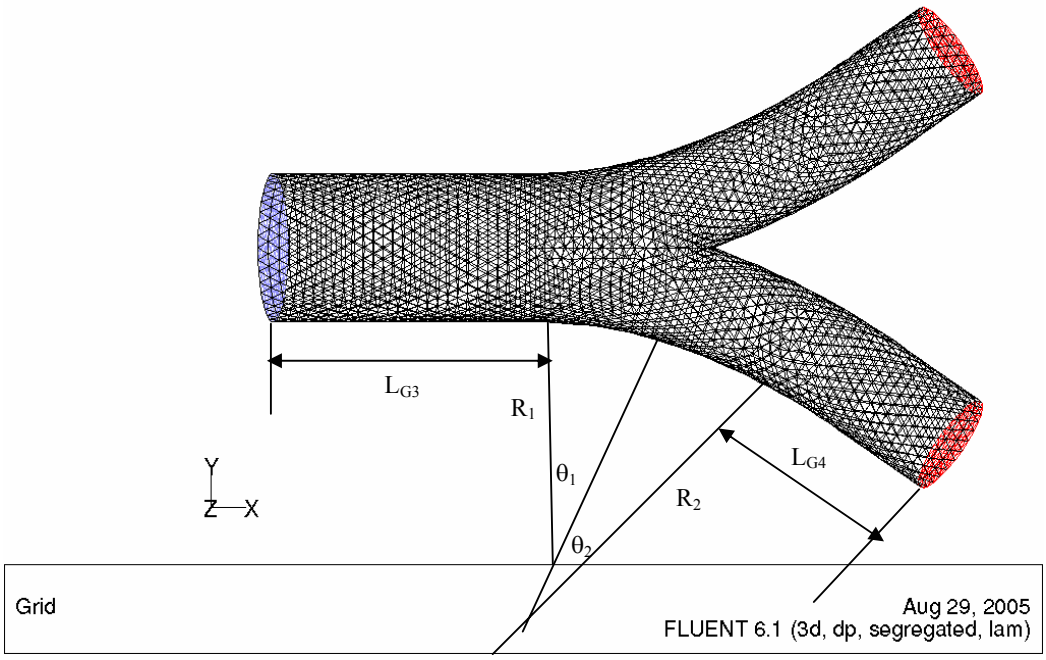

Fig. 3.4: Geometry of the validation model and its dimensions.

3.1.3 Planes and Profiles Defined

For the analysis of air flow fields and particle deposition patterns, planes and profiles were defined in FLUENT 6.1 at the beginning of the transition from G3 to G4, at the beginning and end of each branch of G4, and at the beginning of the branches in G5. The labeling of the planes and profiles was in accordance to the generation in which the plane or profile was in first, then the branch in which the plane or profile was located and finally the order in which the plane or profile existed in that branch. For example, G4-1-1 referred to the plane or profile in Generation 4, located in the affected branch in G4 where the angle of bifurcation was varied, and was the first defined plane or profile in that branch. The following diagram illustrated, for C1, the locations of the planes and profiles defined:

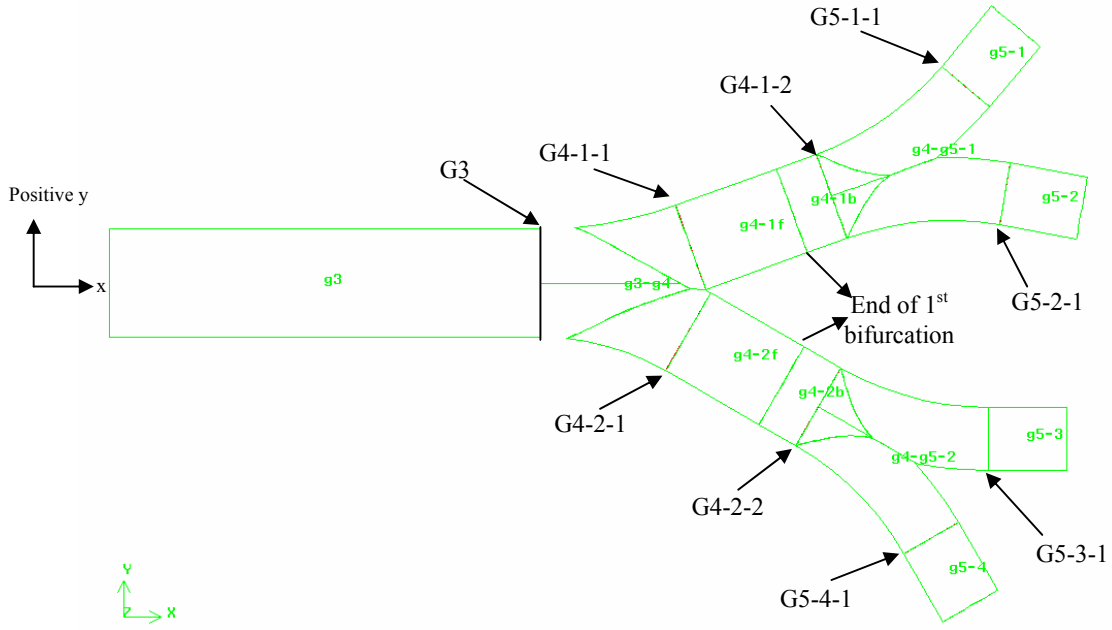

Fig. 3.5: C1 and the location of the defined planes and profile.

For the model validation configuration, profiles 2-2', 10-10' and 15-15' were defined at 1.905 cm from the inlet, at the beginning of curvature of G4 and at the end of the curvature of G4 respectively.

3.2 Numerical Modeling

In this section, the flow and particle transport equations used in the CFD simulations would be given. Next, details on the flow conditions, flow modeling and discrete particle modeling would be described.

3.2.1 Theory

The continuity and momentum equations for steady laminar incompressible air flow were given as [Comer et al, 2001]:

$$\nabla \cdot v = 0 \qquad \text{--- (2)}$$

$$(v \cdot \nabla)v = -\frac{1}{\rho}\nabla p + \nabla \cdot [v(\nabla v + (\nabla v)^{tr})] \qquad \text{--- (3)}$$

The deposition efficiency, DE (%), was defined as the ratio of the number of particles deposited in a given region to the total number entering the region. The motion of particles was governed by the Newton's Second Law [Comer et al, 2001]:

$$m_p \frac{dv_p}{dt} = \sum F_p \qquad \text{--- (4)}$$

m_p was the mass of one spherical particle, d_p was the particle diameter in the range of 1 to 5μm, and ΣF_p was the sum of forces acting on the particle. Since the particles were relatively large, Brownian motion and rarefied gas effects were neglected. The density of the particle ($1 g/cm^3$) was larger than air and thus the pressure force and buoyancy force were small. As explained in Comer et al (2001), the Magnus lift and the shear-induced (Saffman) lift force can be neglected due to the particles were not spinning rapidly and the shear fields were weaker for laminar flows than turbulent flows.

The particle trajectory equation was given as [Comer et al, 2000]:

$$m_p \frac{d^2 x_p}{dt^2} = \frac{1}{8}\pi\rho {d_p}^2 C_{Dp}(v - v_p)\left|v - v_p\right| \quad \text{--- (5)}$$

$$C_{Dp} = C_D / C_{slip} \quad \text{--- (6)}$$

$$C_D = \frac{24}{\mathrm{Re}_p} \quad (\text{for } 0.0 < \mathrm{Re_p} \le 1.0) \quad \text{--- (7)}$$

$$C_D = \frac{24}{\mathrm{Re}_p^{0.646}} \ (\text{for } 1.0 < \mathrm{Re_p} \le 400) \quad \text{--- (8)}$$

$$\mathrm{Re}_p = \frac{\rho\left|v - v_p\right| d_p}{\mu} \quad \text{--- (9)}$$

The Cunningham slip correction factor, C_{slip}, was given as [Hinds, W.C., 1982]:

$$C_{slip} = 1 + \frac{2}{Pd_p}\left[6.32 + 2.01\exp(-0.1095 Pd_p)\right] \quad \text{--- (10)}$$

where P was the atmospheric pressure.

The particle Stokes number, Stk, was defined as [Comer et al, 2001]:

$$Stk = \frac{\rho_p {d_p}^2 \mathrm{Re}}{18\rho {D_{G3}}^2} \quad \text{--- (11)}$$

ρ_p was the particle density which was set at 1g/cm^3, Re was the Reynold's number based on the diameter of G3, ρ was the air density at 25 ^{0}C, and D_{G3} was the diameter of G3 at 0.6cm.

3.2.2 Flow Conditions

A parabolic fluid velocity profile was defined at the inlet of G3 for steady laminar inspiratory flow. Inspirational Reynolds numbers of 514, 1070 and 2194 were chosen at G3 inlet as it corresponded to resting, light and moderate activities [Zhang et al, 2002]. The density, ρ, and the viscosity, μ, of air was given as 1.225kg/m^3 and 1.7894x10^{-5} kg/m.s respectively. The mean inlet velocity, u, at G3 was calculated from the pre-determined Re and the fluid properties:

$$u = \frac{\mathrm{Re} \times \mu}{\rho D_{G3}} \qquad \text{--- (12)}$$

Constant outlet pressure boundary conditions were specified at the outlets while non-slip boundary condition was specified at the walls.

For the flow conditions in the numerical model validation [Zhao et al, 1994], glycerine-water mixture of kinematic viscosity 6.3x10^{-6} was used and a parabolic velocity profile of Re=1036 was chosen. Also, constant outlet pressure boundary conditions at the outlets and non-slip boundary condition at the walls were specified.

3.2.3 Flow Modeling

A commercial CFD code using finite volume method, FLUENT 6.1, was used to solve the Navier-Stokes and the continuity equations. The SIMPLEC algorithm was used with under-relaxation of 0.65 for the flow equations. Comer et al (2001) used hybrid differencing to model the convective terms of the transport equations and

compared the simulation results of this scheme to the QUICK scheme. It was found that the differences in terms of the relative velocity magnitudes were below 10%. In our study, the QUICK scheme was used. The steady state solution for the flow field was assumed to be converged when the dimensionless mass residual, (total mass residual)/(mass flow rate), was less than 0.001. All computations were carried out on HPX4000 workstation with Intel Xeon 2GHz and 3.8GB RAM. Run times for the computations ranged approximately from 2 to 3 hours. The mesh was refined using the velocity gradient adaption scheme after each convergence till the flow solutions were independent of the number of grid cells.

3.2.4 Discrete Particle Modeling

Spherical monodispersed particles of diameter 1, 3 and 5μm and of density 1g/cm^3 were released from the inlet of G3. The particle sizes chosen were representative of standard pharmaceutical aerosols with diameters varying from 1 to 7μm [Ertbruggen et al, 2005]. In Comer et al (2001), the particles simulated had a parabolic distribution across ½ of the model inlet and the bifurcations were symmetrical about z=0. In our study, we used a monodispersed parabolic particle release profile at the inlet and a monodispersed homogeneous particle release profile at the inlet to see the effects of these three particle release profiles on the particle deposition efficiencies and patterns. In addition to these monodispersed distributions, polydispersed parabolic distributions with discrete numbers (1/3 for each particle size) of particles having mean diameters of 1, 3 and 5μm was used. The different profiles were illustrated in the following figures.

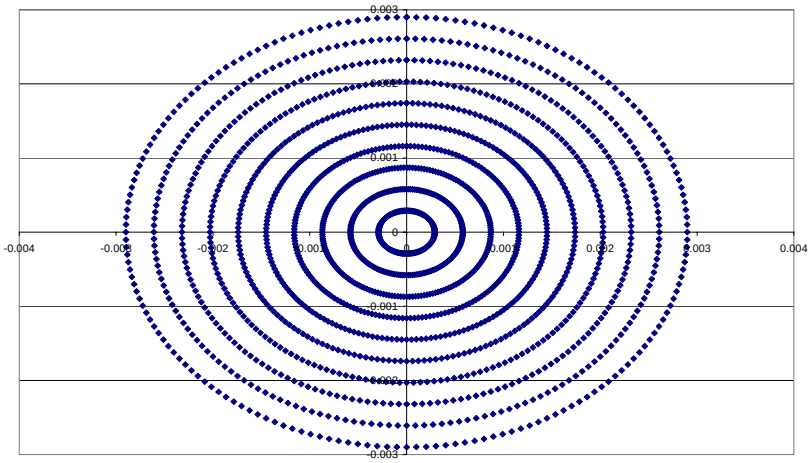

Fig. 3.6 Parabolic release profile for monodispersed as well as polydispersed (discrete numbers of various particle mean diameters) distributions.

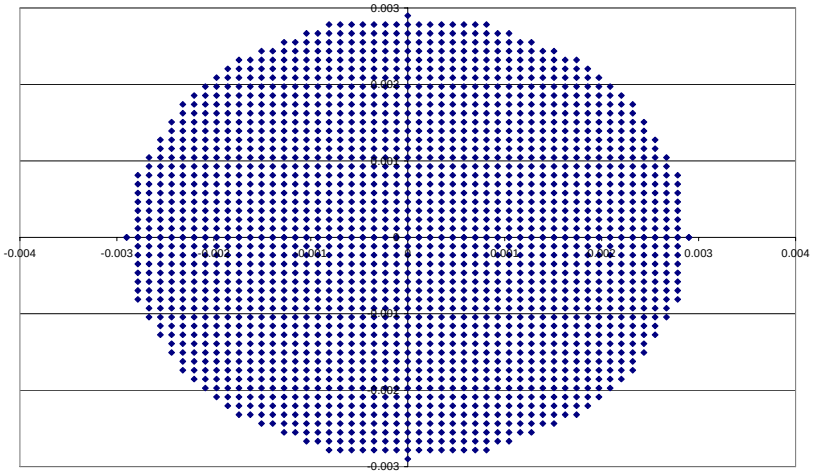

Fig. 3.7 Homogeneous release profile for a monodispersed distribution.

For the monodispersed parabolic release profile, the number of particles located at the center of G3 was equal to that located near the wall of G3. The number of particles used at the inlet was determined by increasing the inlet particle concentration until the overall deposition efficiency became independent of the number of particles simulated. The overall particle deposition efficiency (DE) was defined as the percentage of total number of particles trapped over the total number of particles

entering G3. The determination of the final number of particles for each particle release profile was illustrated in the following figures.

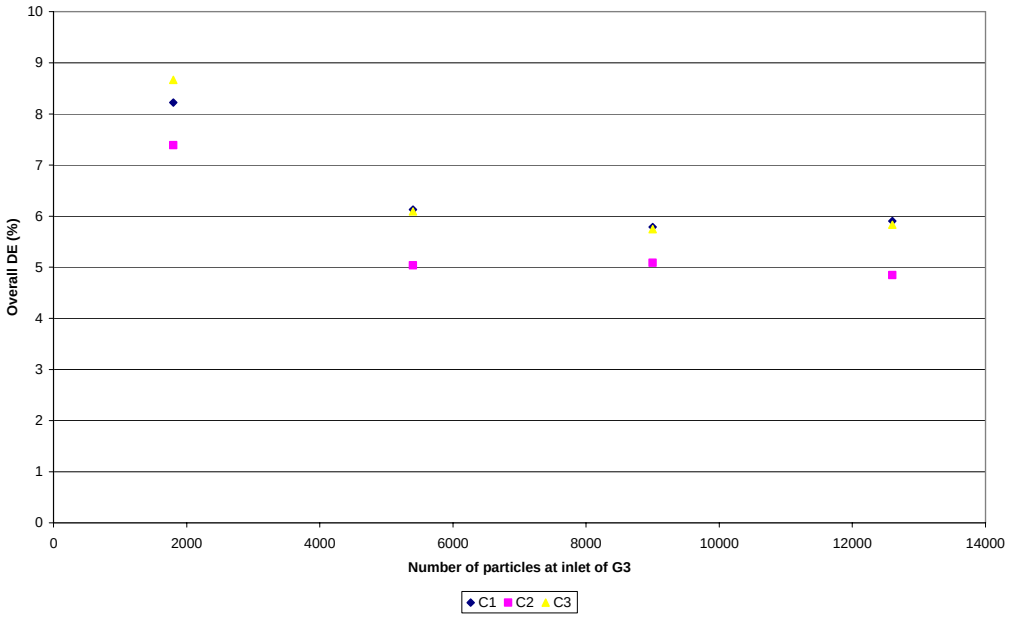

(a)

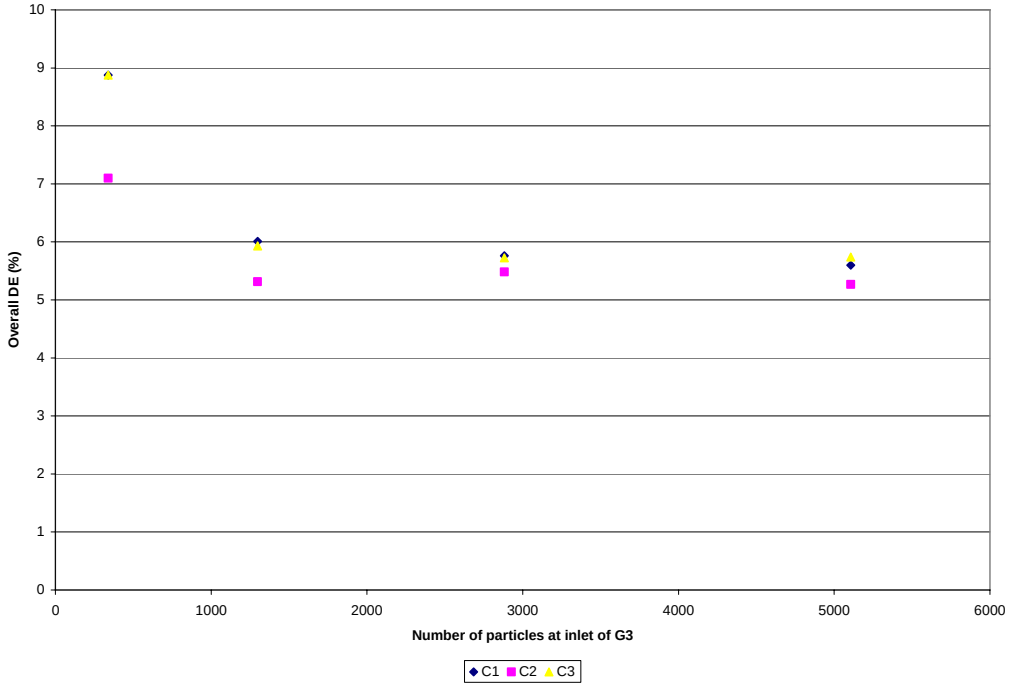

(b)

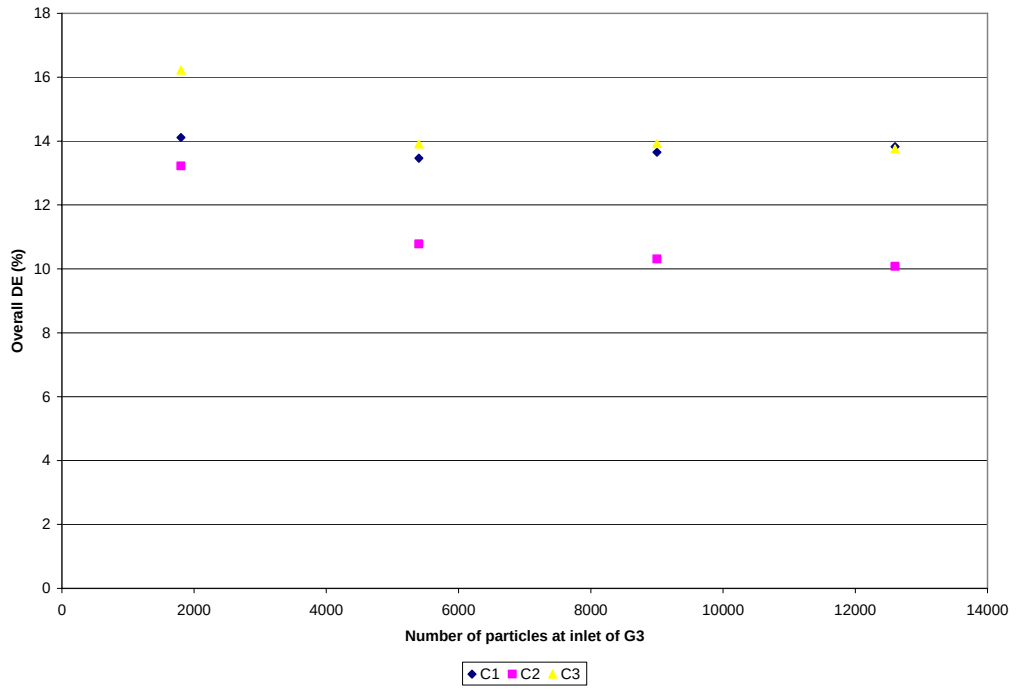

(c)

Fig. 3.8: Determination of the final number of particles to be used for the (a) monodispersed parabolic particle release profile, (b) monodispersed homogeneous particle release profile, and (c) polydispersed parabolic particle release profile at inlet of G3. The results here were based on Re = 2194 and a mean particle diameter of 1μm for the monodispersed distribution.

From the above figures, it was clear that the deposition efficiency had reached a constant after a certain number of particles and hence became independent of the number of particles used in the simulation. The final number of particles used for the monodispersed parabolic profile was 9000, that of the monodispersed homogeneous profile was 2882, and that of the polydispersed parabolic profile was 9000. The number of particles for each mean particle diameter (1, 3 and 5μm) was 3000 for the polydispersed, discrete parabolic profile.

Particle deposition was simulated at the walls by setting the discrete phase boundary conditions at the walls to "trap". The calculated Cunningham correction factor, C_{slip},

was entered for every particle size simulated and the number of iteration steps was fixed at $1.0x10^6$.

3.3 Grid Independence Study

The mesh was refined for each model using the velocity gradient adaption scheme such that more cells were in the vicinity of the walls of the geometry as shown in the following figure for C2.

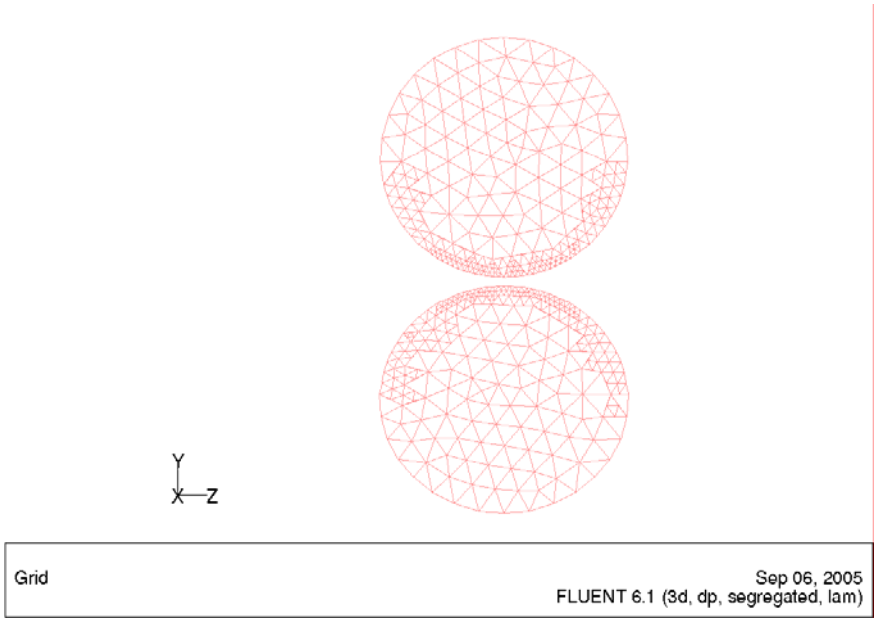

Fig. 3.9: Refined mesh of C2 where more cells were added close to the wall.

This refinement continued until the flow field solutions and the particle deposition efficiency became independent of the number of cells used. The axial velocity profile at g4-1-1 was selected for the flow field solutions comparison for each refinement. Both the position of the node and the flow velocity were normalized with respect to radius, R, of G4, and mean inlet velocity, U, at G3 respectively. The initial number of particles released at the inlet of G3 was 1810 and the profile was parabolic. Grid independence was achieved when the number of cells for C1, C2 and C3 were

859031, 833270 and 874160 respectively. The following diagrams showed the flow field solutions at g4-1-1 for C2 at Re = 514 for each adaption and the overall deposition efficiency for C2 at Re = 514 with each adaption.

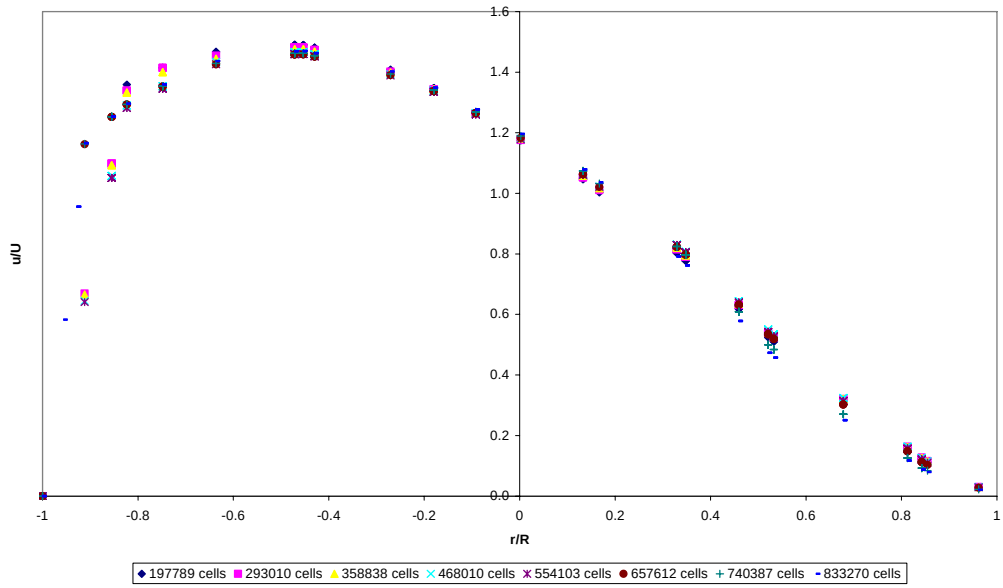

Fig. 3.10: Axial flow field solutions at g4-1-1 for C2 at Re = 514.

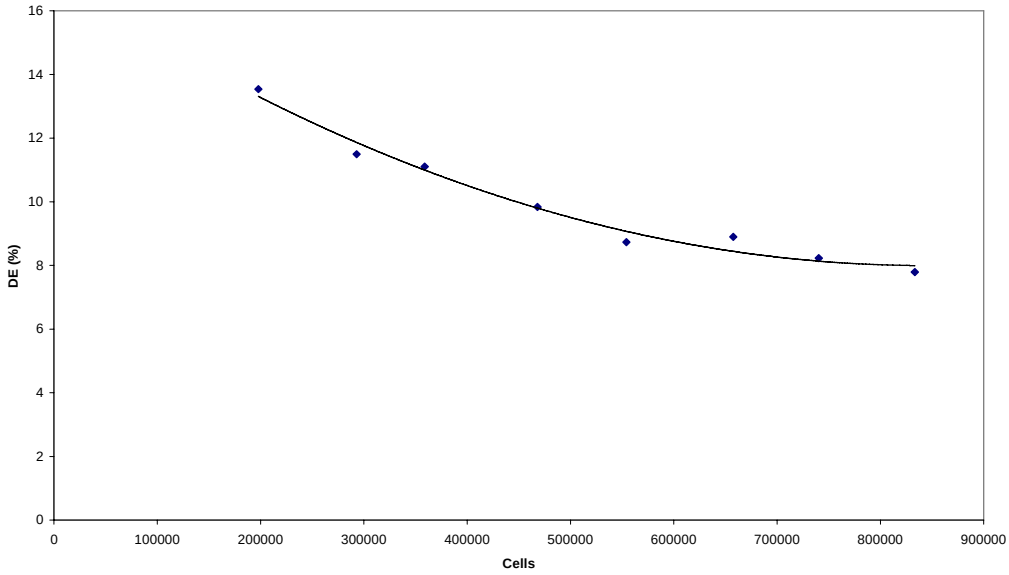

Fig. 3.11: Overall deposition efficiency for C2 at Re = 514.

The following figures showed the grid independence study of the geometry used for the numerical model validation at 2-2' and 10-10' for Re = 1036.

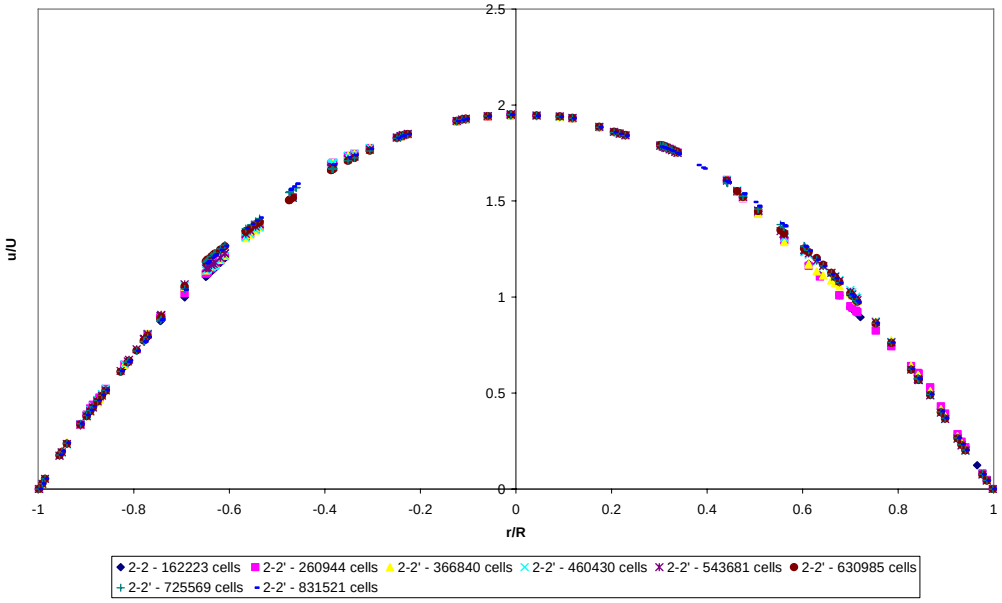

Fig. 3.12: Axial flow solutions at 2-2'of model validation geometry at Re = 1036.

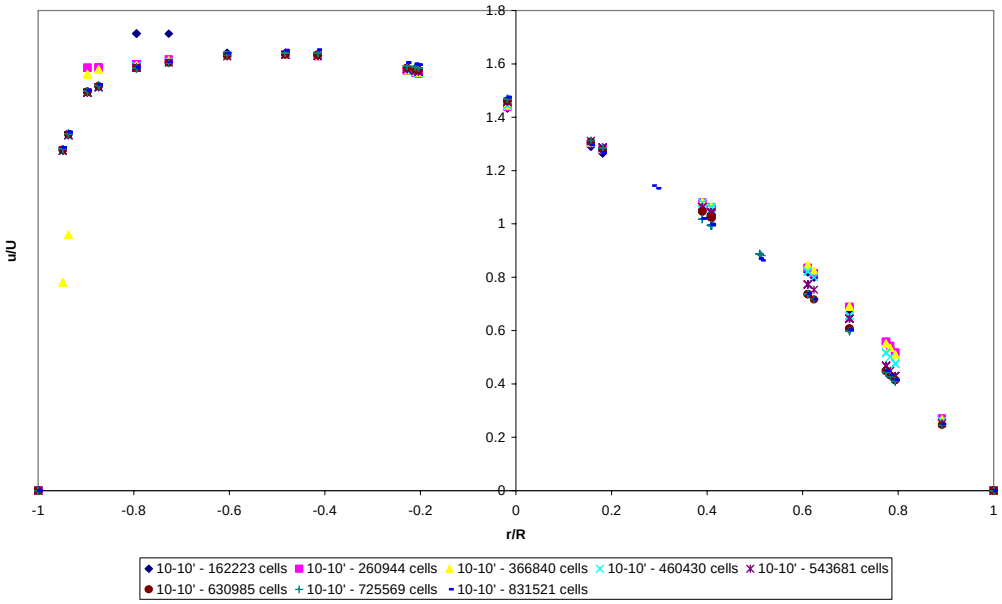

Fig. 3.13: Axial flow solutions at 10-10'of model validation geometry at Re = 1036.

4. Results and Discussions

4.1 Model Validation

The numerical model had been validated with the experimental axial velocity profiles in the plane of bifurcation (x = 0). Three profiles in the geometrical model were selected for the validation. They were cross sections 2-2', 10-10' and 15-15' located at 1.905cm from the inlet, at the beginning of the curvature of the right daughter branch, and at the end of the curvature of the right daughter branch respectively. The following figures illustrated the comparison between the simulated results and the results of Zhao et al (1994), and the simulated results of Comer et al (2001).

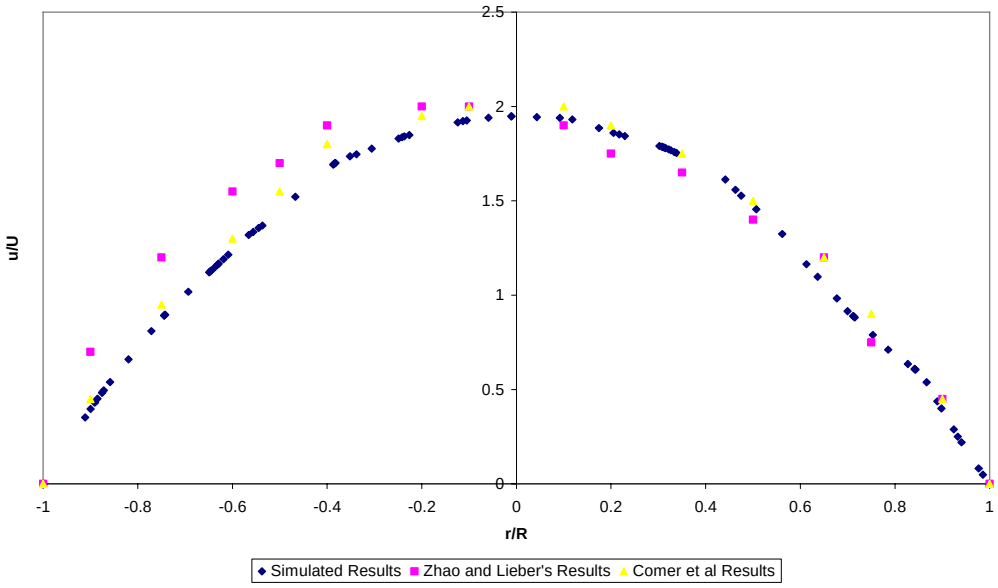

Fig. 4.1: Comparison of axial velocity profile 2-2' in the plane of bifurcation at Re = 1036.

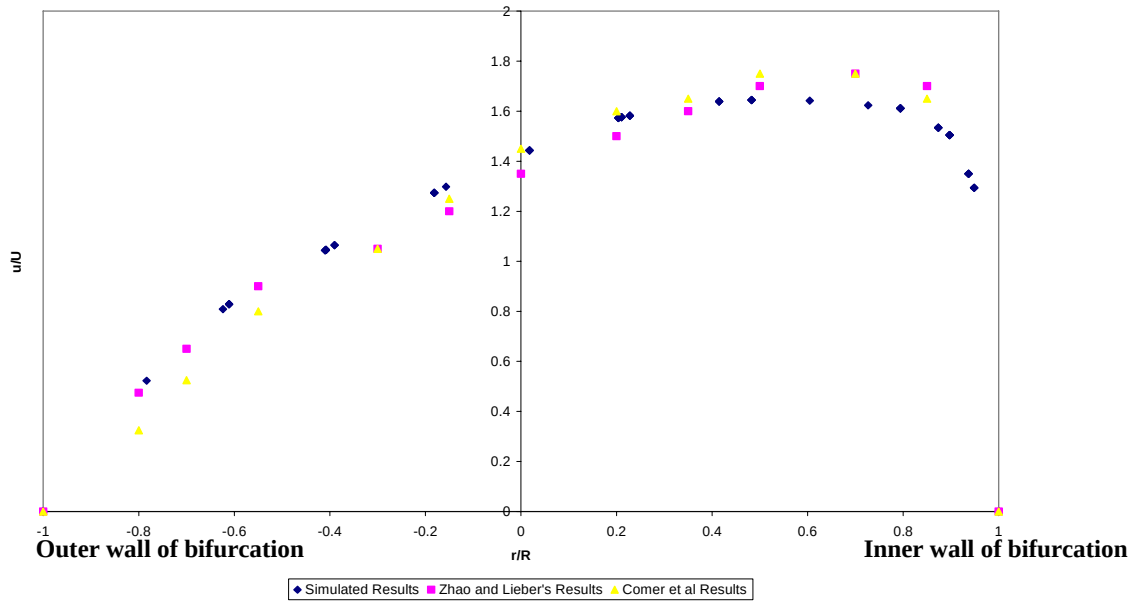

Fig. 4.2: Comparison of axial velocity profile 10-10' in the plane of bifurcation at Re = 1036.

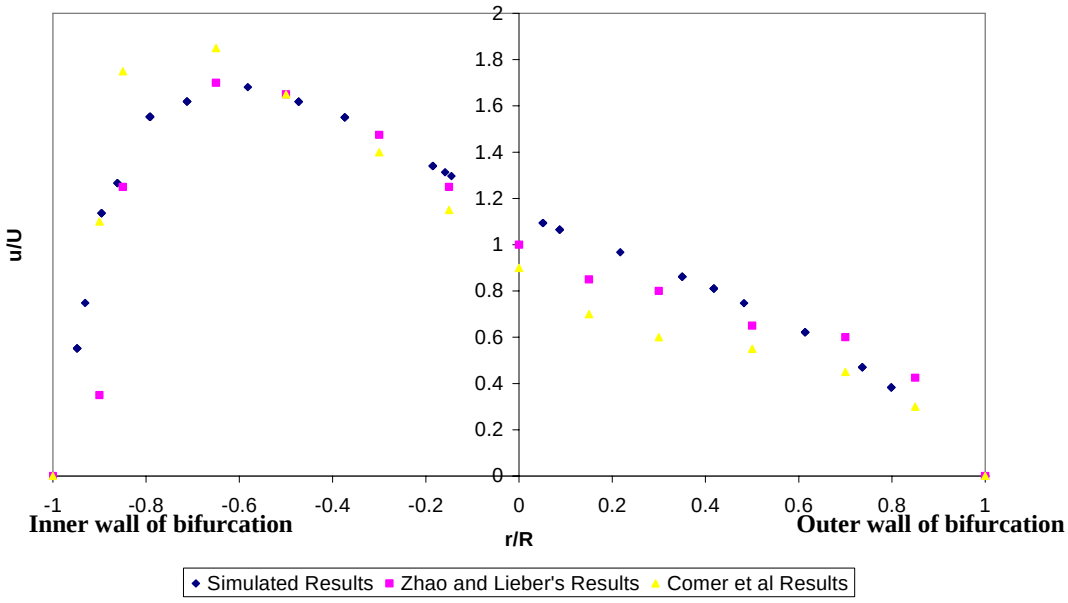

Fig. 4.3: Comparison of axial velocity profile 15-15' in the plane of bifurcation at Re = 1036.

For the profile at 2-2', the simulated results corresponded well with the results of Comer et al (2001). However, the profile at 2-2' from the experimental results of Zhao et al (1994) had some flow asymmetry. It was suggested by Comer et al (2001) that this flow asymmetry was probably due to some blockage effect in one of the daughter tubes. At the profile of 10-10', the axial velocity was skewed towards the

inner wall and this skewness became more significant at 15-15'. Our simulated results corresponded well with the results of Zhao and Comer at 10-10' and corresponded better with the results of Zhao at 15-15'. Similar to the results of Comer, there was no reverse flow observed in the geometry.

4.2 Mid-Plane Axial Flow Fields

Velocity contours in the bifurcation plane (z = 0) were analyzed for the configurations C1, C2 and C3 at Re = 514, 1070 and 2194. For all configurations and Re, it was observed that as flow entered from G3 to G4, high axial velocity regions (lighter areas) existed close to the inner wall of bifurcation, while low axial velocity regions (darker areas) were located close to the outer wall of bifurcation. If velocity profiles were defined in the plane of bifurcation (x = 0) in G4, the velocity profiles would be skewed towards the inner wall of bifurcation, similar to the axial velocity profiles 10-10' and 15-15' shown in the earlier section for the model validation configuration. As flow entered G5, the high axial velocity region still existed close to the inner wall of bifurcation but comparing with that in G4, there was a subtle indication that the high axial velocity region began to move away from the inner wall of bifurcation.

When the bifurcation angle between G3 and one branch of G4 was changed, there seemed to be subtle differences in the axial velocity contours between the various configurations especially for the high Re of 2194. The low axial velocity region in G4 seemed to be largest for C2 where the bifurcation angle between G3 and G4 was the lowest among the three configurations. As flow entered from the affected bifurcation G4 to G5, the high axial velocity region in the median G5 for C2 continued to remain close to the inner wall of bifurcation but for C1 and C3, there was some indication

that the high axial velocity region started to move away from the inner wall of bifurcation as flow entered from G4 to G5.

To illustrate the above-mentioned observations, the mid-plane axial velocity contours for each configuration were shown at various Re in the following diagrams.

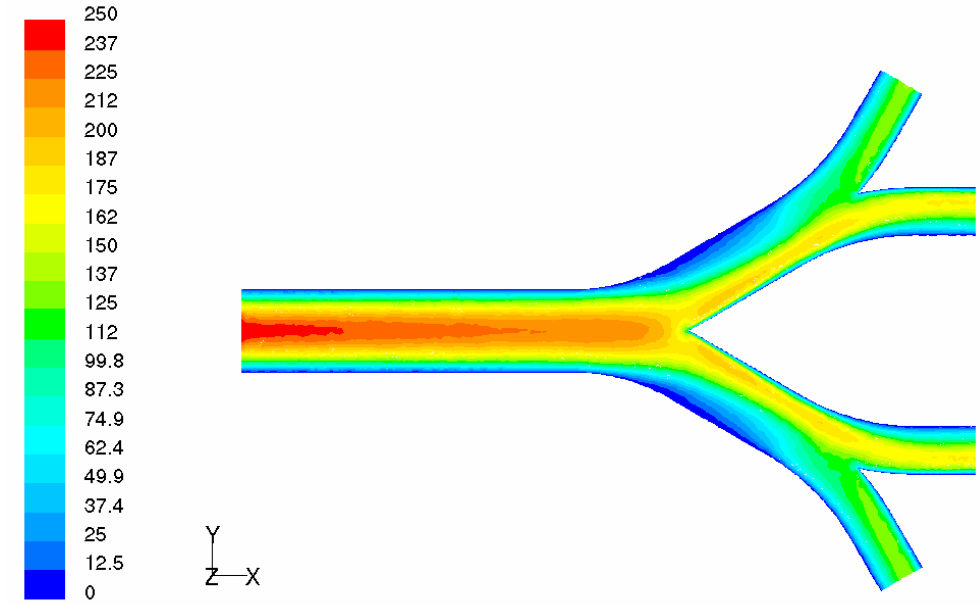

(a)

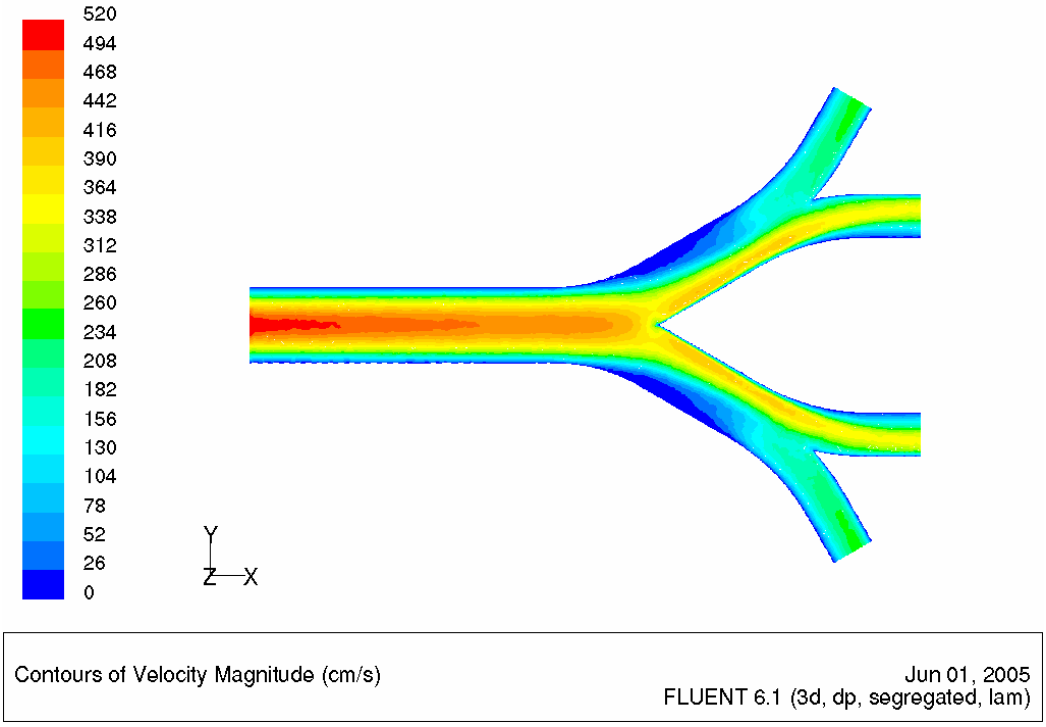

(b)

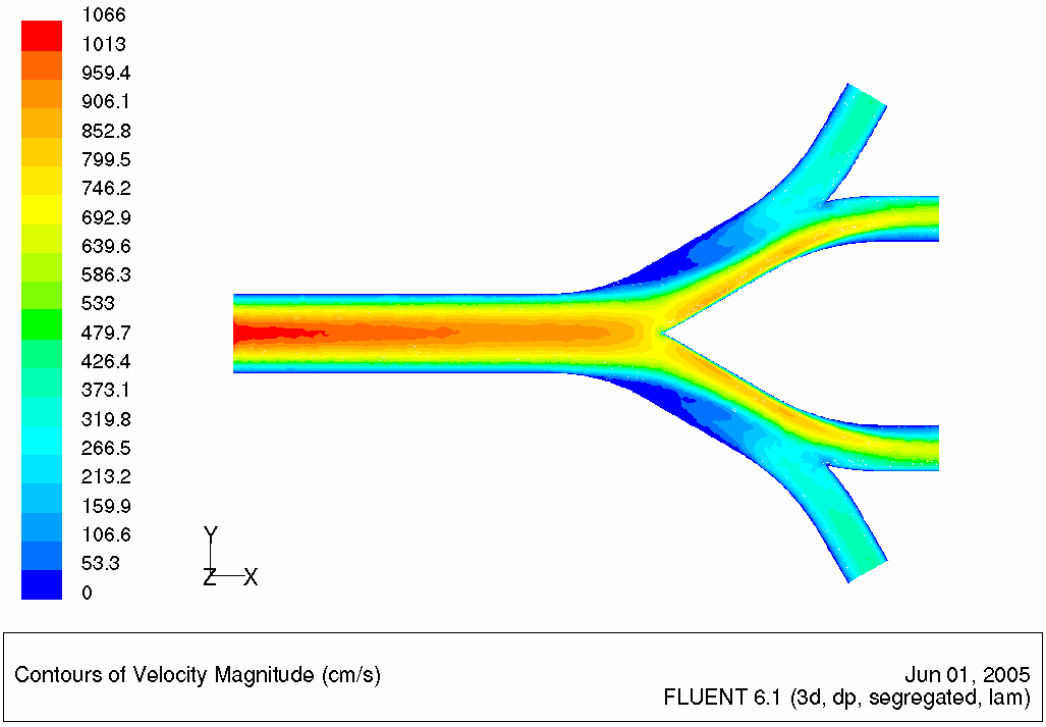

(c)

Fig. 4.4: Mid-plane axial velocity contours for C1 at (a) Re = 514, (b) Re = 1070, and (c) Re = 2194.

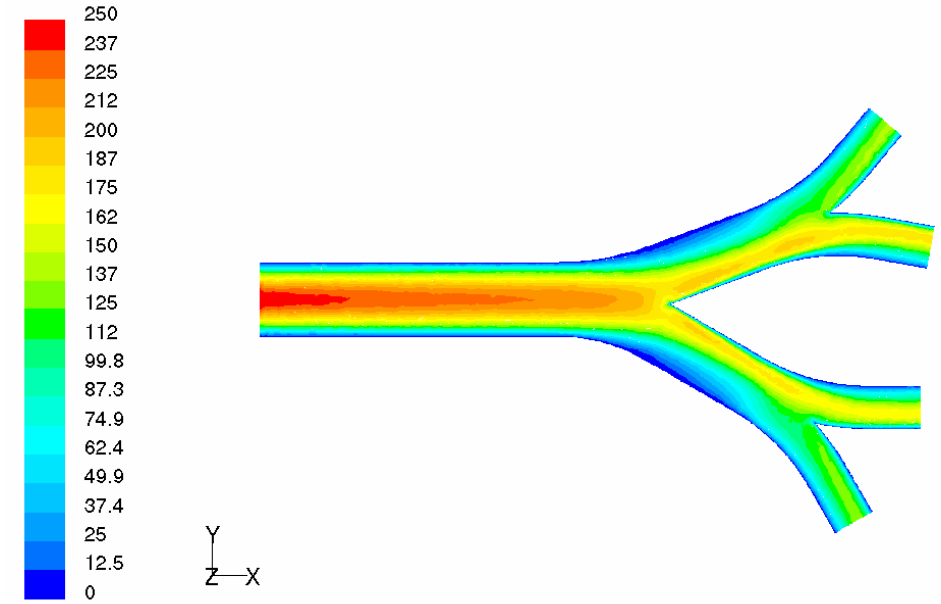
250
237
225
212
200
187
175
162
150
137
125
112
99.8
87.3
74.9
62.4
49.9
37.4
25
12.5
0
Y
Z
X
Contours of Velocity Magnitude (cm/s)
Jun 01, 2005
FLUENT 6.1 (3d, dp, segregated, lam)

(a)

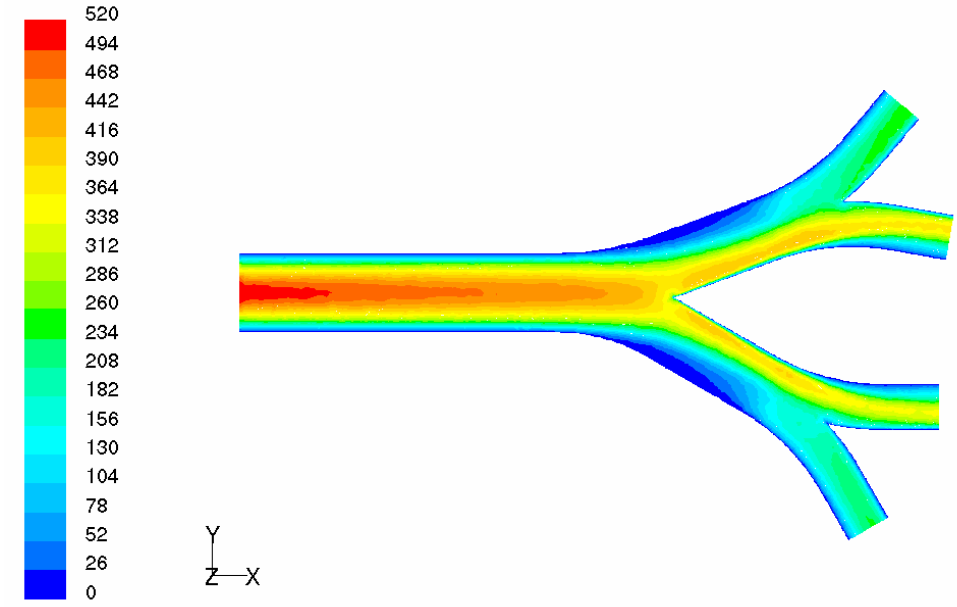
520
494
468
442
416
390
364
338
312
286
260
234
208
182
156
130
104
78
52
26
0
Y
Z
X
Contours of Velocity Magnitude (cm/s)
Jun 01, 2005
FLUENT 6.1 (3d, dp, segregated, lam)

(b)

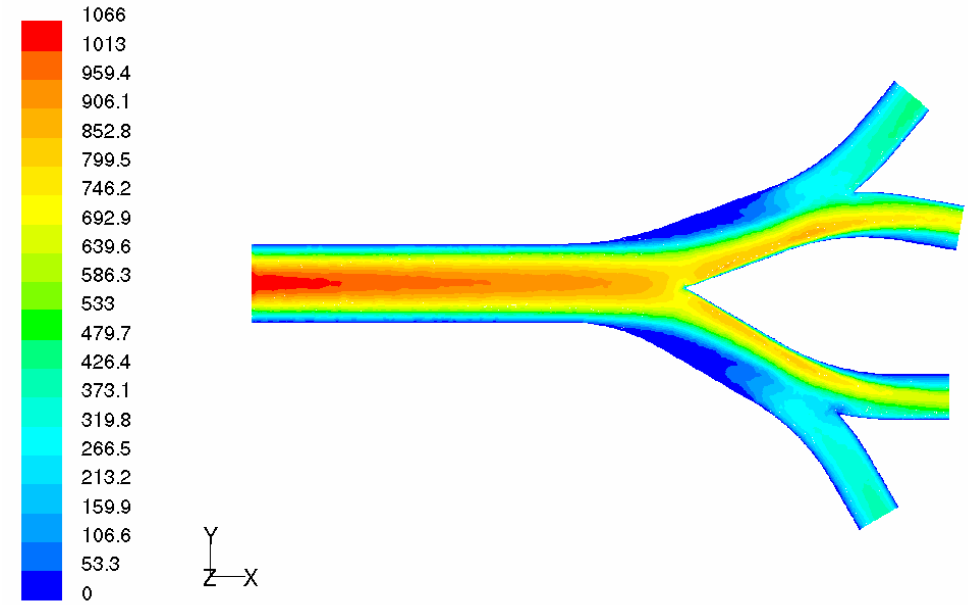

(c)

Fig. 4.5: Mid-plane axial velocity contours for C2 at (a) Re = 514, (b) Re = 1070, and (c) Re = 2194.

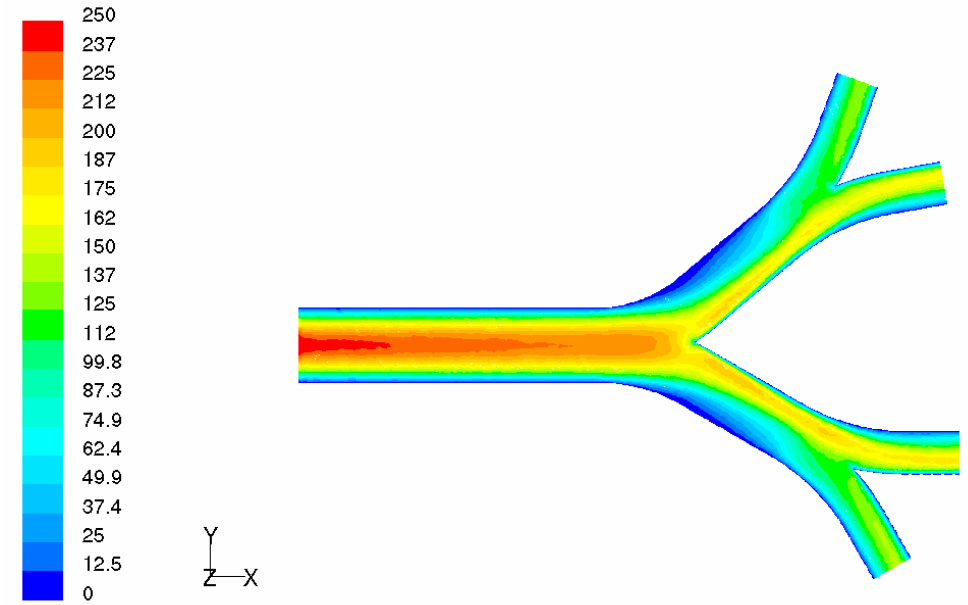

(a)

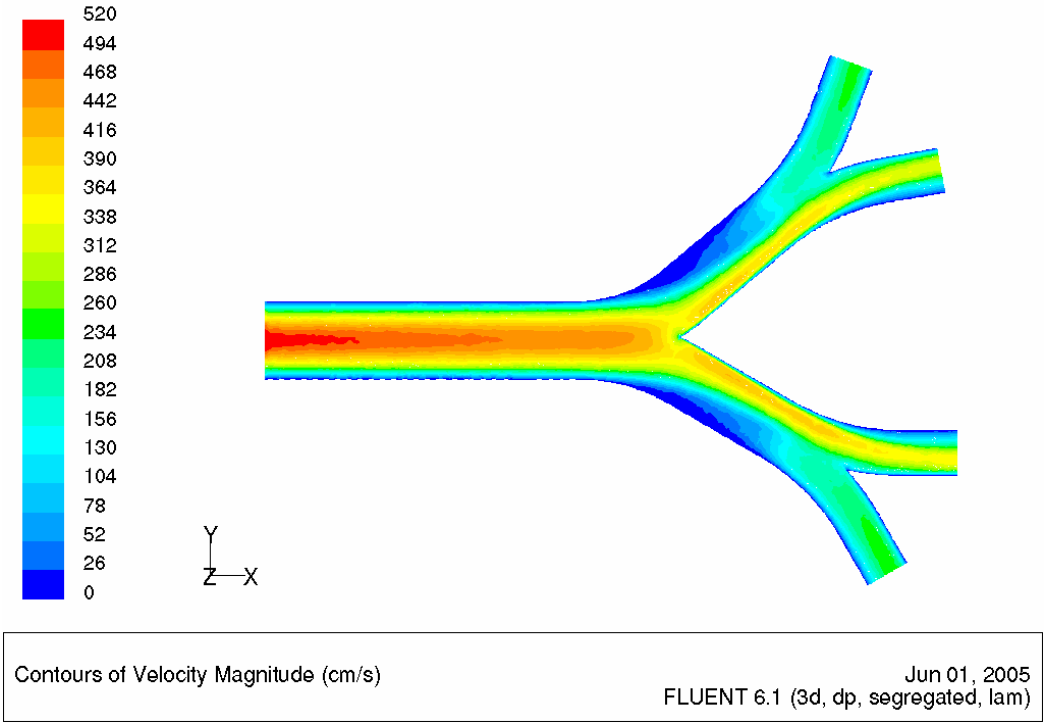

(b)

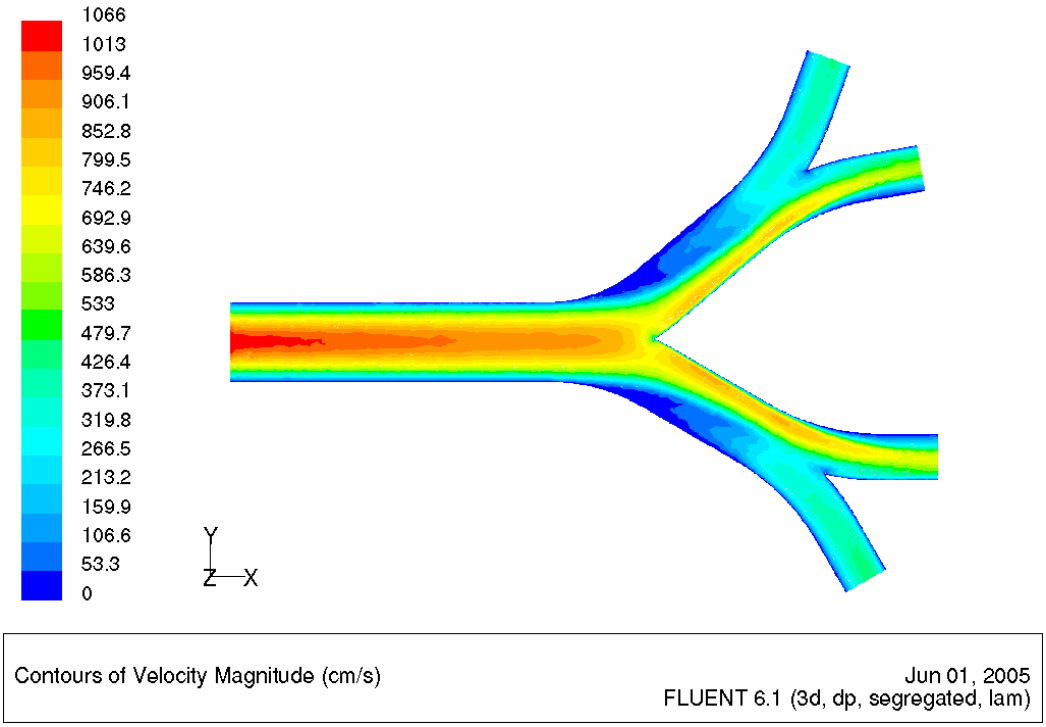

(c)

Fig. 4.6: Mid-plane axial velocity contours for C3 at (a) Re = 514, (b) Re = 1070, and (c) Re = 2194.

The mid-plane axial velocity vectors in the bifurcation plane (z = 0) were also analyzed for each configuration at various Re. It was noticed that at a certain Re for a given configuration, recirculation was observed near the outer walls of the bifurcation in G4 where the axial velocity was the lowest in that region. For C1 and C2, recirculation existed near the outer walls of bifurcation in G4 at high Re of 2194. However, for C3 where the bifurcation angle was the highest among the three configurations, recirculation existed earlier near the outer walls of bifurcation in G4 at Re = 1070.

The following diagrams illustrated the development of the recirculation zone at the outer walls of the bifurcation in G4 as Re increased from 514 to 2194 for C3. The arrows in the diagrams represented the axial air flow directions.

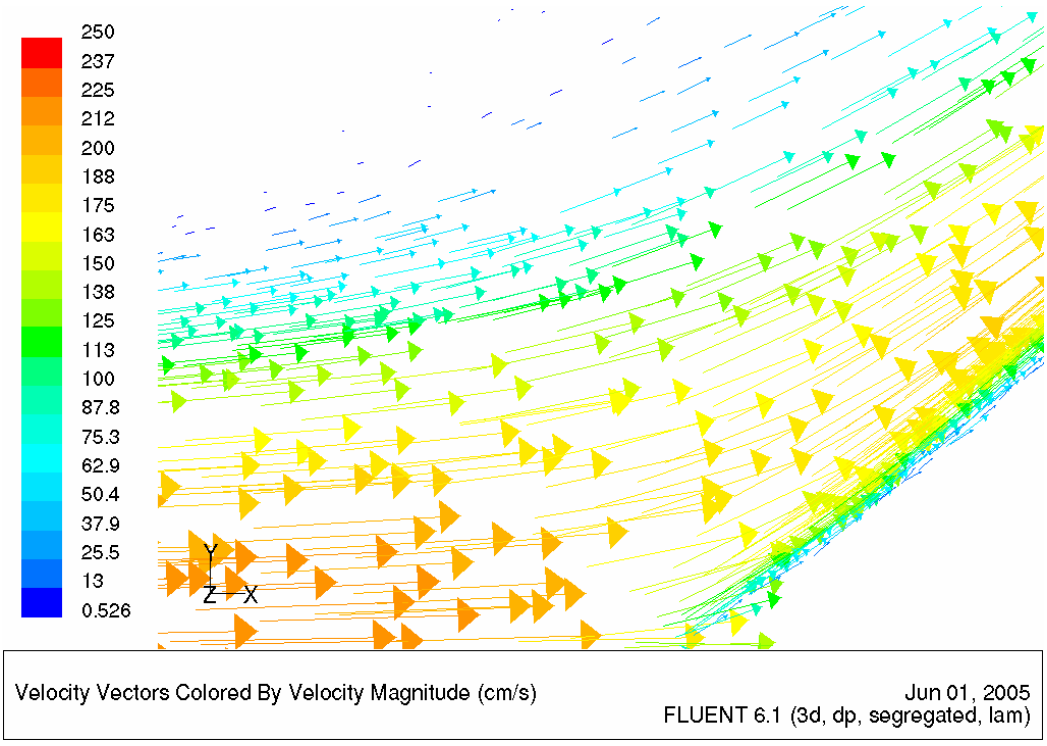

(a)

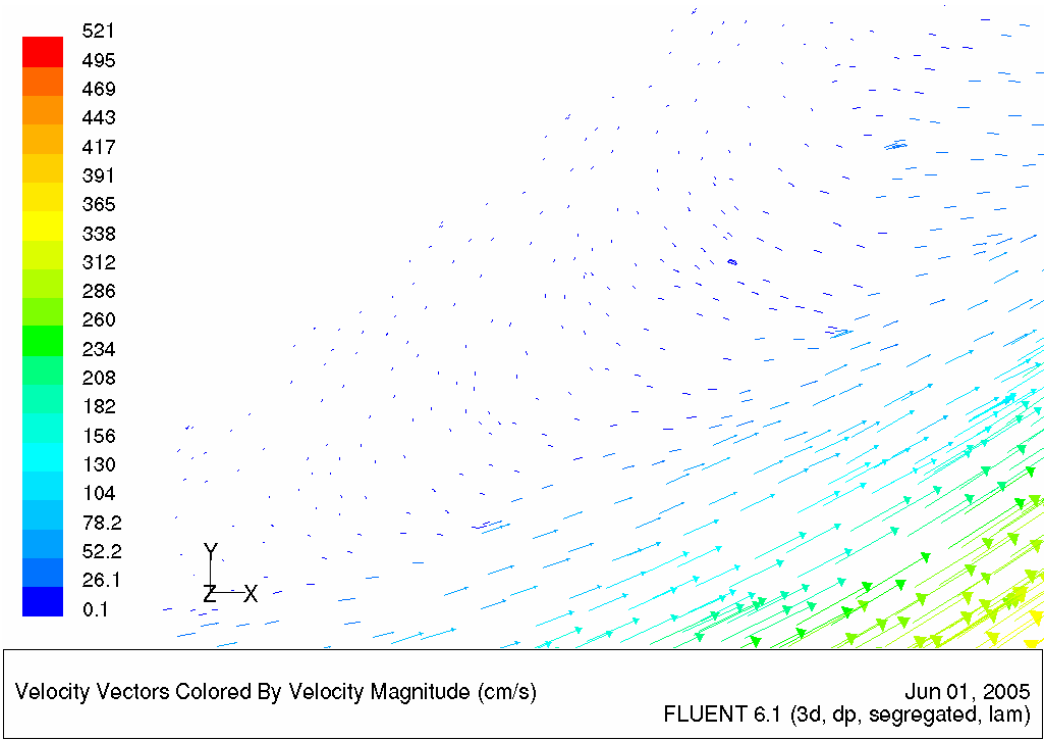

(b)

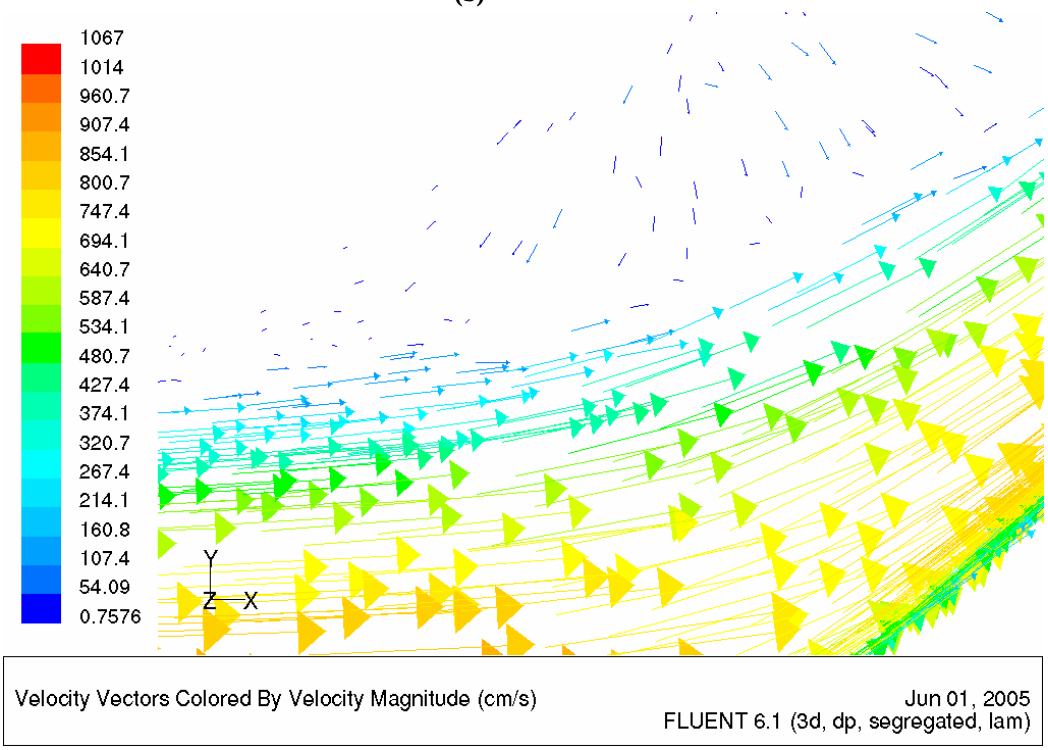

(c)

Fig. 4.7: Mid-plane axial velocity vectors for C3 at (a) Re = 514, (b) Re = 1070, and (c) Re = 2194 near the outer walls of bifurcation in G4. From the vector plots, it was observed that recirculation existed near the outer walls of bifurcation in G4 from Re = 1070 onwards.

It was interesting to note that Comer et al (2001) and Martonen et al (2001) also noted the recirculation near the outer walls of bifurcation in the daughter branches of their configurations at various Re, and the size and intensity of the recirculation depended on the Re.

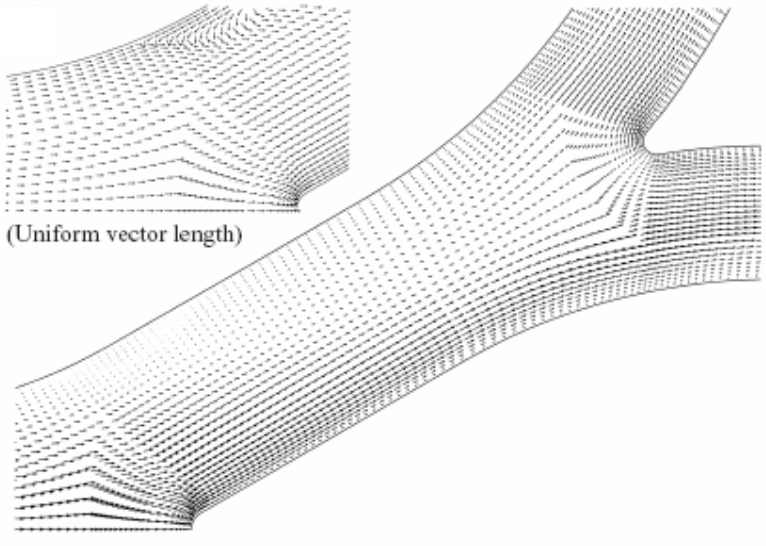

(a)

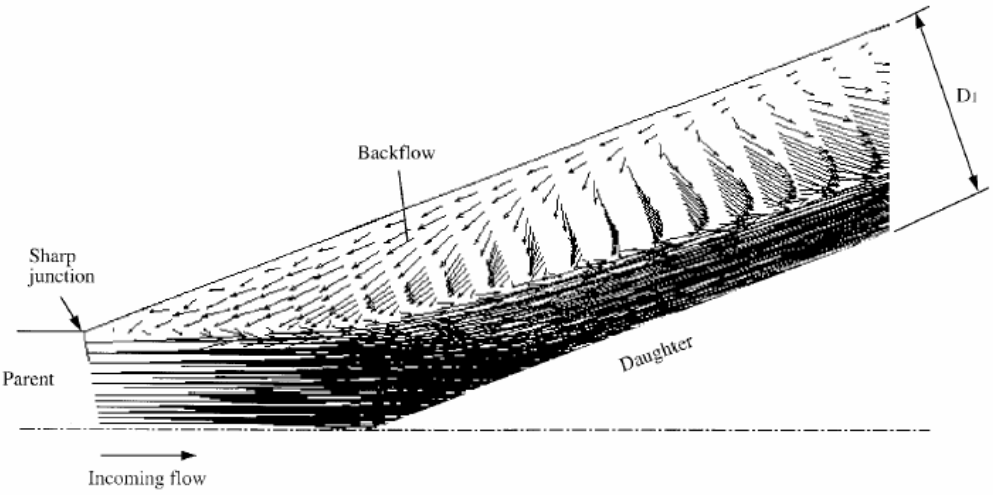

(b)

Fig. 4.8: (a) Velocity vector plots for the planar double bifurcation with rounded carinas with inlet Re = 500 [Comer et al, 2001], (b) Primary velocity fields on the central plane of Model 1 for a parabolic velocity inlet condition with Re = 1175 [Martonen et al, 2001]. It could be seen that recirculation or backflow existed near the outer walls of bifurcation in the daughter tubes.

4.3 Flow Partitioning

Asymmetry in the bifurcation angle between G3 and G4 would cause more flow in one branch than the other in the same generation, thus causing imbalance in the flow partitioning. The imbalance in flow partitioning can be defined as the ratio of the mass flow rates in the *i*th and *j*th branches of the same generation [Liu et al, 2003]. Flow partitioning was analyzed for the branches in G4 as well as for the branches in G5.

In G4, the mass flow rate in the branch affected by the change in the bifurcation angle was compared to that in the unaffected branch and the ratio of the mass flow rates in the branches was given as m(g4-1)/m(g4-2). The variable m(g4-1) referred to the mass flow rate in the affected branch in G4 while m(g4-2) referred to the mass flow rate in the unaffected branch in G4. If the bifurcation was symmetric, m(g4-1)/m(g4-2) would be ideally close to 1. The mass flow rates in the branches were computed for various Re between 514 and 2194 and the results were illustrated in the following graph.

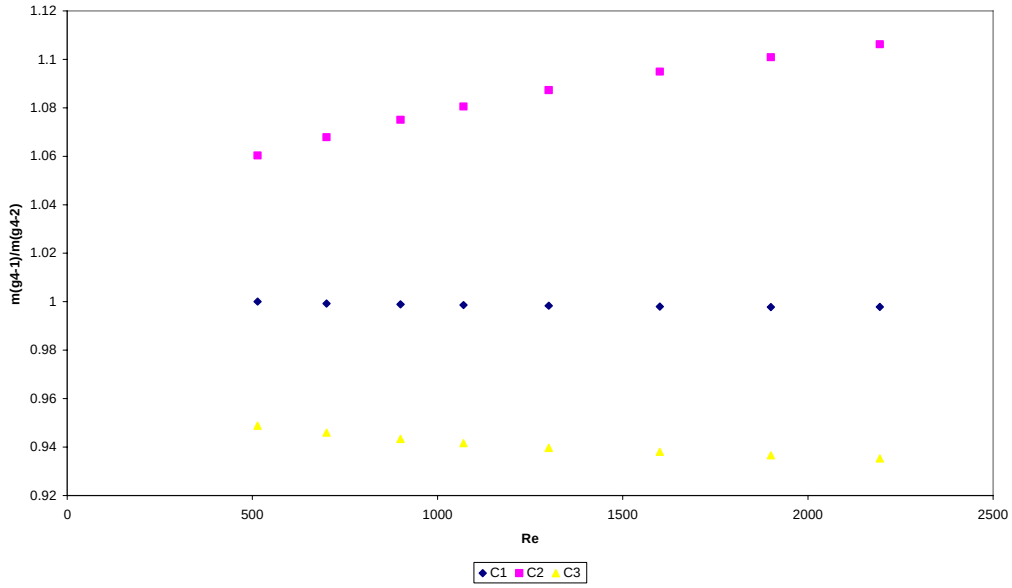

Fig. 4.9: Flow partitioning in G4 for various configuration. It was observed that the ratio remained close to 1 for the symmetric configuration C1. For the asymmetric configurations, mass flow rate was greater in the branch that had a lower bifurcation angle.

For the symmetric configuration C1, the ratio remained close to 1 regardless of the Re. For C2, the ratio was greater than 1 indicating that the mass flow rate in the affected branch was greater than that in the unaffected branch. This imbalance in the flow partitioning increased with increasing Re. Conversely, the ratio for C3 was less than 1 indicating that the mass flow rate in the unaffected branch was greater than the affected branch and again, the imbalance increased with increasing Re. Flow was greater in the branch that gave a smaller bifurcation angle.

Remembering in the previous section that the axial velocity in G4 was skewed towards the inner walls of bifurcation, the flow into downstream G5 would most probably not be equal in the branches of G5 even for the symmetric configuration. The ratio between the mass flow rate in the lateral branches of G5, m(g5-1) or m(g5-4), and the mass flow rate in the median branches of G5, m(g5-2) or m(g5-3), was calculated for the various configurations at different Re. The imbalance in flow partitioning in the branches of G5 was illustrated in the following graph.

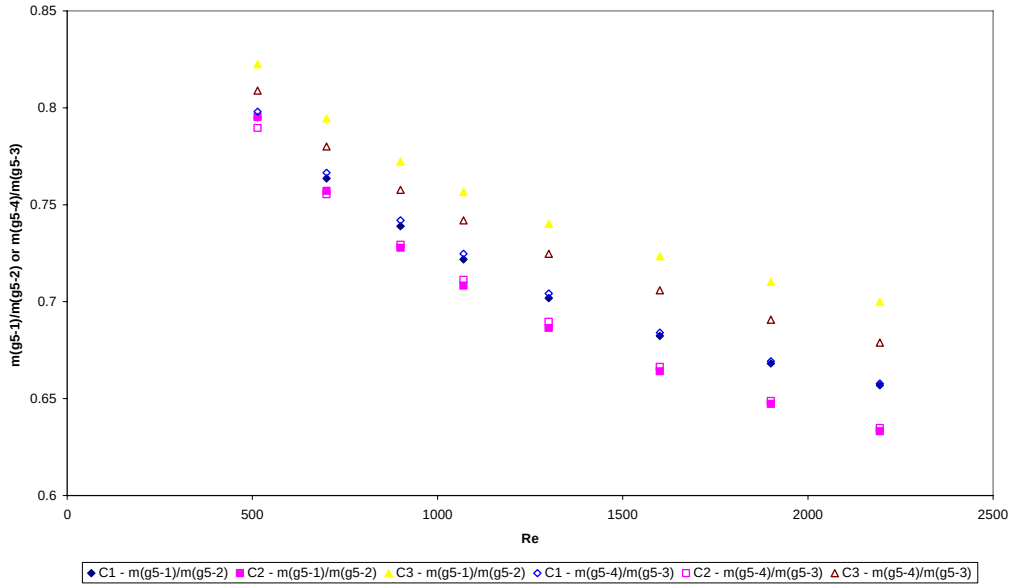

Fig. 4.10: Flow partitioning in G5 for various configurations. It was observed that for all configurations, the flow into the median branch was greater than that for the lateral branch.

The skewed velocity profiles in G4 would bring more flow into the median branches of G5 and hence, the ratio of the mass flow rates between the lateral and median branches of G5 would be less than 1. From the graph, it showed that the ratios were less than 1 and that the asymmetry in the upstream bifurcation of G4 caused various degrees in the imbalance in flow partitioning in the branches of G5. The configuration C2, having the lowest bifurcation angle between G3 and G4, had the smallest ratio indicating that more flow would be in the median branches of G5 than the lateral branches. When the angle of bifurcation in G4 increased, the ratio increased possibly indicating that there was comparatively more flow into lateral branches or less flow into the median branches than that of C1 and C2. It was observed that for C1 or C2, the ratios remained the same regardless of whether the flow into G5 was from the affected G4 branch or the unaffected G4 branch. However, for C3, the ratio where flow originated from the affected G4 branch was greater than the ratio where flow originated from the unaffected G4 branch. Comparatively more flow would enter the branch that gave a smaller bifurcation angle. Since the unaffected branch of G4 in C3

had a smaller bifurcation angle than that in the affected branch, more flow would enter into the median branch of G5, giving rise to a lower ratio.

4.4 Secondary Currents

Planes transverse to the bifurcation or in the y-z plane were defined at the beginning and end of the affected and unaffected branches of G4, and the beginning of all branches of G5. The velocity contours and vectors were analyzed at these planes for each configuration at various Re. The order of analysis would be from the affected branch of G4 (g4-1-1 and g4-1-2), the unaffected branch of G4 (g4-2-1 and g4-2-2), the lateral (g5-1-1) and the median (g5-2-1) branches of G5 where the upstream origin was the affected G4 branch, to the lateral (g5-4-1) and the median (g5-3-1) branches of G5 where the upstream origin was the unaffected G4 branch. The illustrations of the velocity contours and vectors at the above-mentioned planes for various configurations at each Re were given in the Appendix.

As flow entered from G3 into the affected G4 branch, secondary currents in the form of double vortices existed in g4-1-1 for all configurations at all Re. The intensities of the vortices increased and the centers of the vortices moved toward the outer wall of the bifurcation as the bifurcation angle increased. This effect increased when the Re increased. At Re = 2194, C3 showed a secondary vortex near to the outer wall of bifurcation. The velocity contours for g4-1-1 showed that at low Re, the low axial velocity region (indicated by the darker area) had not started to push into the high velocity region (indicated by the lighter area) even as the bifurcation angle increased. At high Re, however, the low velocity region had pushed into the high velocity region as the bifurcation angle increased. The high velocity region moved closer to the inner

wall and became more compressed by the low axial velocity region as the bifurcation angle increased. Possible backflow or recirculation, that was indicated by negative values of the low axial velocity region in the positive x-direction, started to exist from Re = 2194 onwards for C1, and from Re = 1070 onwards for C2 and C3. The following diagram showed the primary vortices as well as a secondary vortex near to the outer wall of bifurcation for C3 at high Re.

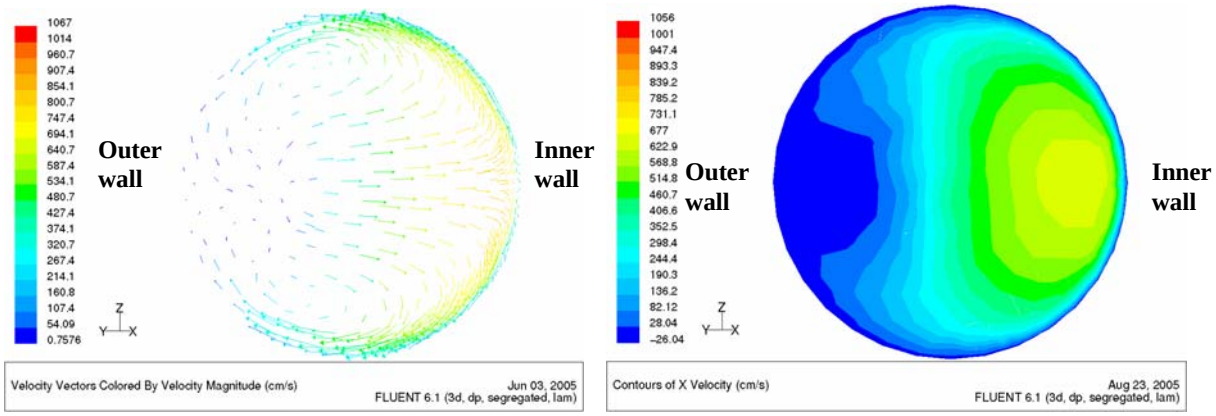

Fig. 4.11: Velocity vector and contour plots at g4-1-1 for C3 at Re = 2194. Primary vortices and a secondary vortex near the outer wall of the bifurcation could be seen in the velocity vectors plot.

As flow progressed further downstream to g4-1-2 in the affected bifurcation of G4, vortices that were near the outer walls of bifurcation started to move towards the center of the bifurcation regardless of the bifurcation angle. There was the similar effect of increased intensities of the vortices when the bifurcation angle and Re were increased. It was interesting to note that for C2, the vortices were not well developed and distinct even at high Re and that the vortices remained in their respective positions even as Re increased. The trend with the velocity contours with Re and bifurcation angle was similar to that for g4-1-1. The high axial velocity region started to push the low axial velocity region from the outer wall of bifurcation as the Re increased and the degree of penetration increased with bifurcation angle.

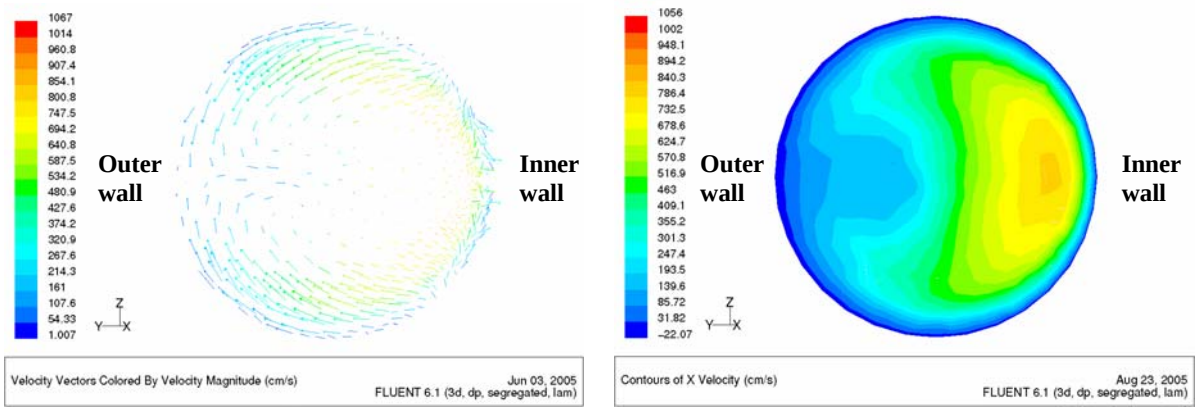

Fig. 4.12: Velocity vector and contour plots at g4-1-2 for C2 at Re = 2194. Vortices were not distinct even at high Re.

For the unaffected bifurcation in G4 at g4-2-1, the change in intensities and locations of the double vortices followed the same trend as in the affected bifurcation. One notable observation was that at Re = 2194, there was no significant secondary vortex developing near to the outer wall of bifurcation which was contrary to that in g4-1-1 of the affected bifurcation. Similar to the development of the velocity contours with bifurcation angle and Re for the affected bifurcation in G4 at g4-1-1, the high velocity region seemed to push the low velocity region from the outer wall towards the inner wall of the bifurcation. One notable difference between the velocity contours in g4-2-1 and g4-1-1 was that the degree of penetration of the low velocity region into the high velocity region for C3 at Re = 2194 was not as great as that in g4-1-1 for C3 at similar Re. On the other hand, for C2, the low velocity region seemed to penetrate slightly deeper toward the inner wall of bifurcation at Re = 2194 as compared to that in the affected bifurcation, g4-1-1, for C2.

As the flow progressed downstream to g4-2-2 in the unaffected bifurcation of G4, primary vortices were not immediately obvious until Re = 2194 for all configurations. The trend of the velocity vectors in g4-2-2 with regards to change in bifurcation angle

and Re was similar to that in g4-1-2. The velocity contours in g4-2-2 had the same trend with regards to the change in bifurcation angle and Re as the velocity contours in g4-1-2. It was observed that the high axial velocity region in g4-2-2 for C2 was smaller in size and magnitude than in g4-1-2 at the same Re, while the high axial velocity region in g4-2-2 for C3 was larger in size and magnitude than in g4-1-2 at same Re. This difference was magnified when the Re increased.

As flow entered the upper lateral bifurcation of G5, g5-1-1, from the affected bifurcation in G4, weak double vortices started to develop and as Re increased, another set of weak secondary double vortices started to develop near to the inner walls of the bifurcation. The secondary vortices became faintly noticeable especially for C3 at Re = 2194. At a particular Re, there was apparently no change in the relative positions of the vortices as the bifurcation angle was increased. The high axial velocity region remained close to the inner walls of bifurcation for all configurations. As the bifurcation angle increased, the high velocity region diminished in size.

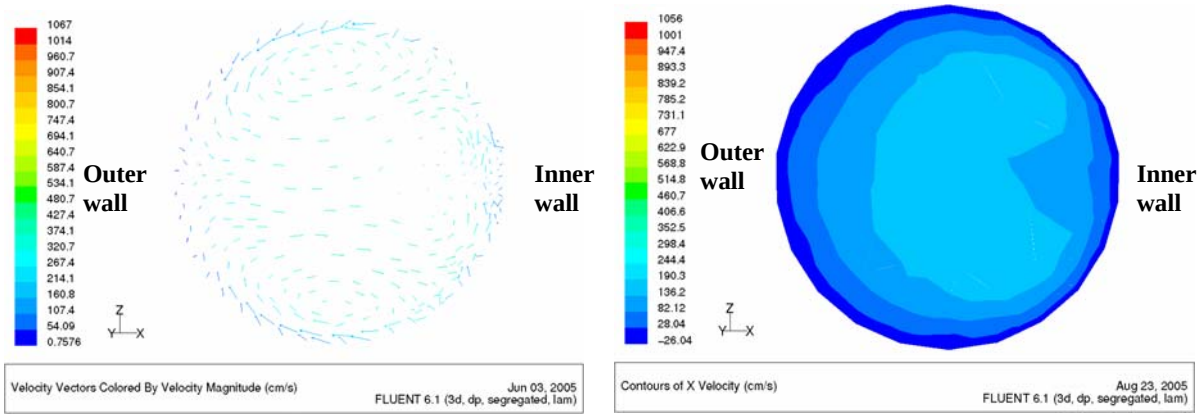

Fig. 4.13: Velocity vector and contour plots at g5-1-1 for C3 at Re = 2194. Weak secondary vortices could be seen near the inner wall of bifurcation.

In the median branch, g5-2-1, of G5, the intensities of the primary vortices were significantly greater than the lateral branch, g5-1-1, since more flow entered the median branch. As Re increased, the primary vortices moved closer to the outer walls of bifurcation and also closer to the top and bottom of the branch for each configuration. Secondary vortices started to develop near the inner walls of bifurcation from a certain Re. For C3, secondary vortices started to form at Re = 1070 while for C1 and C2, secondary vortices were visible only at the highest Re = 2194. These secondary vortices became more distinct as bifurcation angle increased. As Re increased, the low axial velocity region started to engulf the high velocity region at the inner walls of bifurcation. This effect was magnified when the bifurcation angle increased.

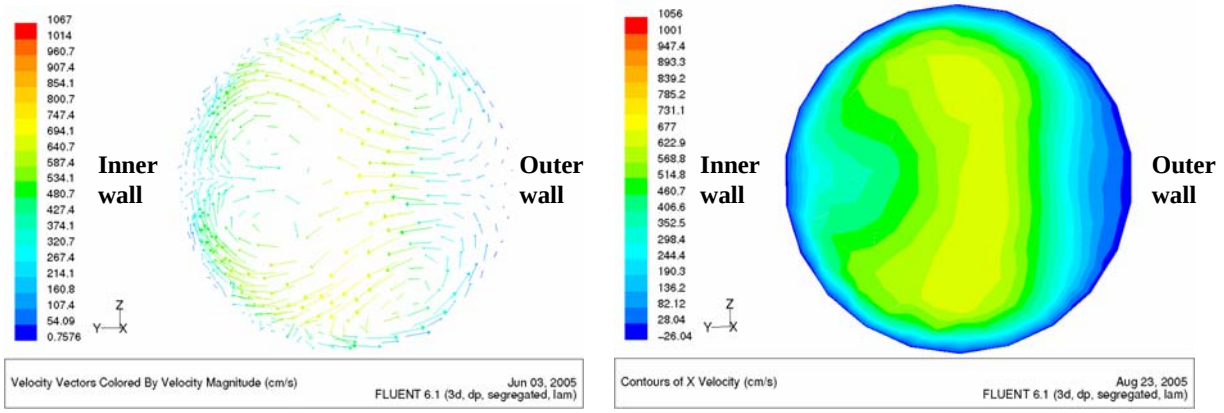

Fig. 4.14: Velocity vector and contour plots at g5-2-1 for C3 at Re = 2194. Secondary vortices near the inner wall of bifurcation can be seen clearly in the velocity vector plot.

The velocity vectors for the flow entering the lower median branch, g5-3-1, of G5 had similar trends as those in the upper median branch, g5-2-1, of G5. For C2, the secondary vortices were stronger and more distinct in the lower median branch, g5-3-1, than the upper median branch, g5-2-1, at high Re of 2194. In addition, for C2, weak secondary vortices started to form earlier at Re=1070 in the lower median branch whereas secondary vortices were only visible at Re=2194 in the upper median branch.

For other configurations, there were no significant differences in the intensity or the formation of the secondary vortices between the lower and upper median branch of G5. The velocity contours for g5-3-1 also showed similar trends as those in g5-2-1. However, at high Re, the low velocity region seemed to penetrate more into the high velocity region as the bifurcation angle decreased when compared to the extent of penetration in g5-2-1.

Comparing to the flow in the upper lateral branch, g5-1-1, similar characteristics appeared in the secondary currents of the lower lateral branch, g5-4-1. Weak secondary vortices developed near the inner walls of bifurcation for all configurations. Weak primary vortices moved towards the outer walls of bifurcation as Re increased. As the bifurcation angle increased, the high velocity region also increased in size. This was in contrast with the secondary currents in upper lateral branch, g5-1-1.

4.5 Particle Deposition

The air flow fields at selected sites of the asymmetric and symmetric configurations had been analyzed and compared for various Reynolds numbers. In this section, the particle deposition in the symmetric configuration, C1, would first be compared to published results of similar configuration. Next, the effect of different inlet (G3) particle release profiles such as monodispersed parabolic, homogeneous, and polydispersed parabolic, on the overall particle deposition efficiency for various configurations would be examined. In addition, the particle deposition patterns at various sites of the double bifurcation would be studied for various release profiles as well as different particle sizes and Re.

4.5.1 Comparison of Particle Deposition Efficiency with Published Results

In section 3.2.4, the particle deposition efficiency (DE) was defined as percentage of the number of particles trapped in a particular region of interest over the total number of particles entering that region. In this section, the particle deposition efficiencies for the 1st bifurcation as well as the 2nd bifurcation were compared to published results with similar geometrical configurations. The definitions of the 1st and 2nd bifurcations were described in Kim et al (1999) and Comer et al (2001). The 1st bifurcation described the region stretching from G3 to 0.6cm into the G4 branches, while that of the 2nd bifurcation stretches from the remaining lengths in G4 branches till G5 branches. Kim et al (1999) did experimental work on doubly bifurcated glass tube configuration and calculated the deposition efficiency for the 1st and 2nd bifurcations. Comer et al (2001) then adopted the configuration that Kim used and simulated the air flow and particle deposition patterns. Since, in this work, we adopted the configuration as described by Comer, the particle deposition efficiencies for the 1st and 2nd bifurcations with that from Kim (1999) and Comer (2001) would be compared. The configuration that had dimensions similar to the ones used by Kim and Comer was C1 where the geometry was symmetric between G3 and G4. The type of particle release profile at the inlet used for the comparisons was monodispersed parabolic. The following graphs illustrated the comparisons.

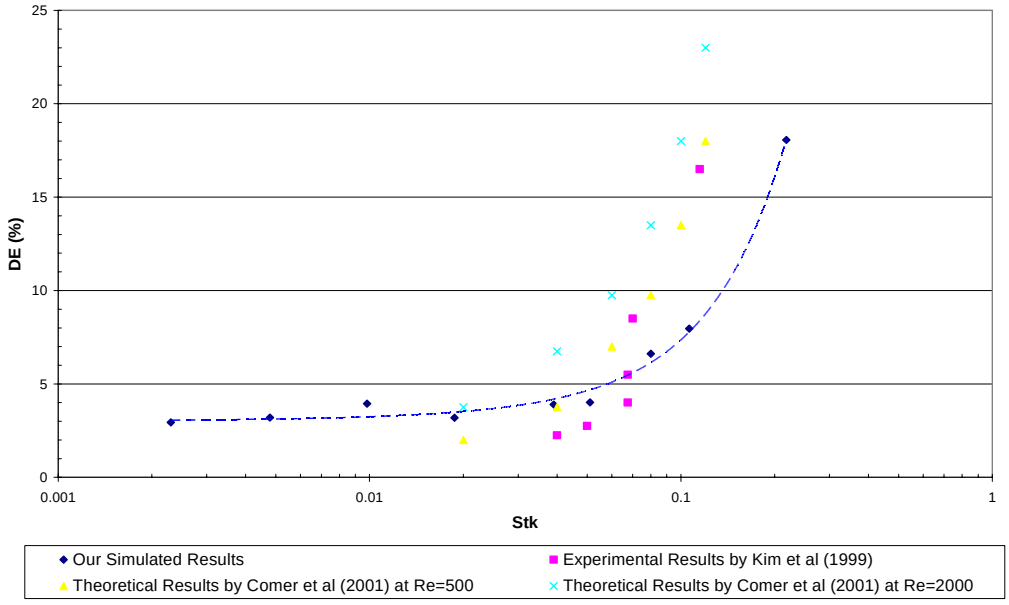

(a)

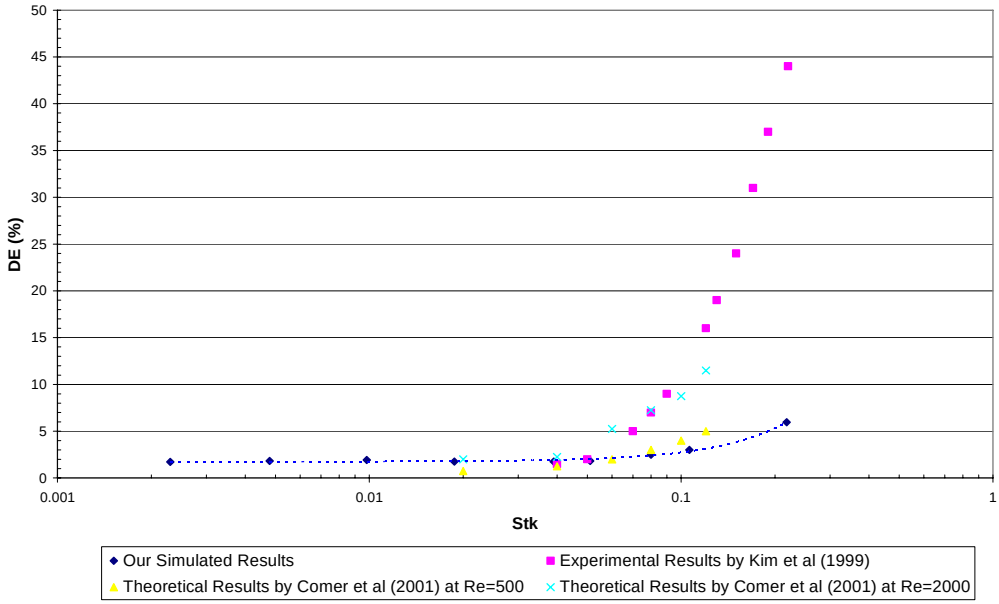

(b)

Fig. 4.15: Particle deposition efficiency comparisons of simulated results with published results in (a) 1st bifurcation, and (b) 2nd bifurcation.

Both graphs showed that for low Stk (~< 0.05), the simulated particle deposition overestimated that of the experimental results but underestimated the deposition for higher Stk (~> 0.1). This phenomenon was also reported by Kim et al (1999) and

Balashazy et al (1991). The reason given was that the theoretical equations were derived from either circular bend geometry or a simple analogy of the circular bend. In addition, the CFD results were very sensitive to differences in bifurcation geometries. The configuration used although had similar dimensions as the ones used by Kim and Comer, it should be noted that some details on the manner in which the geometry was constructed, especially at the bend, were modified slightly to be within the algorithmic confines of the geometry builder Gambit. When comparing the simulated results for the 2nd bifurcation with Comer's simulated results, it was interesting to note that our results correlated well when Re=500 was used in the Comer's simulation. Nevertheless, the simulated results should provide a starting basis for comparing the effects of geometrical asymmetries and particle release patterns on the overall particle deposition and the deposition patterns in various sites of the lungs.

4.5.2 Overall Deposition Efficiency and the Effects of Particle Release Profile and Geometry

The overall particle deposition efficiency was plotted against Stk for various configurations to investigate the effects of the inlet particle release profiles and geometry. The following graphs showed the plots as described.

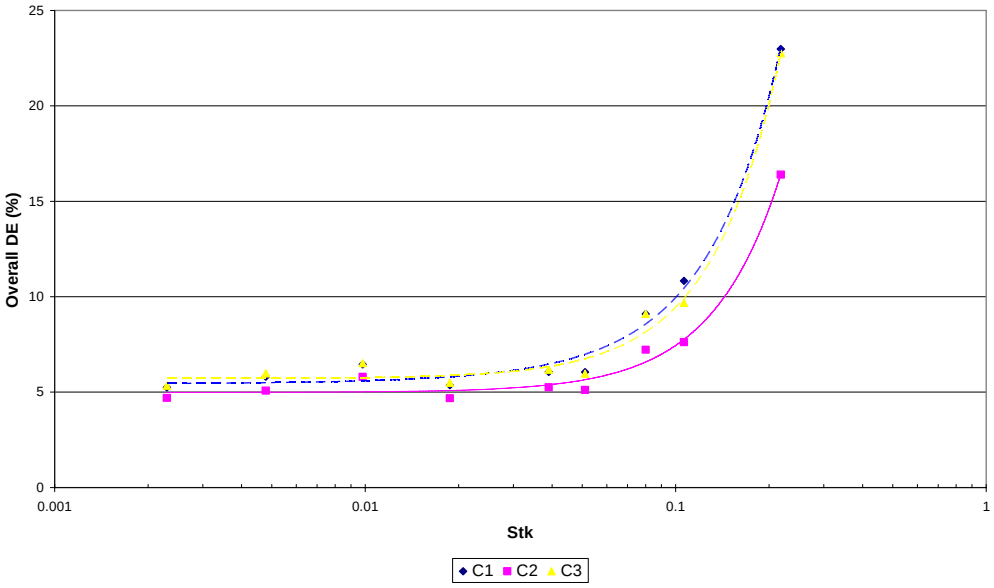
25
20
15
10
5
0
Overall DE (%)
0.001
0.01
0.1
1
Stk
C1 C2 C3

(a)

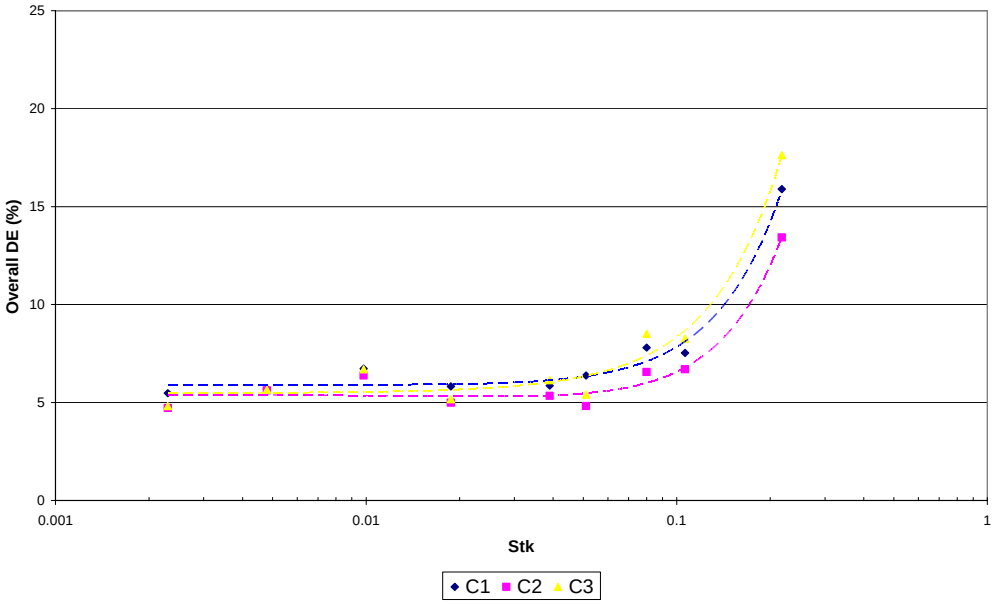
25
20
15
10
5
0
Overall DE (%)
0.001
0.01
0.1
1
Stk
C1 C2 C3

(b)

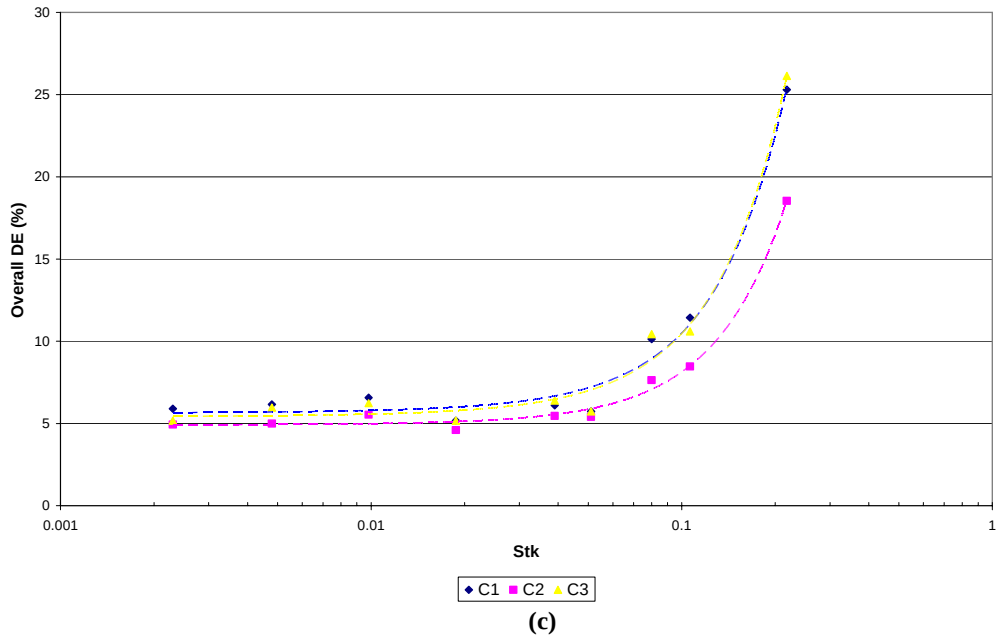

(c)

Fig. 4.16: Overall particle deposition efficiencies as functions of Stk for various configurations with (a) monodispersed parabolic, (b) monodispersed homogeneous, and (c) polydispersed parabolic particle release profiles at inlet of G3.

From the graphs, it could be observed that for all particle release profiles, there were only subtle differences between the various configurations in the overall particle deposition efficiencies at low Stk (~ < 0.01) but as Stk increased, the difference in the overall deposition efficiency between C1/C3 and C2 increased. It was interesting to note that regardless of the type of inlet particle release profiles there was little difference between the overall deposition efficiencies of C1 and C3. This seemed to suggest that when the bifurcation angle at G3 and G4 changed from 20 to 30 degrees, there was a significant increase in the overall deposition efficiency at high Stk. However, as the bifurcation angle increased further from 30 to 40 degrees, there seemed to be significantly less difference between the overall deposition efficiencies of C1 and C3 even at high Stk. This significant difference in the overall particle deposition efficiency between C1/C3 and C2 might be attributed to the significant increase in the intensity of the double vortices with bifurcation angle change from 20

to 30 degrees. As the intensity of the double vortices increased, the particles might be pulled away from the vortical centres and thus impact and deposit on the walls of bifurcation [Fontana et al, 2005, Comer et al, 2001].

If the maximum difference in the overall particle deposition efficiency between C1/C3 and C2 were to be quantified for each inlet release profile, the monodispersed homogeneous particle release profile would give the lowest maximum difference of 31% as compared to a maximum difference of 40 – 41% for both the monodispersed parabolic and polydispersed parabolic profiles respectively. The maximum overall deposition efficiency with the polydispersed parabolic release profile was the highest among the three profiles at over 25%, while the maximum overall deposition efficiency with the monodispersed homogeneous release profile was the lowest at under 20%.

4.5.3 Particle Deposition Pattern

The effects of the inlet release profile on the particle deposition pattern at selected sites of the lungs from G3 to G5 would be examined for both small and large particle sizes (1 and 5μm) at low and high Re (514 and 2194). The sites of the lungs would be the mother branch (g3), the carinal region between G3 and G4 (g3-g4), the upper and lower G4 branches (g4-1 and g4-2), upper and lower carinal regions between G4 and G5 (g4-g5-1 and g4-g5-2), upper and lower lateral G5 branches (g5-1 and g5-4), and upper and lower median G5 branches (g5-2 and g5-3). The inlet release profiles used were monodispersed parabolic, monodispersed homogeneous and polydispersed parabolic.

Monodispersed Parabolic Inlet Release Profile

The following graphs showed the particle deposition patterns when the profile was monodispersed parabolic.

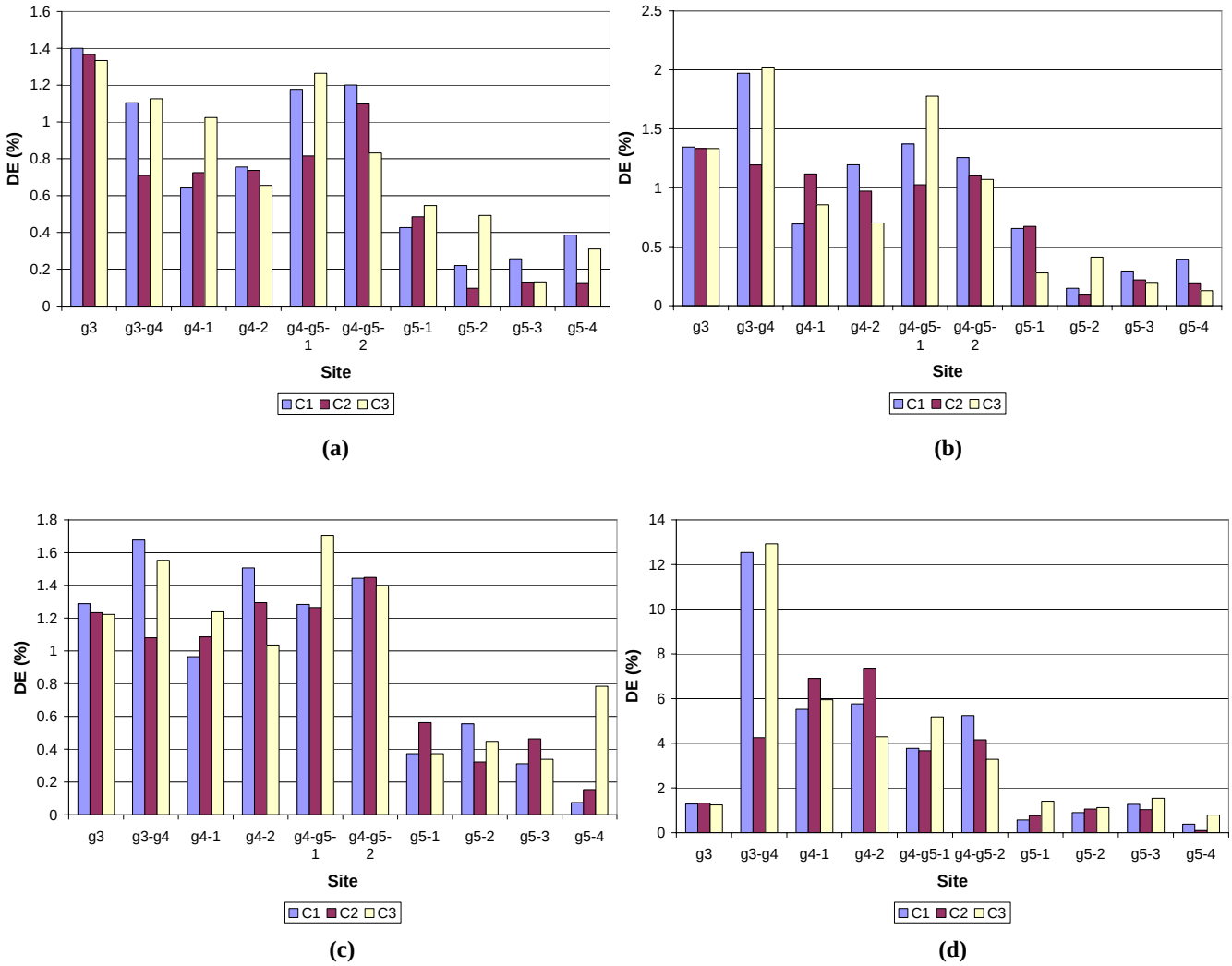

Fig. 4.17: Particle deposition patterns in various configurations for (a) d_p = 1µm, Re = 514, (b) d_p = 5µm, Re = 514, (c) d_p = 1µm, Re = 2194, and (d) d_p = 5µm, Re = 2194, when the release profile was monodispersed parabolic.

At low Re and for small particles, the particles deposited early in the mother branch, g3, as the DE was highest at g3. As the particle sizes or the Re increased, more and more particles got deposited at the carinal region between g3 and g4 by impaction, such that the deposition efficiency at g3-g4 became more dominant as compared to

the deposition efficiencies at other sites. Predominant deposition at g3-g4 occurred at low Re and large particle sizes for C1 and C3 but for C2, it occurred only when both the Re and particle size were high. When the Re was low and small particles were involved in C2, the DE at g4-2 was about 1.57% higher than that at g4-1. In C3, the DE at g4-1 was 56.2% greater than g4-2. This trend also holds for high Re. Considering that the angle made by g4-1 with the horizontal was greater in C3 than C2, it seemed that the DE was higher in the bifurcation with a greater angle. An exception to this trend would be C2 at high Re and involving small particles. It was observed that although C1 was a symmetric configuration, the DE in both g4-1 and g4-2 were not equal although it might seem that the difference in DE between g4-1 and g4-2 diminished when the Re was increased. As Re increased, the air flow into the G5 median branches (g5-2 and g5-3) increased and subsequently the flow of particles into these branches increased. As such, the probability of particles getting deposited in the median branches increased. This could be observed in that the DE in g5-2 and g5-3 increased substantially as compared to the lateral branches when the Re increased.

Monodispersed Homogeneous Inlet Release Profile

The following graphs illustrated the particle deposition patterns for various configurations at various Re and particle sizes when the release profile was monodispersed homogeneous.

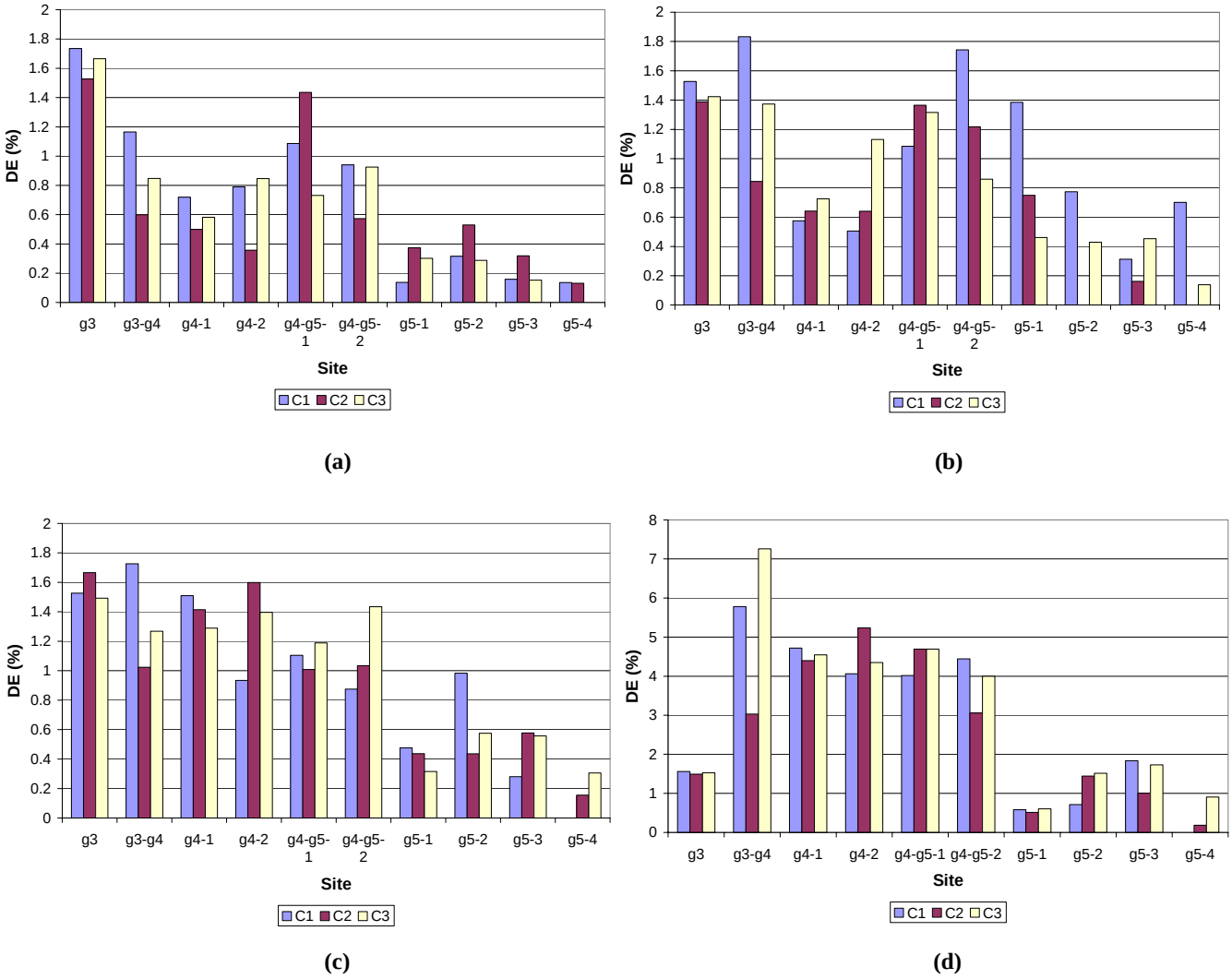

Fig. 4.18: Particle deposition patterns in various configurations for (a) d_p = 1µm, Re = 514, (b) d_p = 5µm, Re = 514, (c) d_p = 1µm, Re = 2194, and (d) d_p = 5µm, Re = 2194, when the release profile was monodispersed homogeneous.

Similar to the parabolic profile, particles deposited mainly at G3 when the Re and particle sizes were low. However, deposition became dominant at g3-g4 only when both the Re and particle sizes were high. In addition, the highest DE reached at g3-g4 was only 7.26% for C3 whereas that in the parabolic profile, the highest DE reached was 12.9%. At low Re, the DE in g4-1 was greater than g4-2 for C2 while the reverse was true for C3. This was in contrast to the trend as observed for the parabolic profile. However as Re and particle size increased, deposition seemed to be higher in the

branch that gave a larger bifurcation angle. It was observed that, similar to the parabolic profile, deposition of particles was greater in the median branches of G5 as the Re and particle size increased.

Polydispersed Parabolic Inlet Release Profile

The last release profile was polydispersed parabolic in which particle sizes of 1, 3 and 5μm were used in the simulation. Comparisons of the deposition pattern for this profile would be compared to that of the monodispersed ones. The following graphs illustrated the particle deposition patterns for various configurations at different Re and particle sizes when the release profile was polydispersed parabolic.

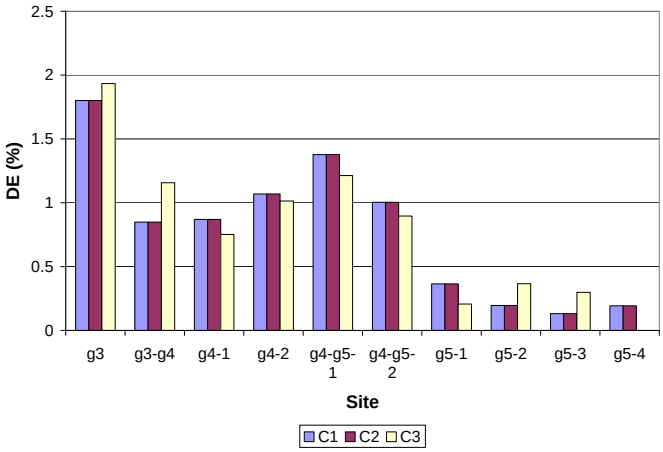

(a)

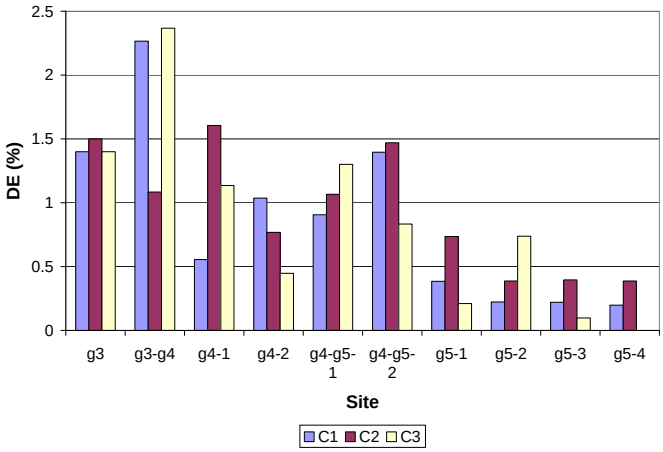

(b)

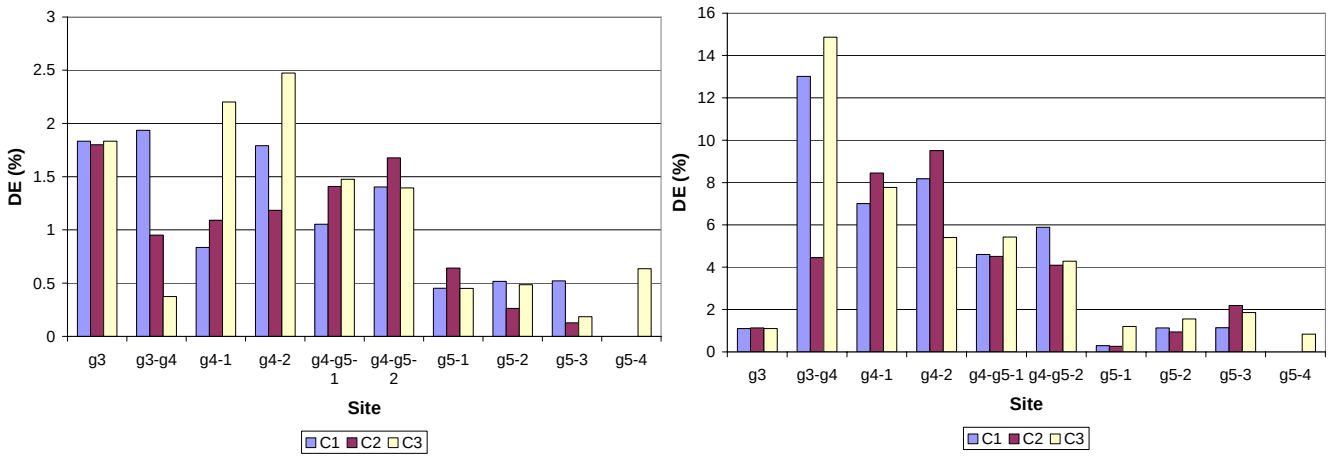

Fig. 4.19: Particle deposition patterns in various configurations for (a) d_p = 1µm, Re = 514, (b) d_p = 5µm, Re = 514, (c) d_p = 1µm, Re = 2194, and (d) d_p = 5µm, Re = 2194, when the release profile was polydispersed parabolic.

Similar to the previous two profiles, particles were mainly deposited at g3 when the particle size and Re were low. Deposition at g3-g4 became dominant only when the particle size was large. The highest DE reached at g3-g4 was 14.9% for C3 at high Re and large particle size and this value was greatest among the three profiles. It was observed that only at high Re and large particle size, deposition was higher in the bifurcation with a greater bifurcation angle. Similar to both the previous profiles, deposition was greater in the median G5 branches than the lateral ones as Re and particle size increased.

4.6 Practical Significance of Results

It was shown in this study that geometrical asymmetry in the human lungs could affect the airflow and particle deposition patterns. An increase in the bifurcation angle between the mother branch and a daughter branch caused larger flow in the affected branch. A larger flow would imply that more particles could flow into the affected branch and the probability of the particles getting deposited on the walls would

increase accordingly. However, this was found to be dependent on inlet particle release profile, the activity level of the subject and the particle sizes involved. For instance, particle deposition was generally higher in the branch having a higher bifurcation angle when the inlet particle release profile was monodispersed parabolic. When the profile was polydispersed parabolic, deposition was only higher in the branch having a higher bifurcation angle if the activity level or Re number and the particle size were high. These results could serve as a guide when developing global lung deposition models for exposure-dose relationship and subsequently for dose-effect analysis in therapeutic drug delivery systems as well as evaluating the health risk in inhalation toxicology.

5. Conclusions

The effects of bifurcation angle between a branch in Generation 4 and Generation 3, and the particle release profile at the inlet on the air flow fields and particle deposition patterns had been investigated using a double bifurcation simulating Generation 3 to Generation 5 in the human lungs. Analysis of the mid-plane axial flow fields revealed that recirculation occurred near the outer walls of bifurcation of G4 at Re = 2194 for C1 and C2 while it occurred earlier at Re = 1070 for C3. The flow was larger in the bifurcation that had a higher bifurcation angle with the mother branch and the median branches in G5 received a larger proportion of flow than the lateral branches.

Double primary vortices were observed in the secondary flow fields in G4 branches and the intensity of these vortices increased with increasing bifurcation angle. With an increase in Re number, the vortices moved closer to the outer wall of bifurcation. The high axial velocity near the inner walls of bifurcation began to engulf the low axial velocity regions near to the outer walls of bifurcation as flow entered the branches of G4. The degree of engulfment in the affected branch of G4 increased with increasing bifurcation angle. As the flow proceeded downstream in G4, the vortices shifted back towards the center of the bifurcation. In the branches of G5, weak secondary vortices began to appear with higher intensity in the median branches as compared to the lateral branches since more flow entered the median branches. Secondary vortices became distinct at certain Re number for different configuration. For example, secondary vortices were only noticeable at Re = 1070 for C3 in g5-2-1 but for C1 and C2, it became only obvious at Re = 2194.

The overall particle deposition efficiency (DE) was plotted against the Stk number for each particle release profile at the inlet to investigate the effects of the release profile on the overall DE. It was found that at low Stk (< 0.01), only subtle differences existed between various configurations. However, as Stk increased, the differences in the overall DE between the configurations increased. Maximum difference in the overall DE could be seen between C1 or C3 and C2 but relatively insignificant difference existed between C1 and C3. This might be attributed to the significant increase in intensity of the vortices as the bifurcation angle increased. Monodispersed homogeneous particle release profile would give the largest maximum difference between the various configurations. Polydispersed parabolic release profile would give the highest overall DE at over 25% at high Stk while the monodispersed homogeneous release profile would give the lowest overall DE at under 20%.

The particle deposition patterns showed several interesting features between various release profiles. All the release profiles showed that at low Re and with small particles (~ 1μm), deposition occurred mainly in the mother branch in G3. For profiles that were parabolic, an increase in either the Re number or the particle size would cause predominant deposition at the first bifurcation transition for two of the configurations, C1 and C3. For the monodispersed homogeneous release profile, predominant deposition at the first bifurcation transition occurred only when both the Re number and the particle size were high. Deposition was higher in the branch that had a higher bifurcation angle when the release profile was monodispersed parabolic with the exception of C2 at high Re and small particle size. However, for the monodispersed homogeneous and the polydispersed parabolic profiles, deposition was higher in the branch with a larger bifurcation angle only when both the Re number and the particle

size were high. The maximum DE reached at any one site was 14.9% when the profile was polydispersed parabolic and this value was the highest among all the three profiles with the monodispersed homogeneous profile giving the lowest value of 7.26%. In all the three profiles, DE in the median branches of G5 was greater than that in the lateral ones especially at high Re and large particle size.

To conclude, this study suggested that the geometrical asymmetry and the particle release profile did have some effects on the flow structures as well as the particle deposition in Generations 3 to 5 in the human airways, and this might in turn affect the therapeutic effect in drug delivery to the targeted sites as well as the risk assessment of airborne particulate pollutants in inhalation toxicology. However, the simulated work here should only serve as a guide on the possible implications of geometrical asymmetry and particle release profile on the particle deposition. The results of which should be verified against experimental works of the same configurations and this would serve as the next step for the research.

6. References

Agrawal, Y., Talbot, L., Gong, K., 1978, J. Fluid Mech., 85, 3 , pp. 497 – 518.

Balashazy, I., Hofmann, W., 2000, Health Physics, 78, 2, pp. 147 – 158.

Balashazy, I., Hofmann, W., Martonen, T. B., 1991, J. Aerosol Sci., 22, 1, pp. 15 – 30.

Cai, F. S., Yu, C. P., 1988, J. Aerosol Sci., 19, pp. 679 – 688.

Comer, J. K., Kleinstreuer, C., Hyun, S., Kim, C. S., 2000, J. Biomech. Eng., 122, pp. 152 – 158.

Comer, J. K., Kleinstreuer, C., Kim, C. S., 2001, J. Fluid Mech., 435, pp. 55 – 80.

Comer, J. K., Kleinstreuer, C., Zhang, Z., 2001, J. Fluid Mech., 435, pp. 25 – 54.

Dean, W. R., 1927, Phil. Mag., S. 7, 4, pp. 208 – 223.

Dean, W. R., 1928, Phil. Mag., S. 7, 5, pp. 674 – 695.

Ertbruggen, C., Hirsch, C., Paiva, M., 2005, J. Appl. Physiol., 98, pp. 970 – 980.

Fontana, D., Vanni, M., Baldi, G., 2005, The Int. J. Artificial Organs, 28, 7, pp. 667 – 677.

Guan, X., Martonen, T. B., 2000, J. Aerosol Sci., 31, 7, pp. 833 – 847.

Hinds, W. C., 1982, Aerosol Technology, Wiley, New York.

Horsfield, K, Cumming, G., 1967, Bull. Math. Biophys., 29, pp. 245 – 259.

Horsfield, K., Dart, G., Olson, D. E., Filley, G. F., Cumming, G., 1971, J. Appl. Physiol., 31, pp. 207 – 217.

Kim, C. S., Fisher, D. M., 1999, Aerosol Sci. Tech., 31, pp. 198 – 220.

Kim, C. S., Fisher, D. M., Lutz, D. J., Gerrity, T. R., 1994, J. Aerosol Sci., 25, 3, pp. 567 – 581.

Kim, C. S., Iglesias, A. J., 1989a, J. Aerosol Med., 2, pp. 1 – 14.

Kleinstreuer, C., 2001, J. Med. Eng. Tech., 25, 3, pp. 127.

Landahl, H. D., 1950, Bull. Math. Biophys., 12, pp. 43 – 56.

Lee, J. W., Goo, J. H., 1992, J. Aerosol Med., 5, pp. 131 – 154.

Lee, J. W., Goo, J. H., Chung, M. K., 1996, J. Aerosol Sci., 27, 1, pp. 119 – 138.

Liu, Y., So, R. M. C., Zhang, C. H., 2003, J. Biomech., 36, pp. 951 – 959.

Martonen, T. B., Guan, X., Schreck, R. M., 2001, Inhal. Toxicol., 13, pp. 291 – 305.

Nowak, N. K., Annapragada, P. P., Ananth, V., 2003, Ann. Biomed. Eng., 31, 4, pp. 374 – 390.

Phillips, C. G., Kaye, S. R., 1997, Respir. Physiol., 107, pp. 85 – 98.

Phillips, C. G., Kaye, S. R., Schroter, R. C., 1994, Respir. Physiol., 98, pp. 219 – 226.

Sauret, V., Halson, P. M., Brown, I. W., Fleming, J. S., Bailey, A. G., 2002, J. Anat., 200, pp. 123 – 134.

Soh, W. Y., Berger, S. A., 1984, J. Fluid Mech., 148, pp. 109 – 135.

Synder, B., Hammersley, J. R., Olson, D. E., 1985, J. Fluid Mech., 161, pp. 281 – 294.

Weibel, E. R., 1963, Morphometry of the Human Lung, Academic.

Yeh, H. C., 1974, Bull. Math. Biophys., 36, pp. 105 – 116.

Yeh, H. C., Schum, G. M., 1980, Bull. Math. Biol., 42, pp. 461 – 480.

Zhang, Z., Kleinstreuer, C., Kim, C. S., 2002, Int. J. Multiphase Flow, 28, pp. 1021 – 1046.

Zhao, Y., Brunskill, C. T., Lieber, B. B., 1997, J. Biomech. Eng., 119, pp. 52 – 58.

Zhao, Y., Lieber, B. B., 1994, J. Biomech. Eng., 116, pp. 488 – 496.

Appendix

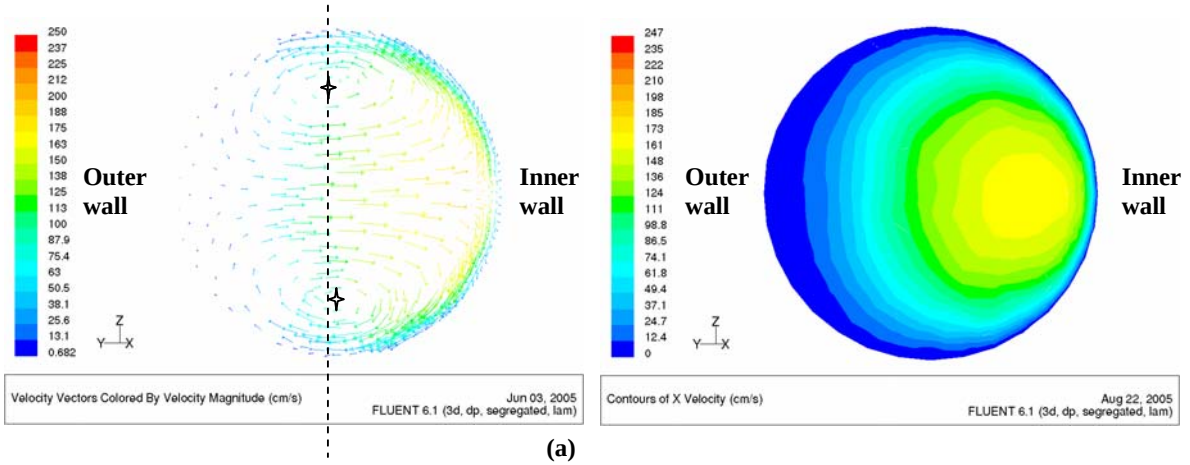
250
237
225
212
200
188
175
163
150
138
125
113
100
87.9
75.4
63
50.5
38.1
25.6
13.1
0.682
Outer wall
Inner wall
Velocity Vectors Colored By Velocity Magnitude (cm/s)
Jun 03, 2005
FLUENT 6.1 (3d, dp, segregated, lam)
247
235
222
210
198
185
173
161
148
136
124
111
98.8
86.5
74.1
61.8
49.4
37.1
24.7
12.4
0
Outer wall
Inner wall
Contours of X Velocity (cm/s)
Aug 22, 2005
FLUENT 6.1 (3d, dp, segregated, lam)

(a)

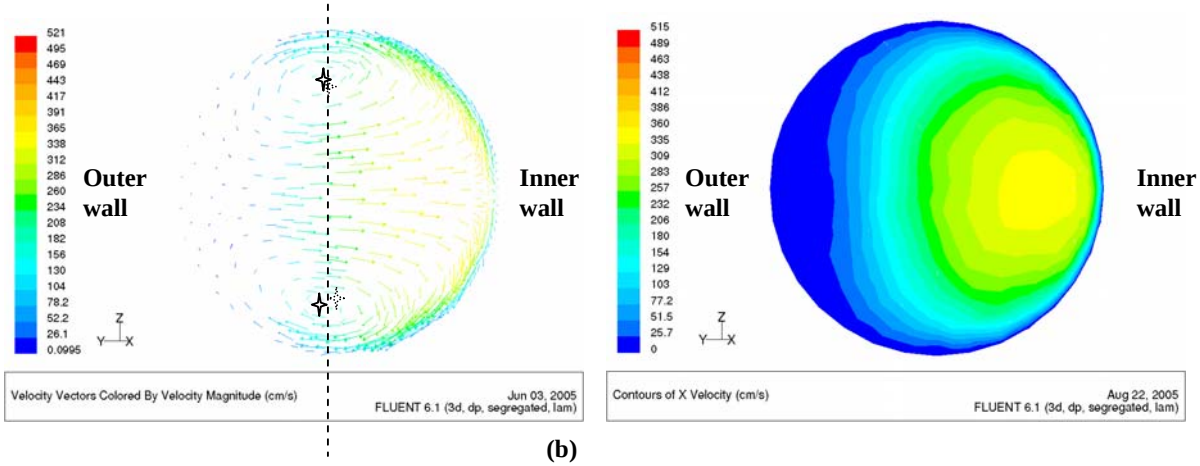
521
495
469
443
417
391
365
338
312
286
260
234
208
182
156
130
104
78.2
52.2
26.1
0.0995
Outer wall
Inner wall
Velocity Vectors Colored By Velocity Magnitude (cm/s)
Jun 03, 2005
FLUENT 6.1 (3d, dp, segregated, lam)
515
489
463
438
412
386
360
335
309
283
257
232
206
180
154
129
103
77.2
51.5
25.7
0
Outer wall
Inner wall
Contours of X Velocity (cm/s)
Aug 22, 2005
FLUENT 6.1 (3d, dp, segregated, lam)

(b)

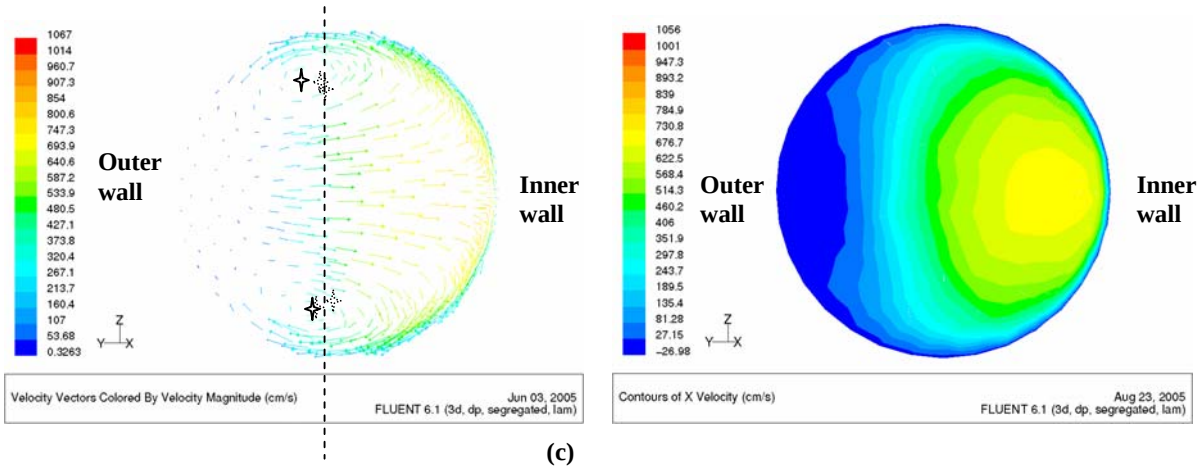

(c)

Fig. A.1: Velocity vectors and contours at g4-1-1 for C1 at (a) Re = 514, (b) Re = 1070, and (c) Re = 2194. The dashed line on the velocity vector plots served as a gage for comparing the location of the centers of vortices for the vector plots at various Re. The stars represented the centers of the vortices and the dashed stars illustrated how the centers of vortices had moved with Re.

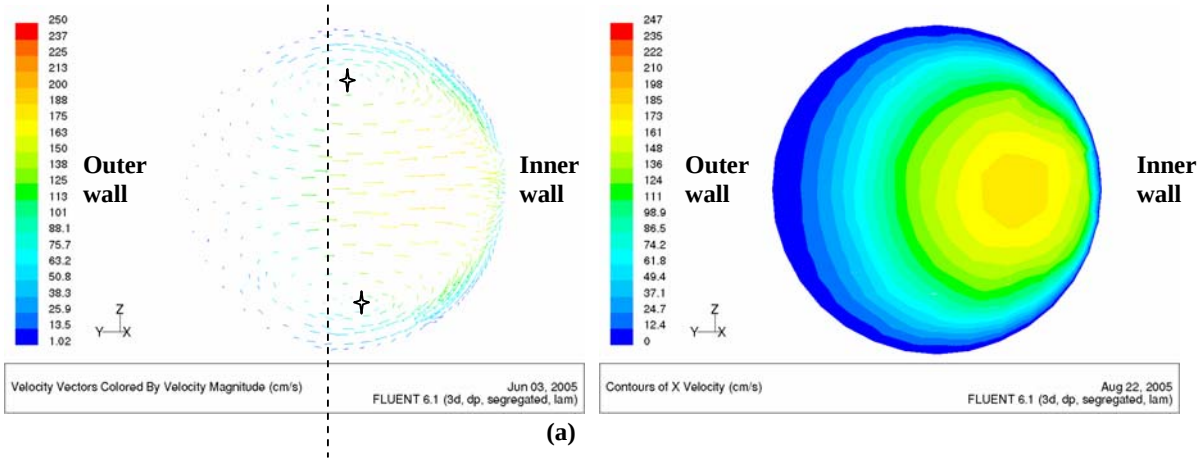

(a)

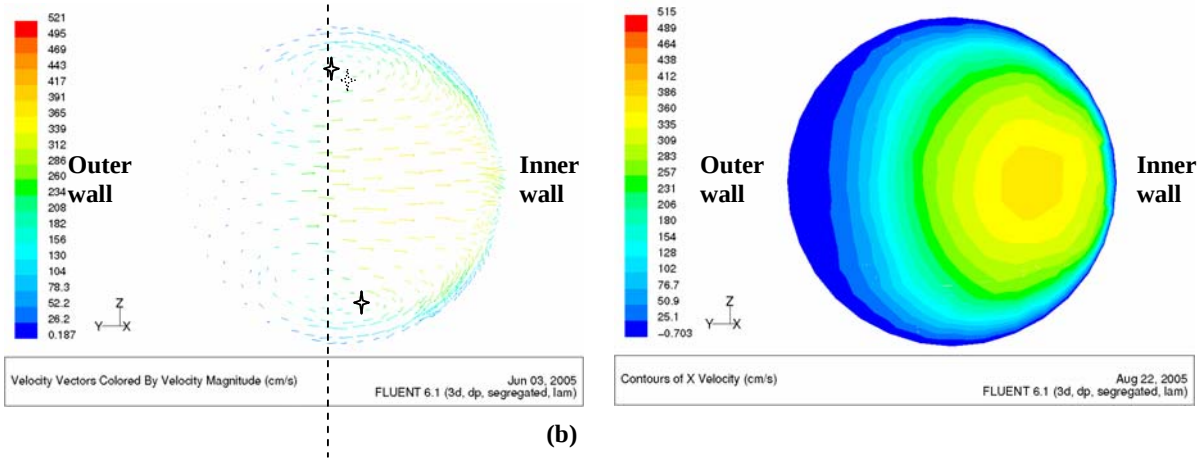

(b)

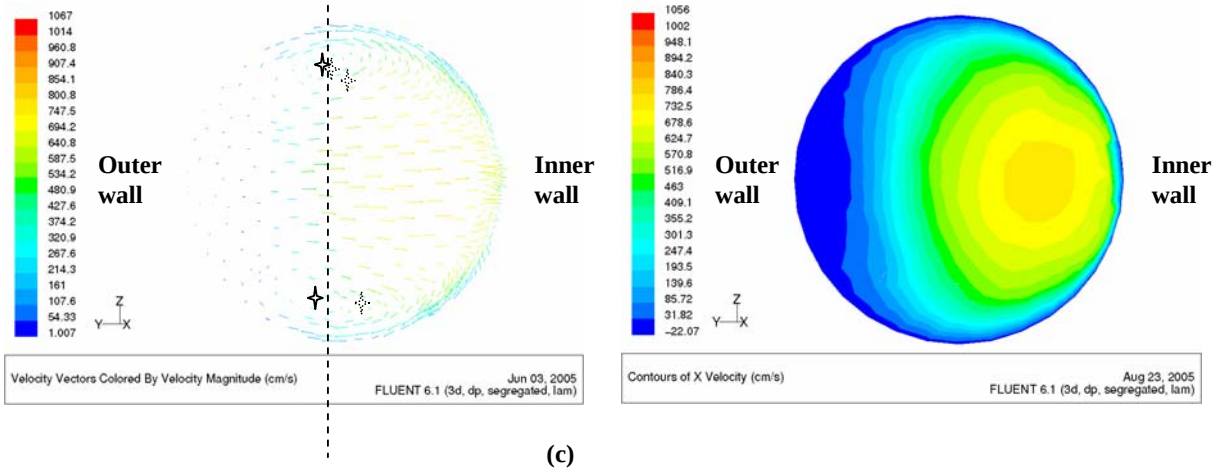

(c)

Fig. A.2: Velocity vectors and contours at g4-1-1 for C2 at (a) Re = 514, (b) Re = 1070, and (c) Re = 2194.

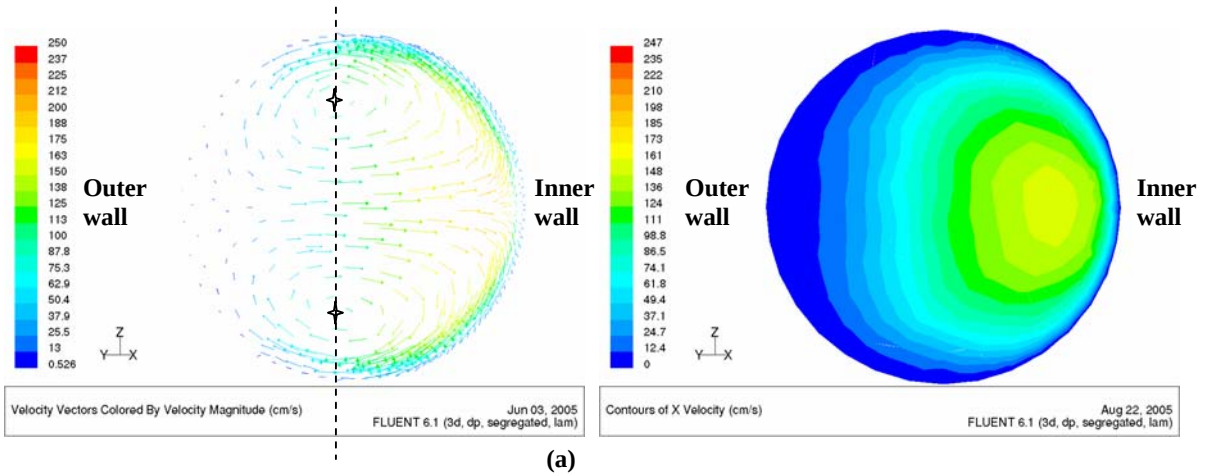

(a)

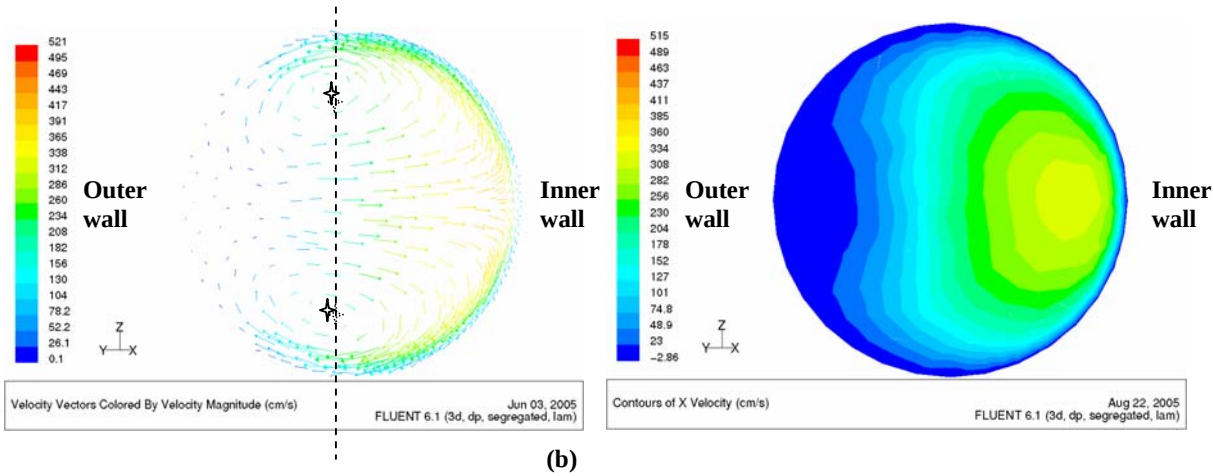

(b)

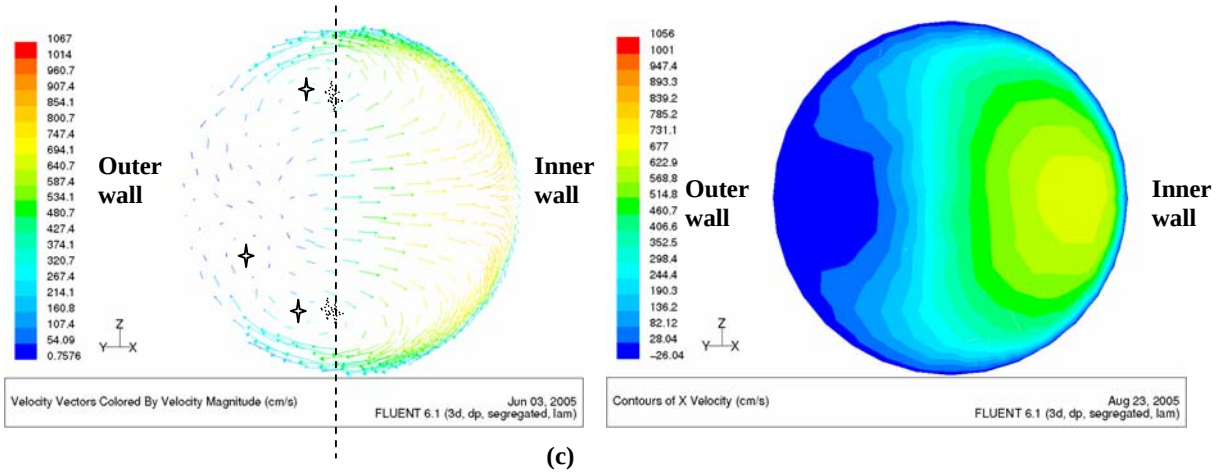

(c)

Fig. A.3: Velocity vectors and contours at g4-1-1 for C3 at (a) Re = 514, (b) Re = 1070, and (c) Re = 2194. From Re = 1070 onwards, negative values began to appear for the velocity contours of C3 indicating the presence of backflow or recirculation.

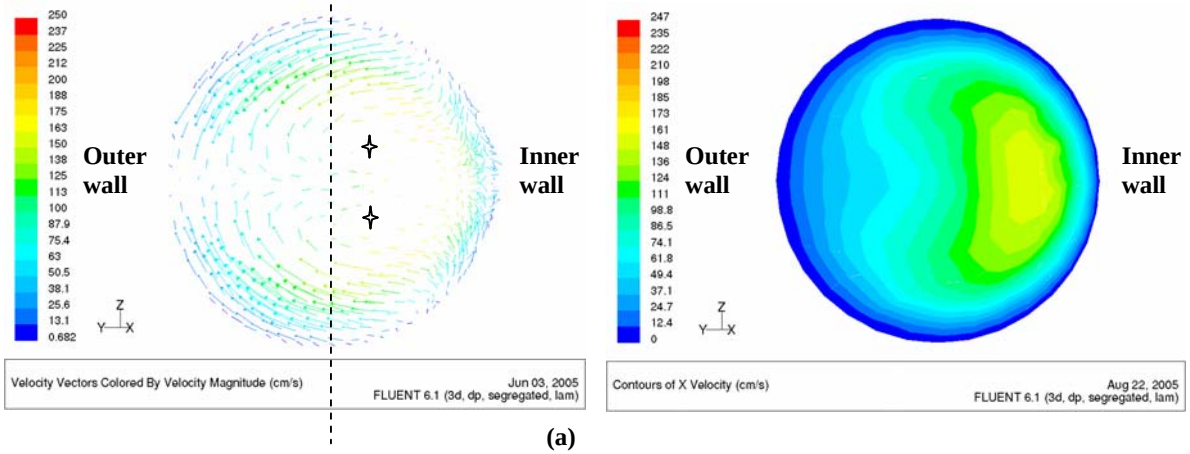

(a)

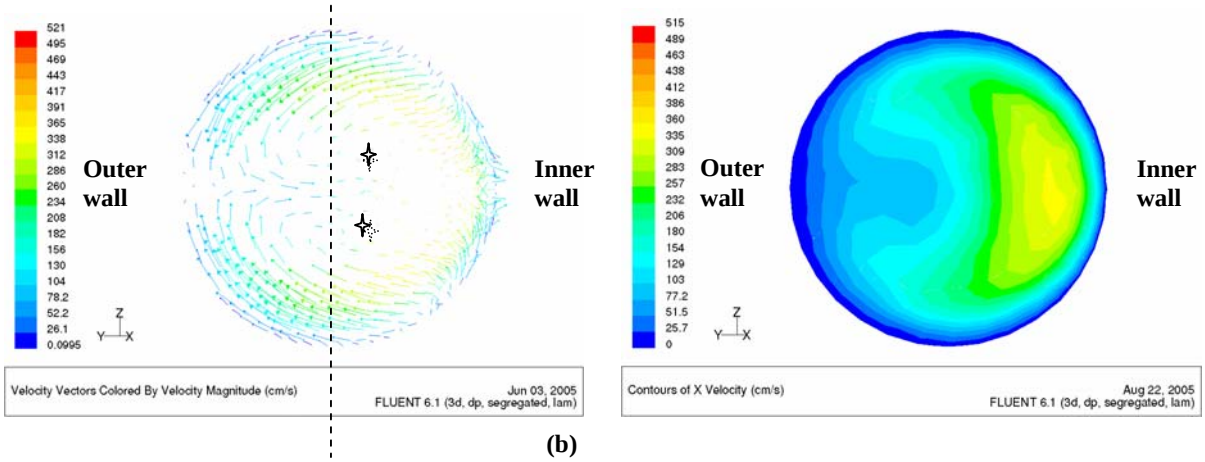

(b)

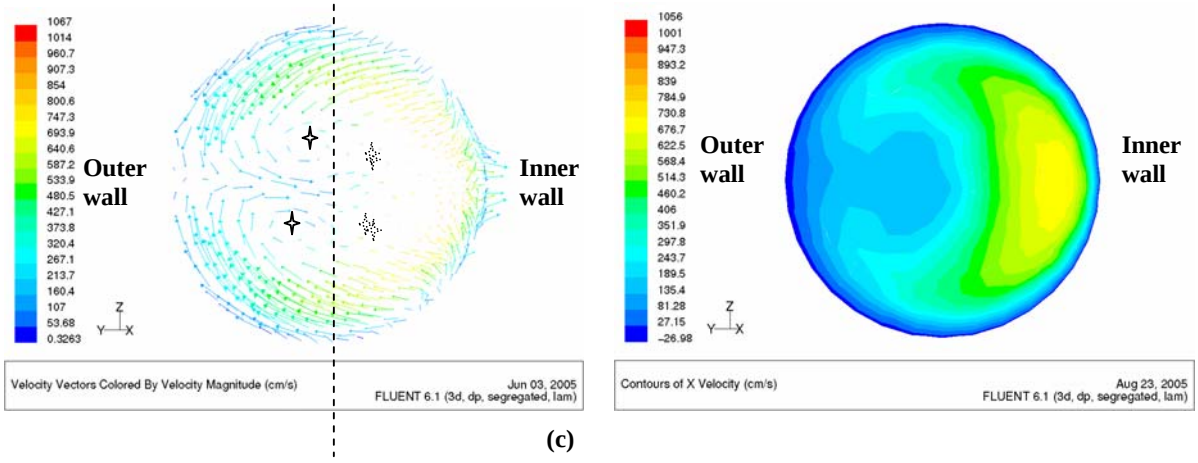

(c)

Fig. A.4: Velocity vectors and contours at g4-1-2 for C1 at (a) Re = 514, (b) Re = 1070, and (c) Re = 2194.

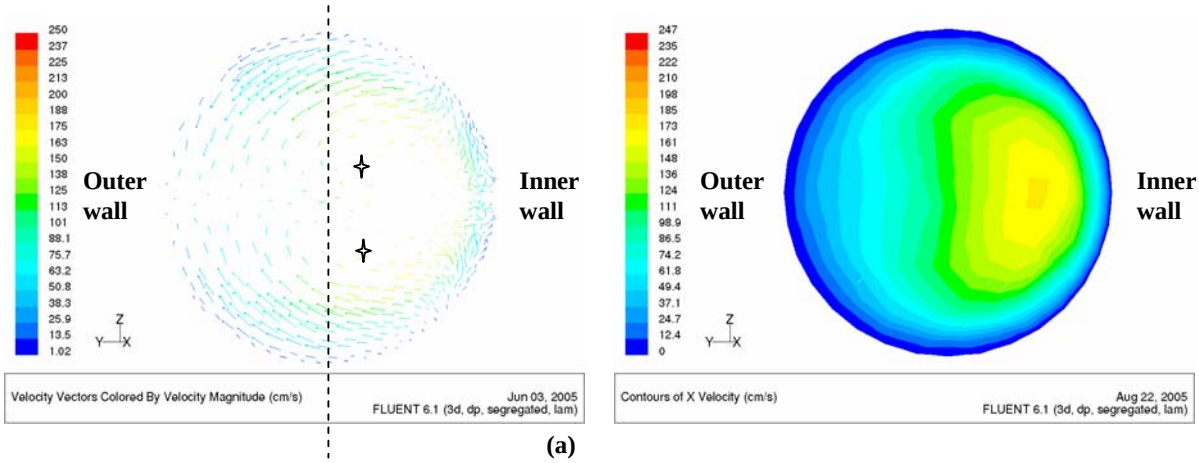

(a)

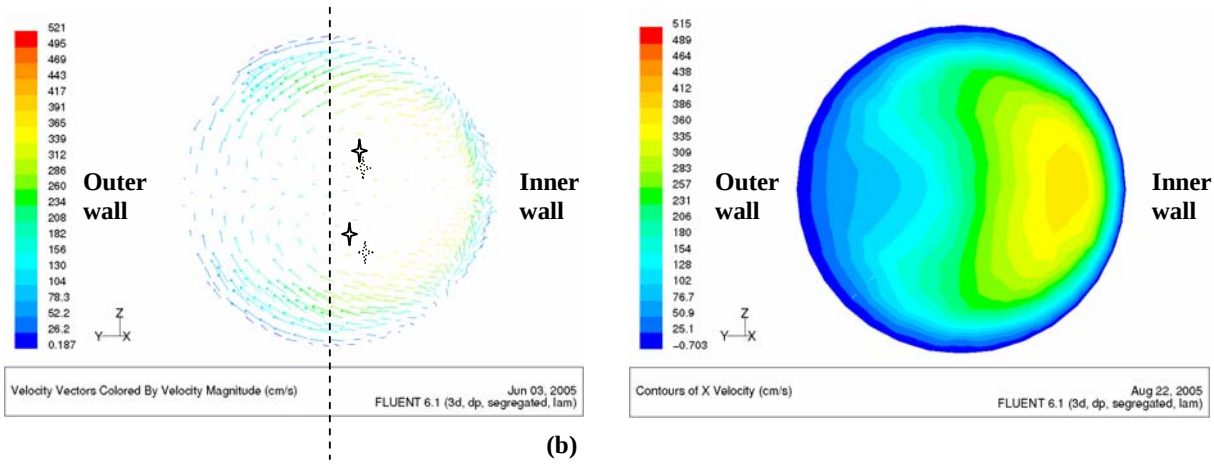

(b)

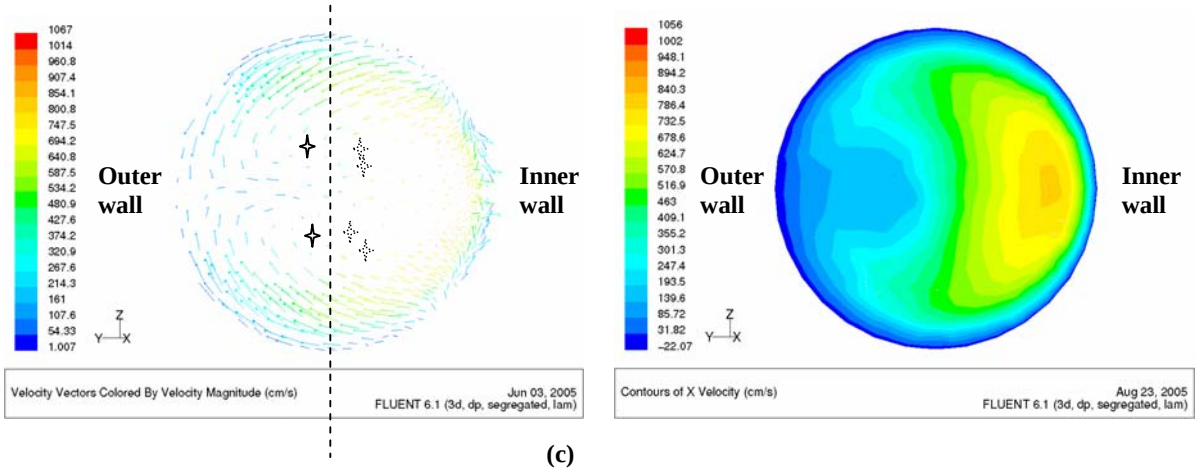

(c)

Fig. A.5: Velocity vectors and contours at g4-1-2 for C2 at (a) Re = 514, (b) Re = 1070, and (c) Re = 2194.

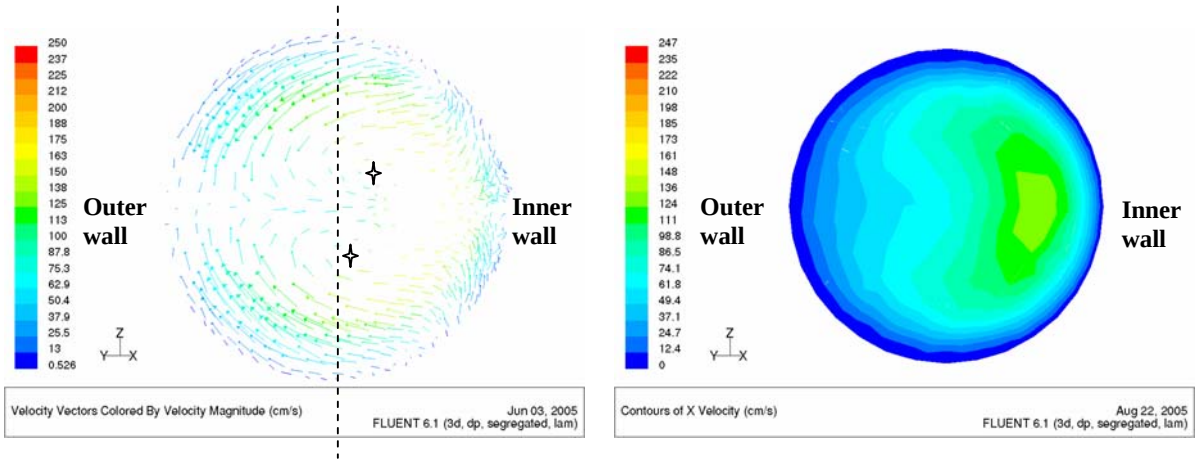

(a)

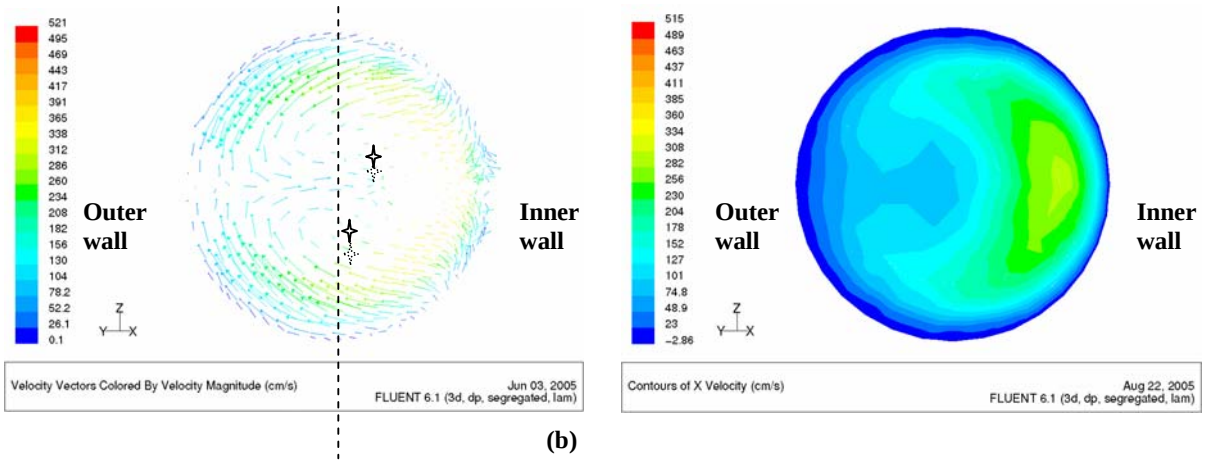

(b)

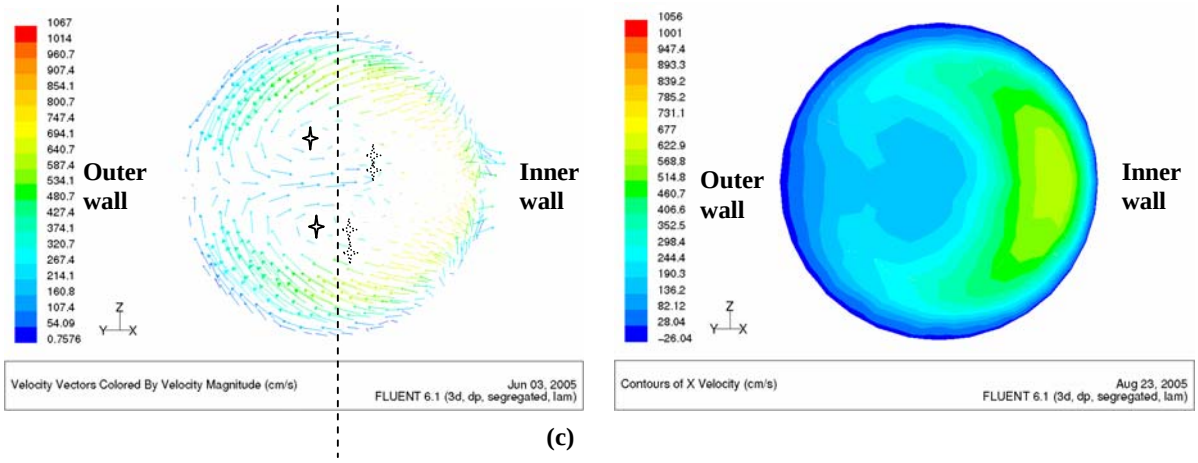

(c)

Fig. A.6: Velocity vectors and contours at g4-1-2 for C3 at (a) Re = 514, (b) Re = 1070, and (c) Re = 2194.

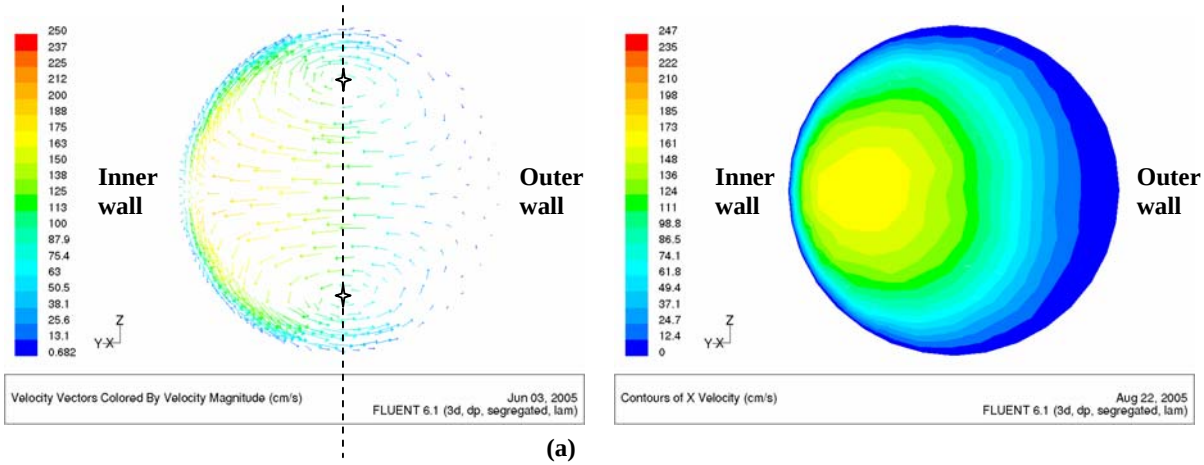

(a)

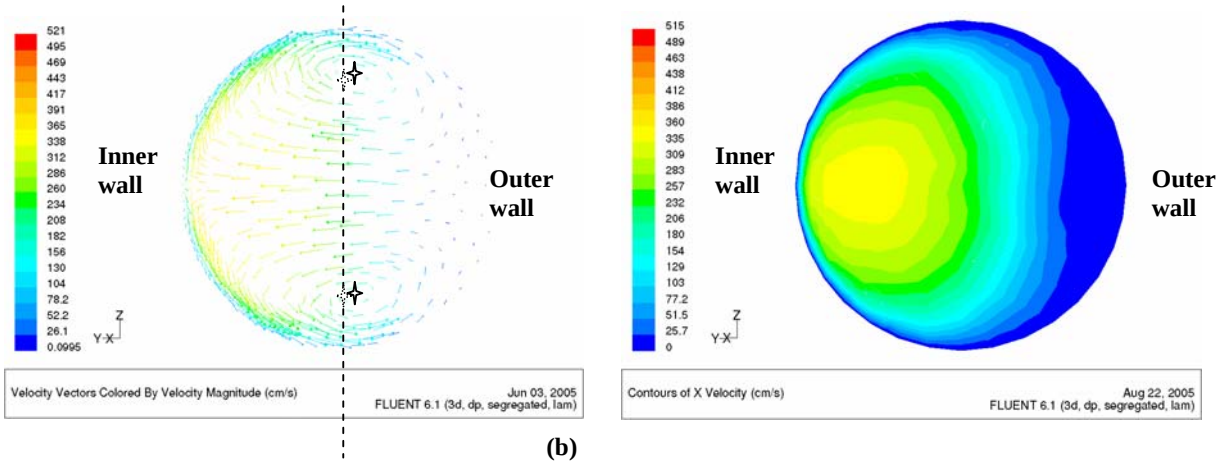

(b)

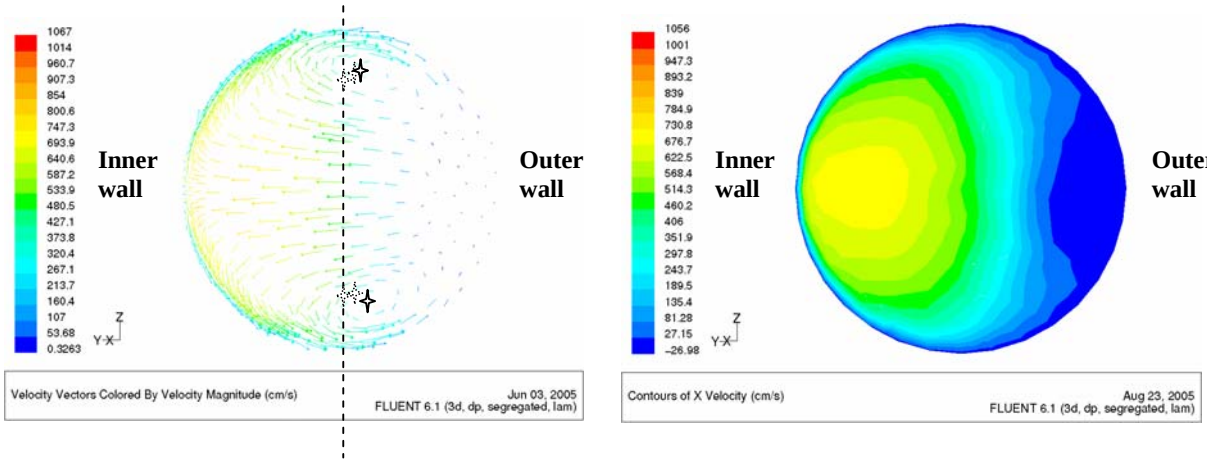

(c)

Fig. A.7: Velocity vectors and contours at g4-2-1 for C1 at (a) Re = 514, (b) Re = 1070, and (c) Re = 2194.

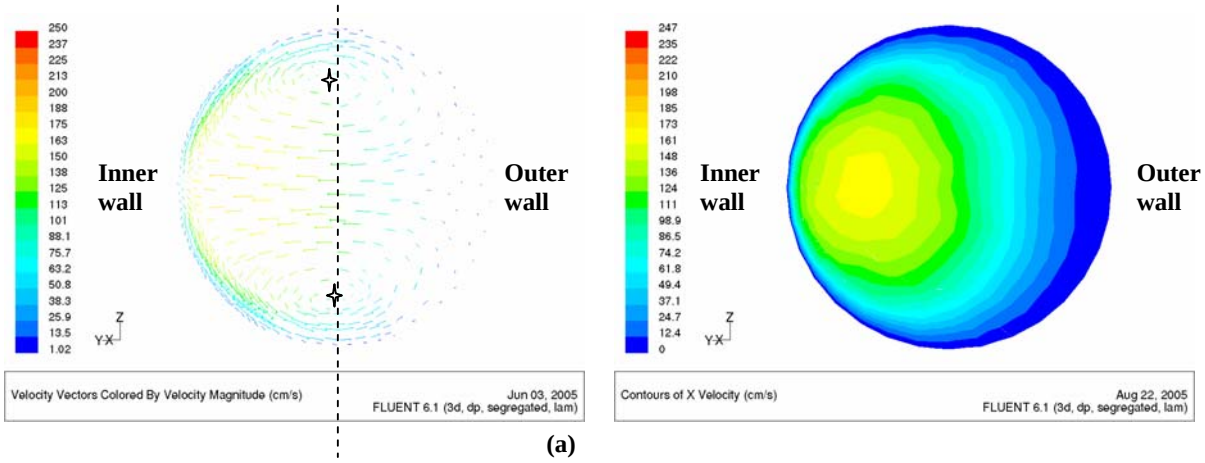

(a)

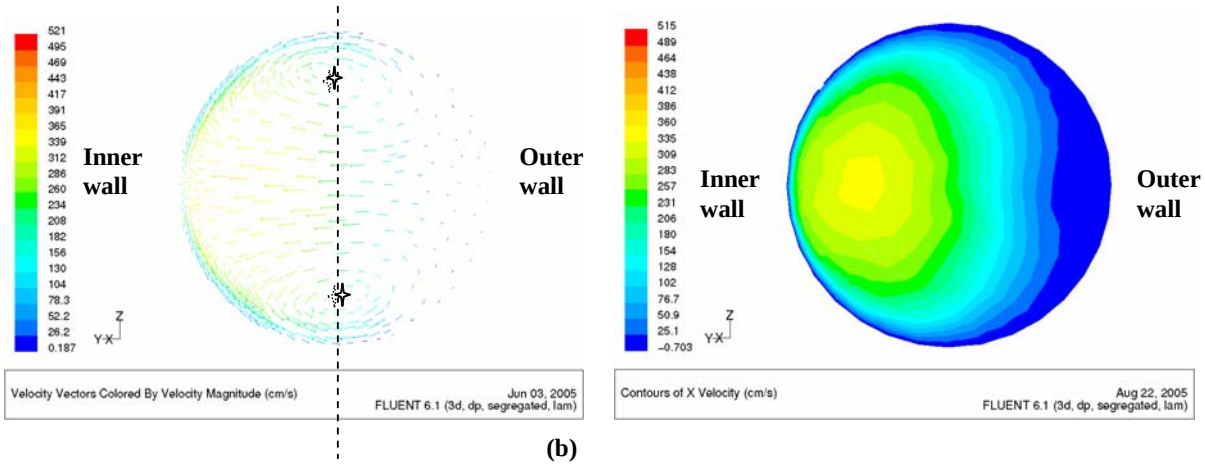

(b)

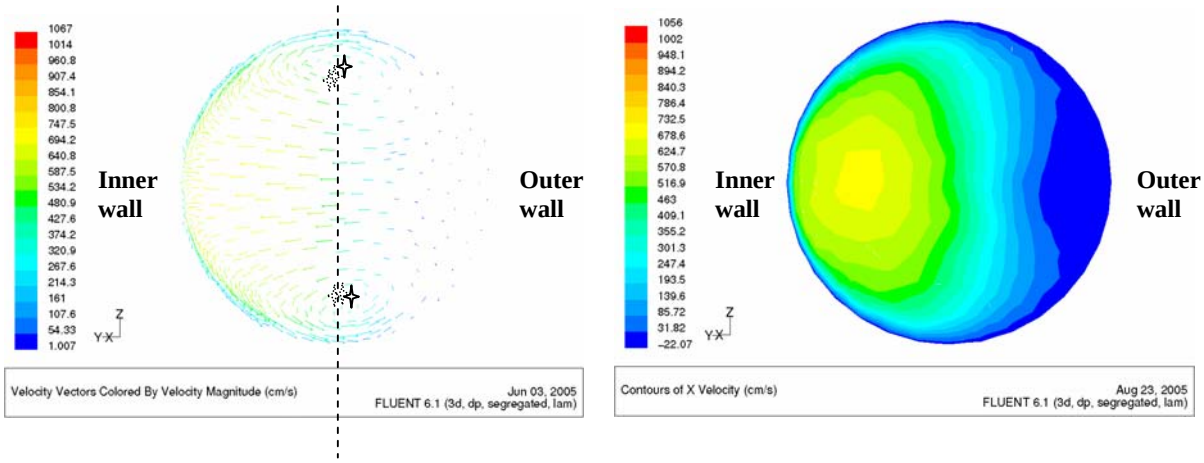

(c)

Fig. A.8: Velocity vectors and contours at g4-2-1 for C2 at (a) Re = 514, (b) Re = 1070, and (c) Re = 2194.

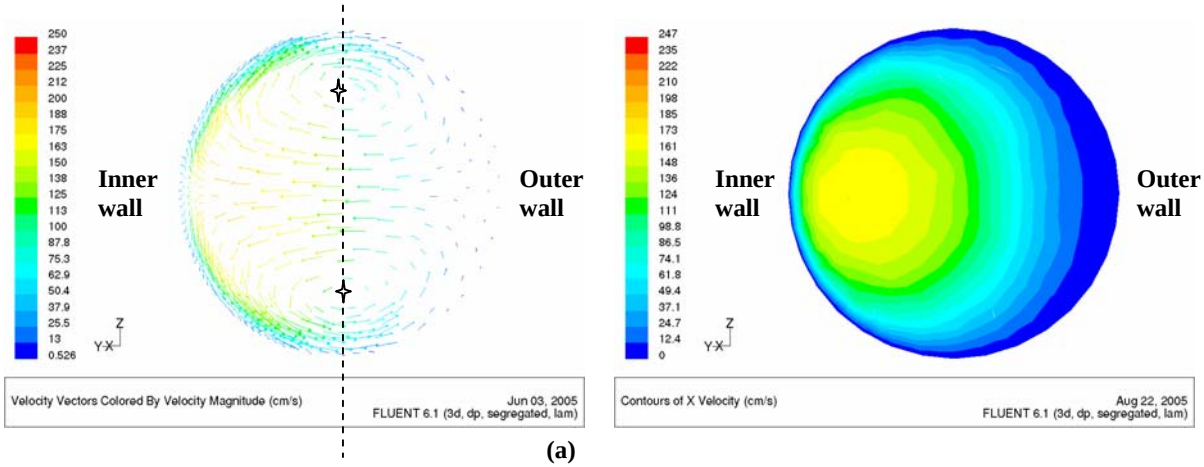

(a)

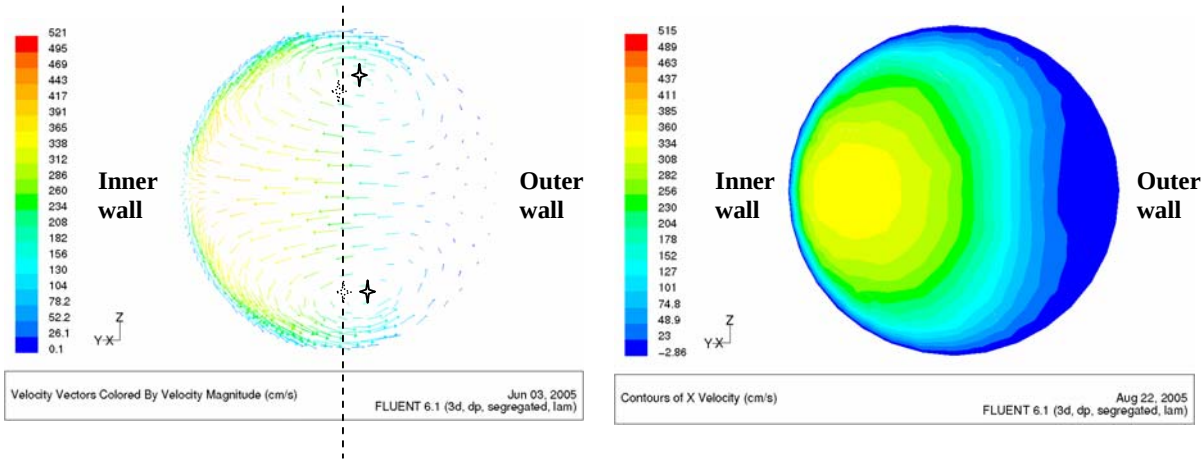

(b)

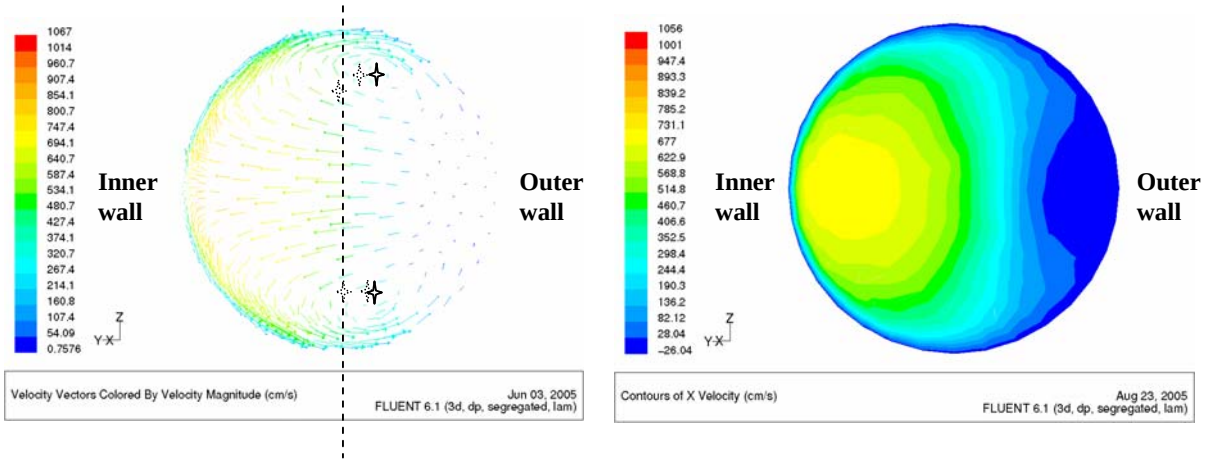

(c)

Fig. A.9: Velocity vectors and contours at g4-2-1 for C3 at (a) Re = 514, (b) Re = 1070, and (c) Re = 2194.

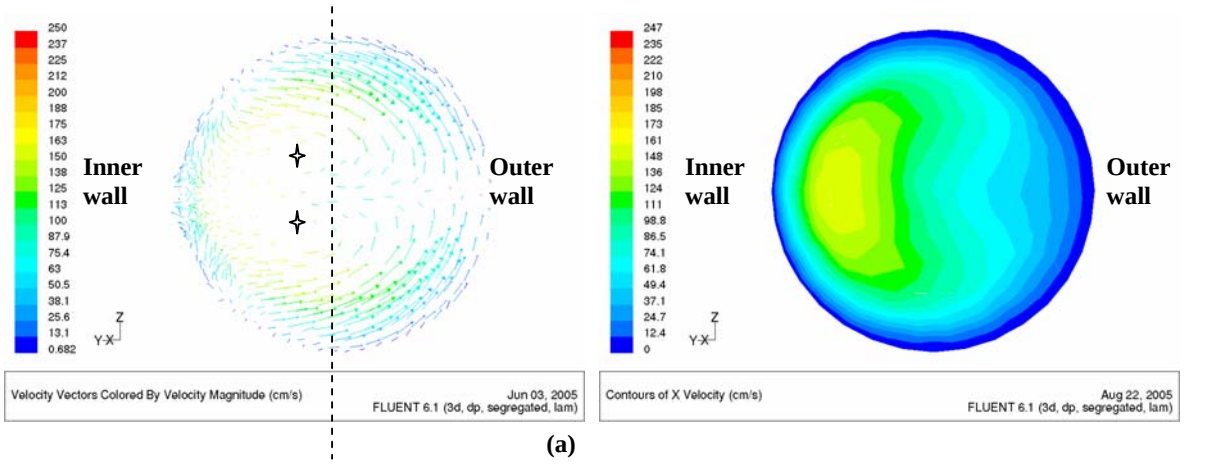

(a)

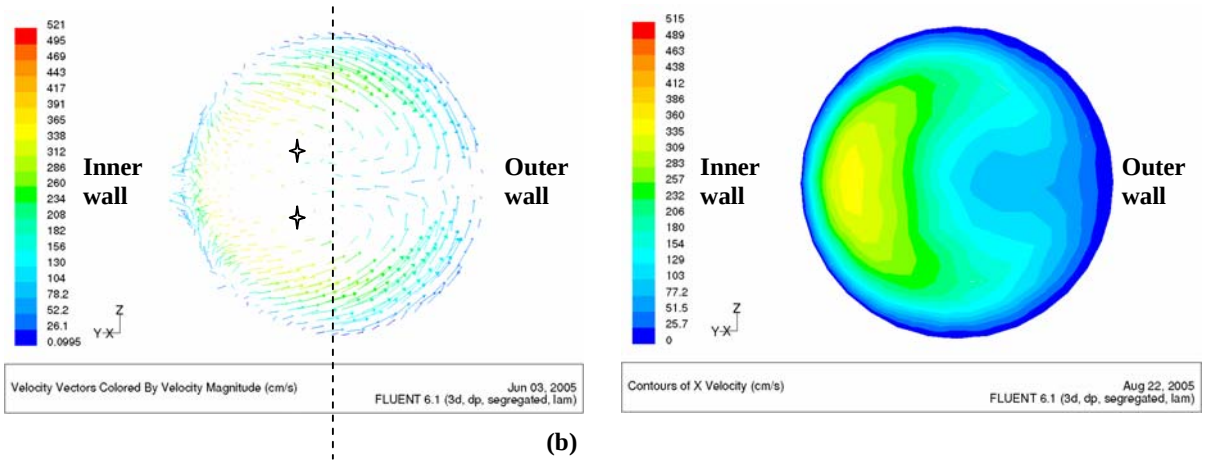

(b)

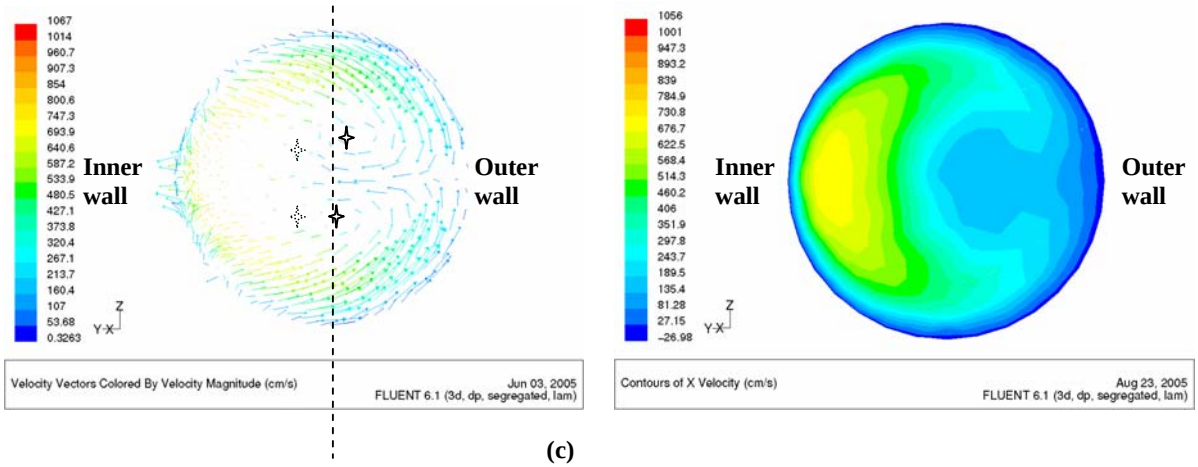

(c)

Fig. A.10: Velocity vectors and contours at g4-2-2 for C1 at (a) Re = 514, (b) Re = 1070, and (c) Re = 2194.

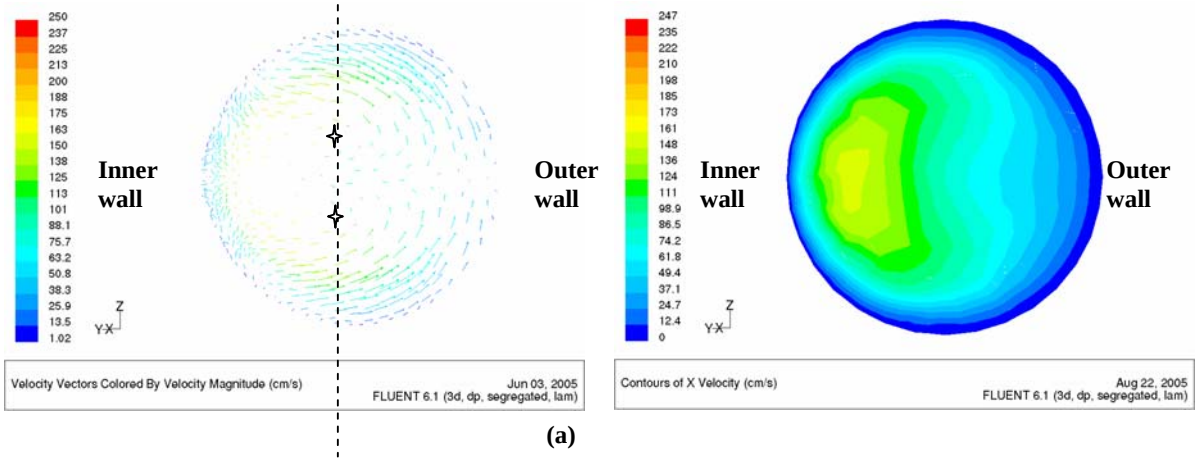

(a)

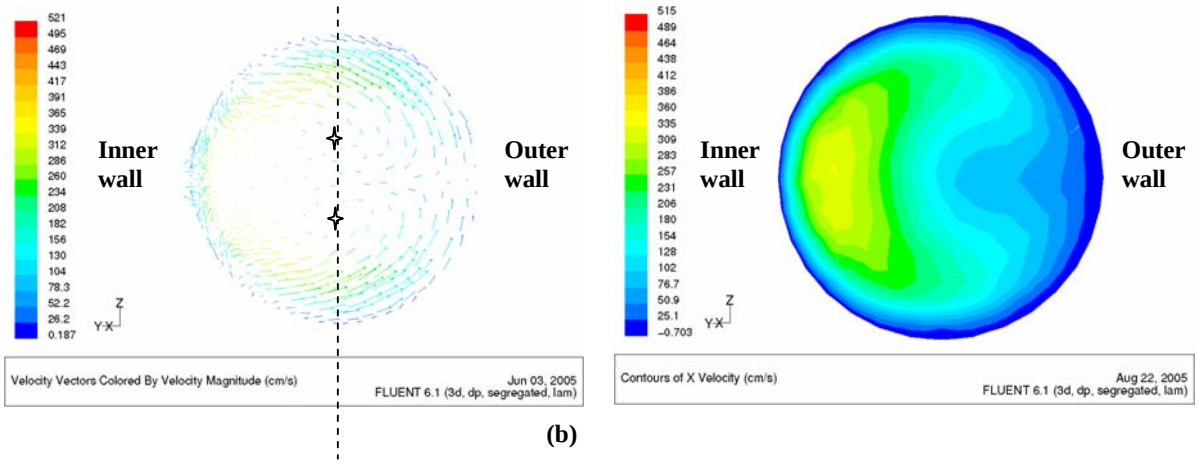

(b)

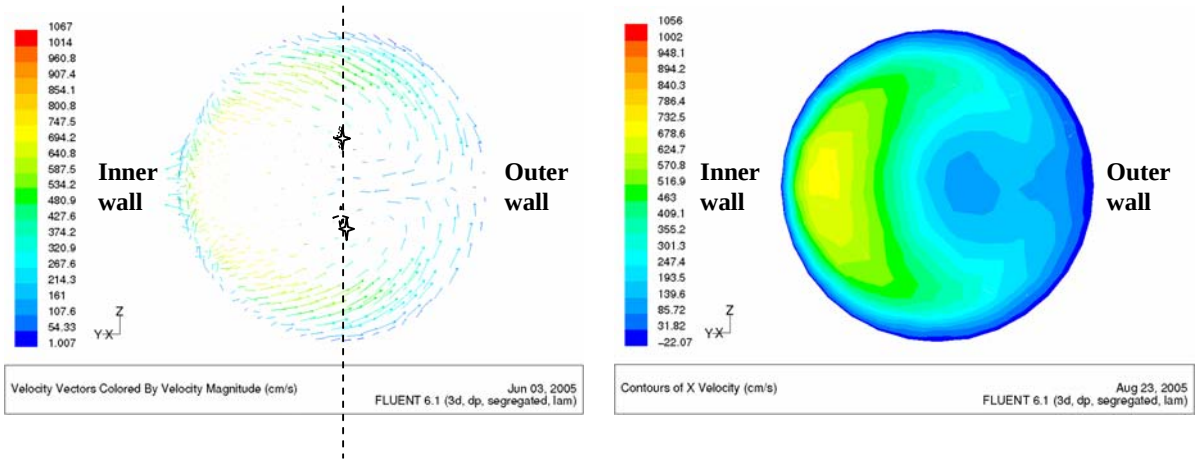

(c)

Fig. A.11: Velocity vectors and contours at g4-2-2 for C2 at (a) Re = 514, (b) Re = 1070, and (c) Re = 2194.

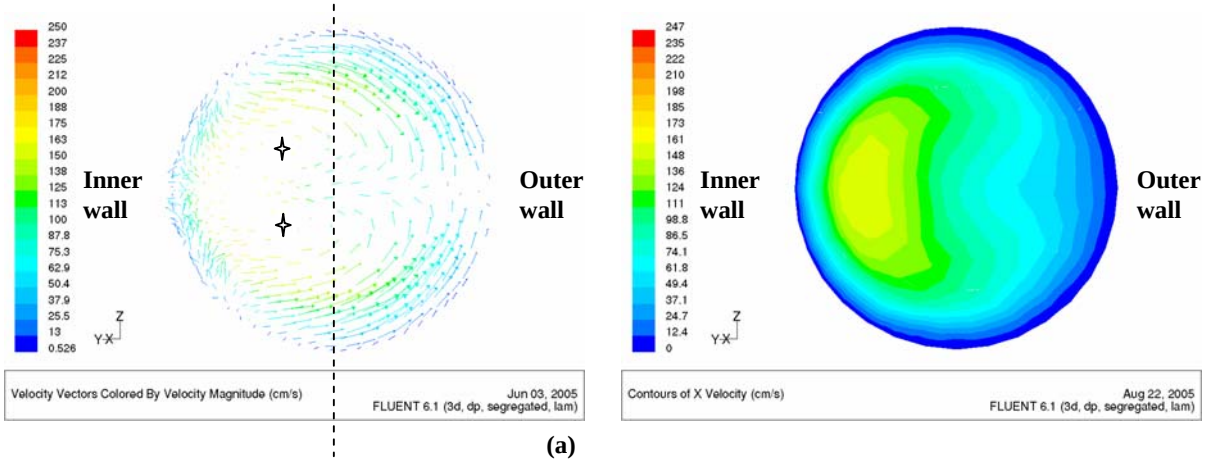

(a)

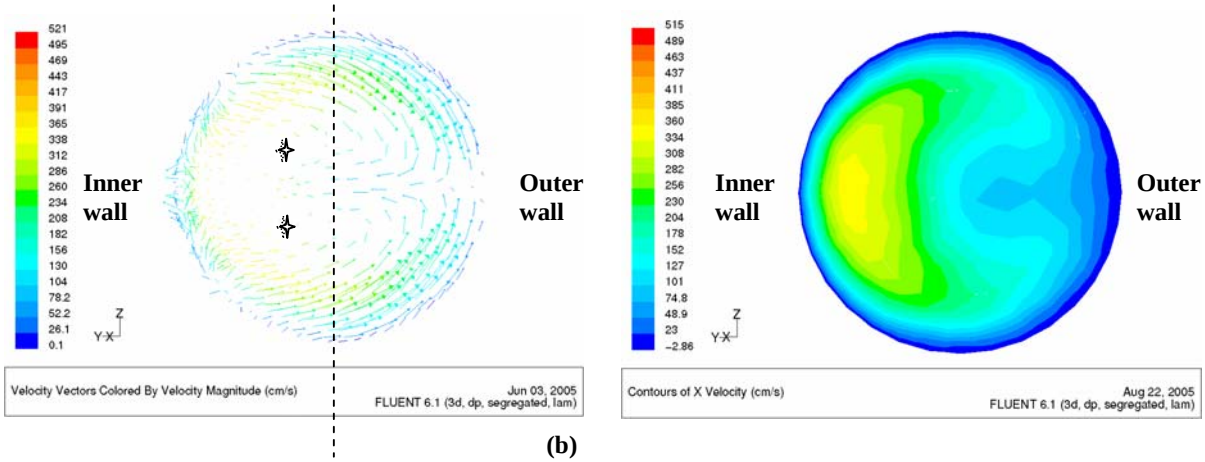

(b)

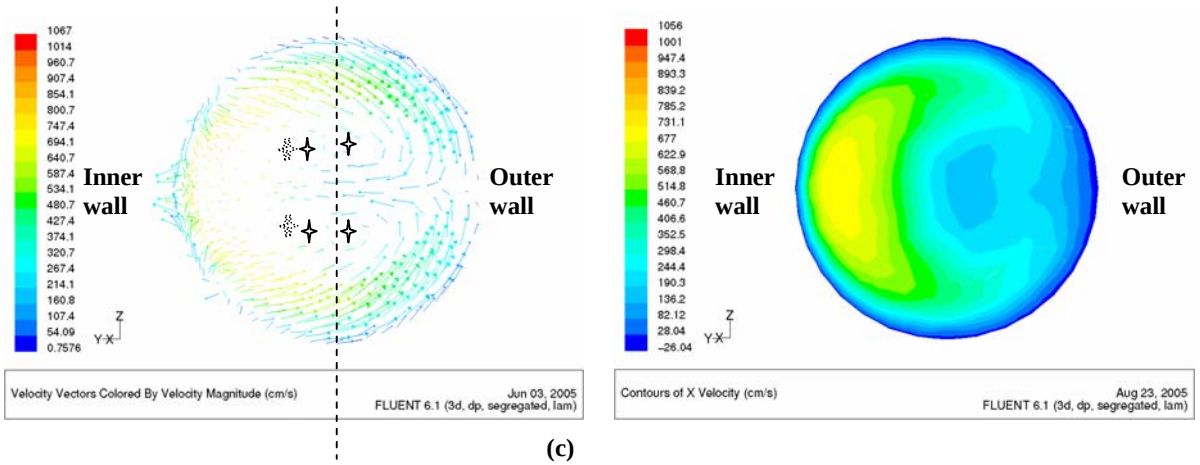

(c)

Fig. A.12: Velocity vectors and contours at g4-2-2 for C3 at (a) Re = 514, (b) Re = 1070, and (c) Re = 2194.

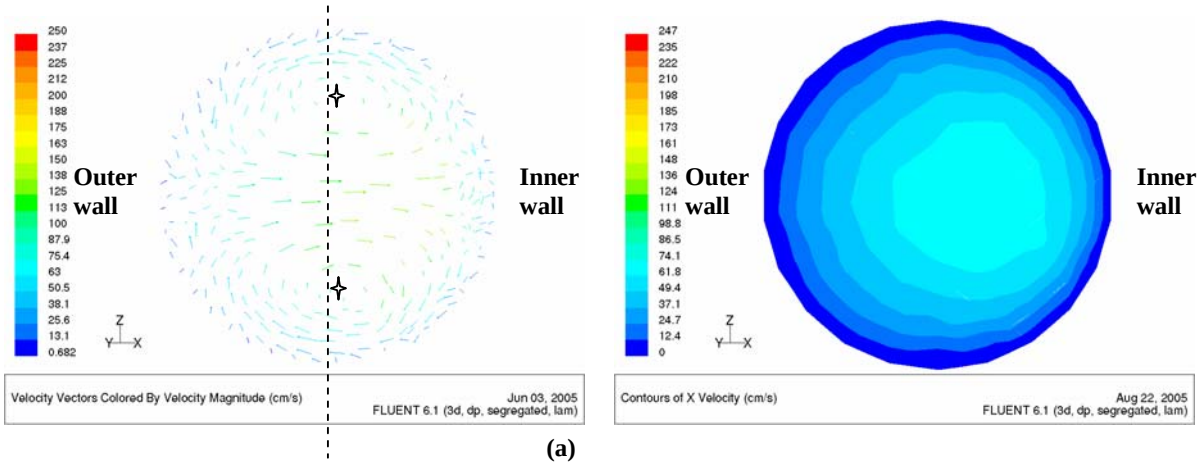

(a)

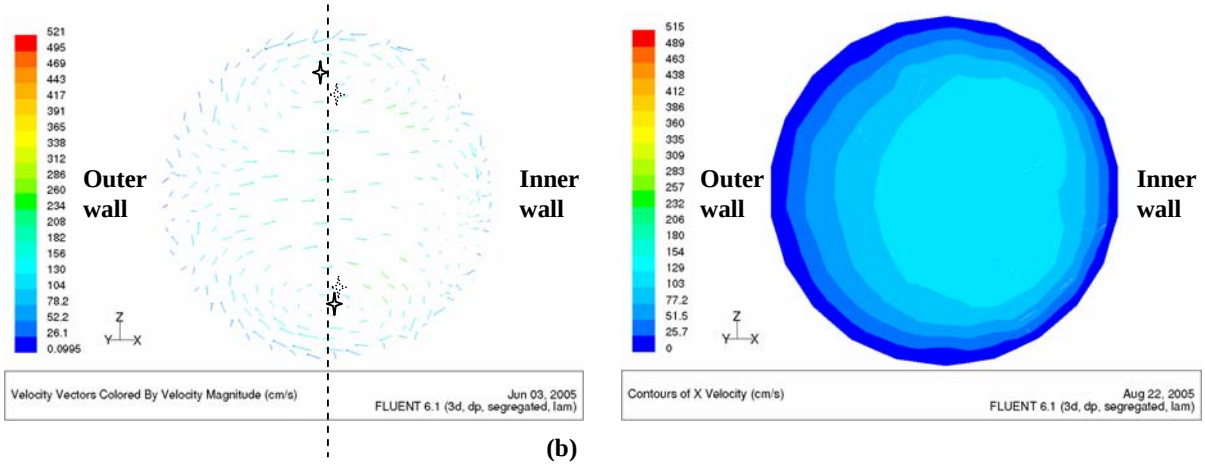

(b)

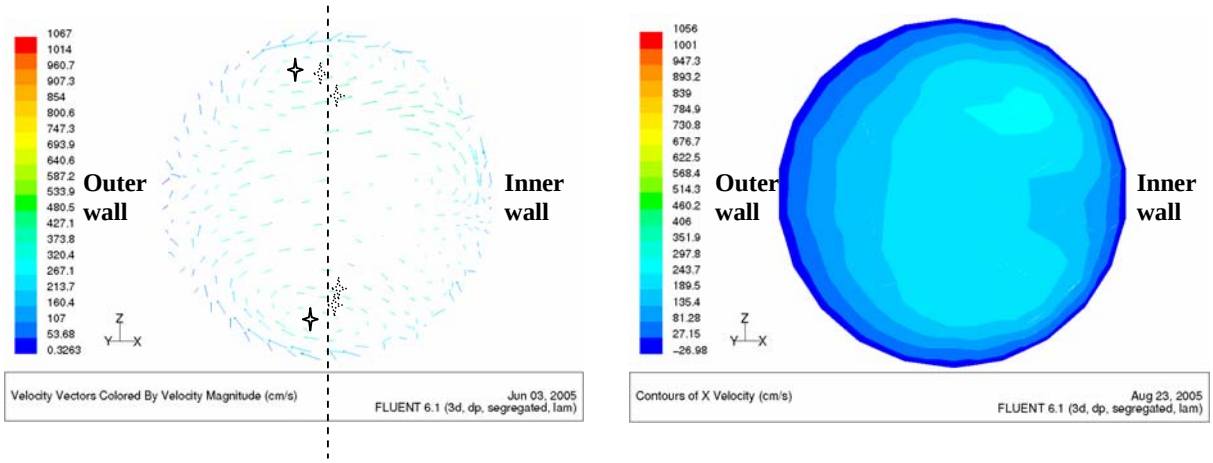

(c)

Fig. A.13: Velocity vectors and contours at g5-1-1 for C1 at (a) Re = 514, (b) Re = 1070, and (c) Re = 2194.

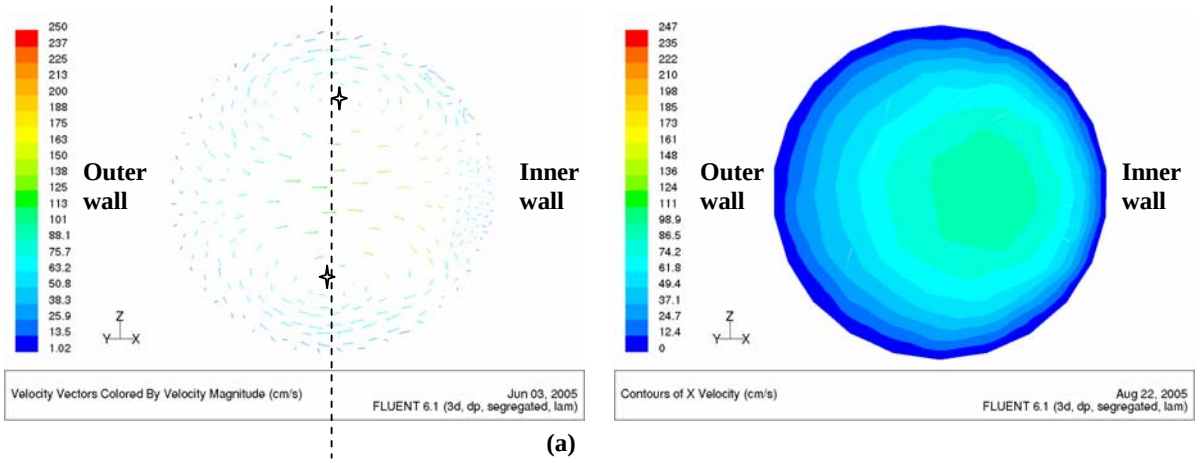

(a)

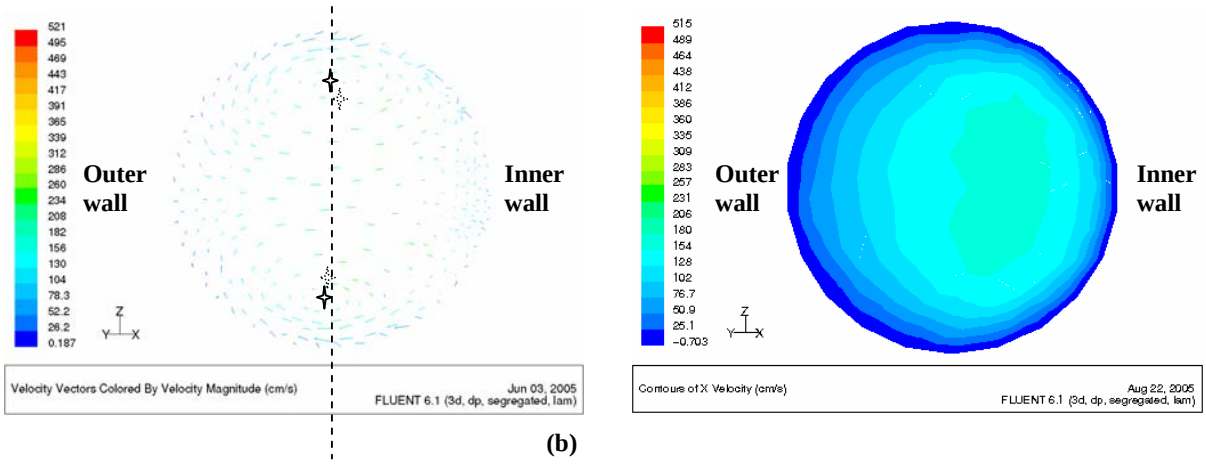

(b)

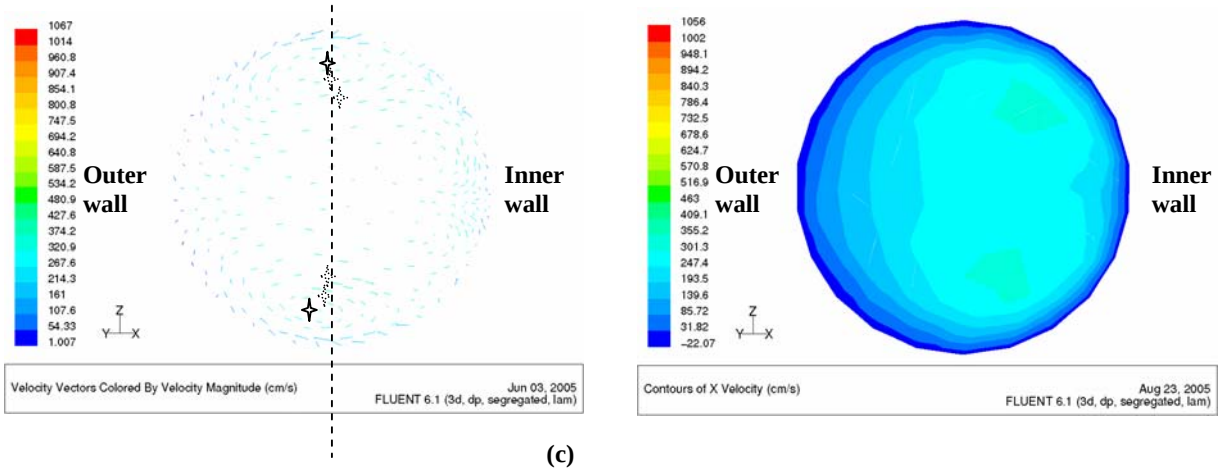

(c)

Fig. A.14: Velocity vectors and contours at g5-1-1 for C2 at (a) Re = 514, (b) Re = 1070, and (c) Re = 2194.

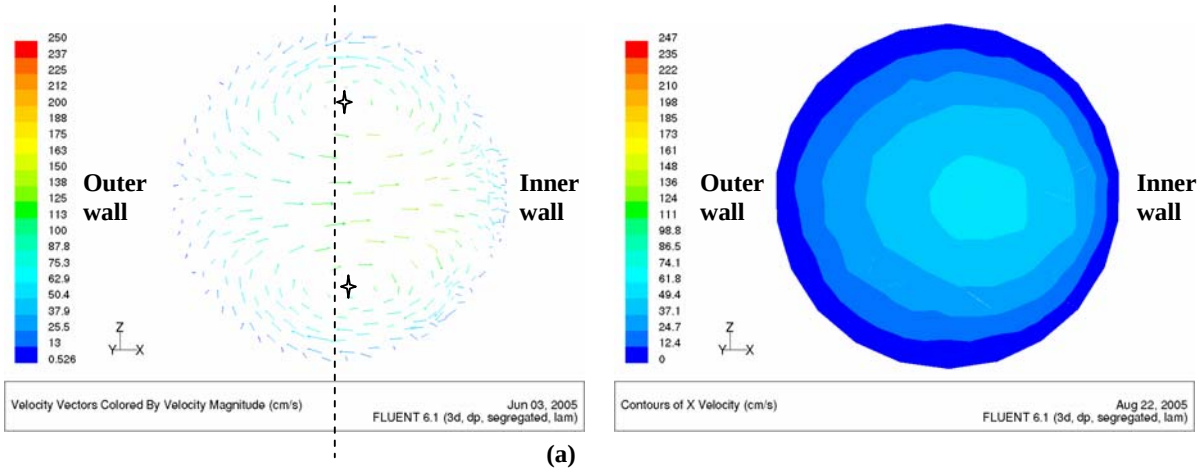

(a)

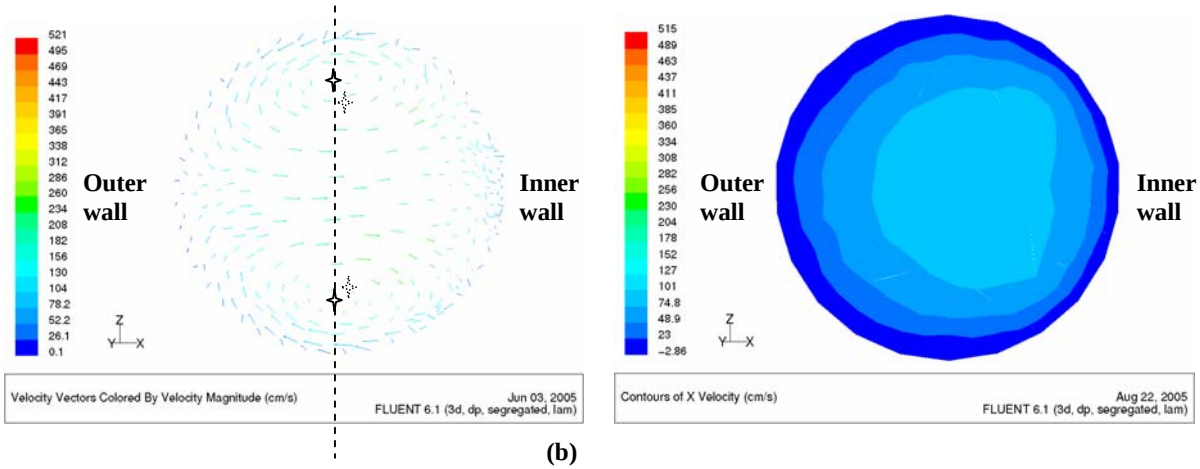

(b)

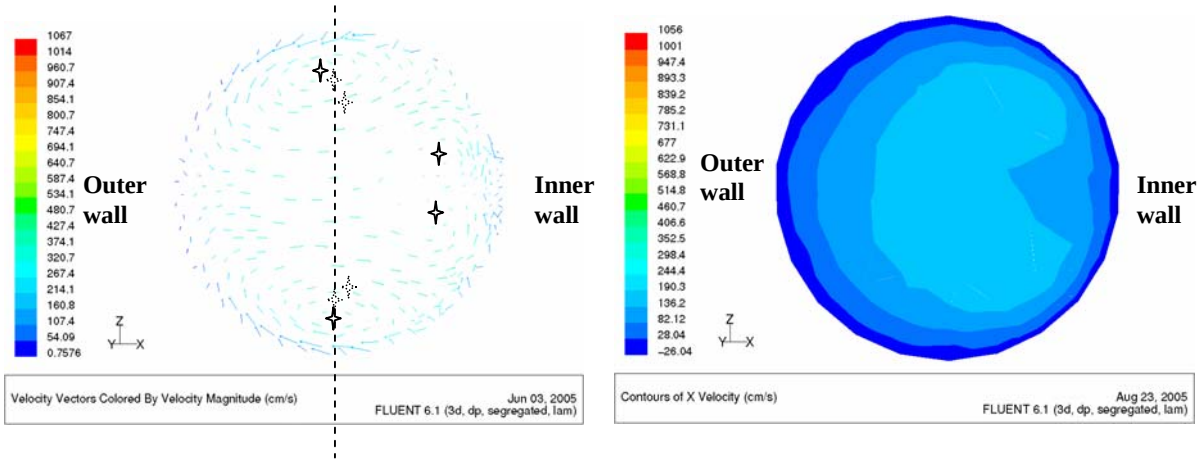

(c)

Fig. A.15: Velocity vectors and contours at g5-1-1 for C3 at (a) Re = 514, (b) Re = 1070, and (c) Re = 2194.

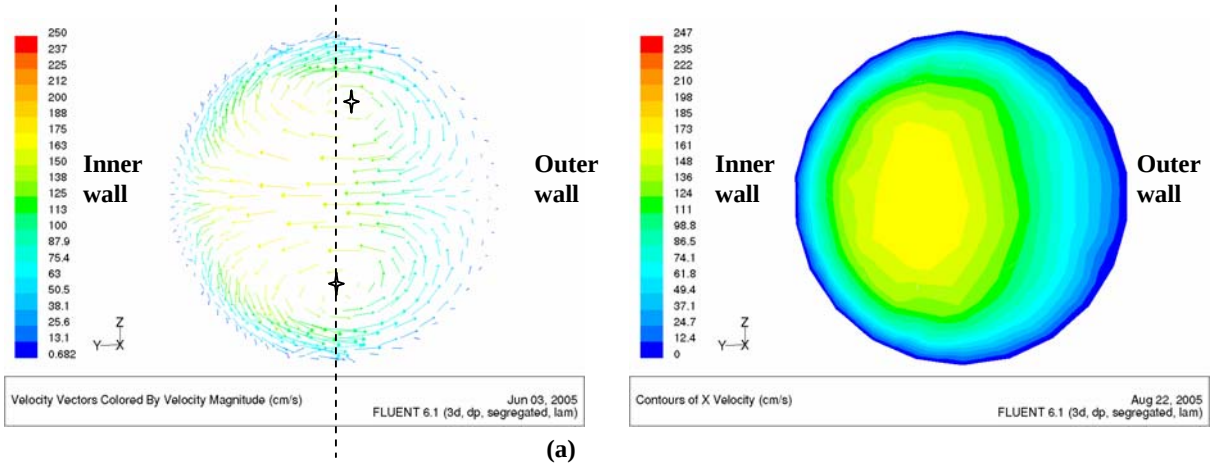

(a)

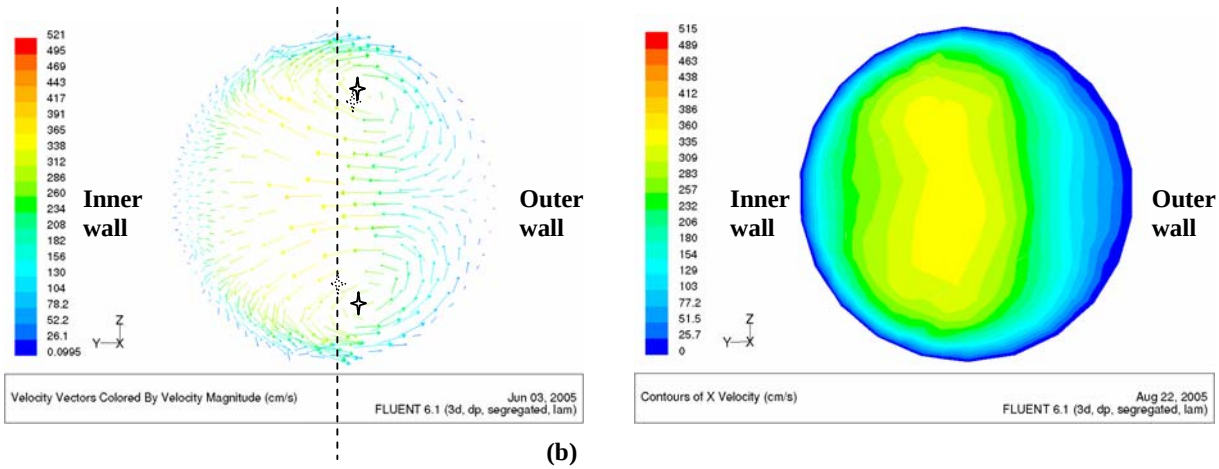

(b)

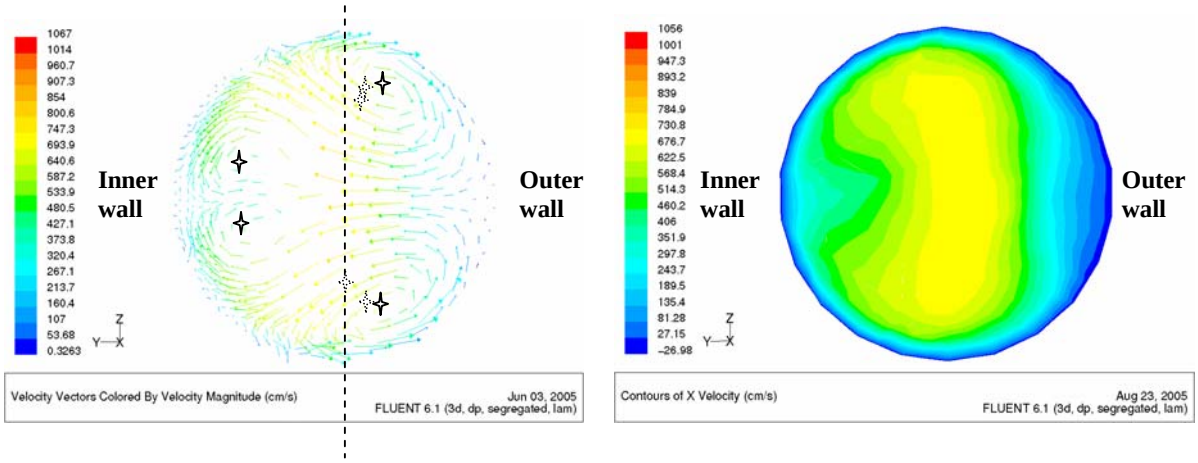

(c)

Fig. A.16: Velocity vectors and contours at g5-2-1 for C1 at (a) Re = 514, (b) Re = 1070, and (c) Re = 2194.

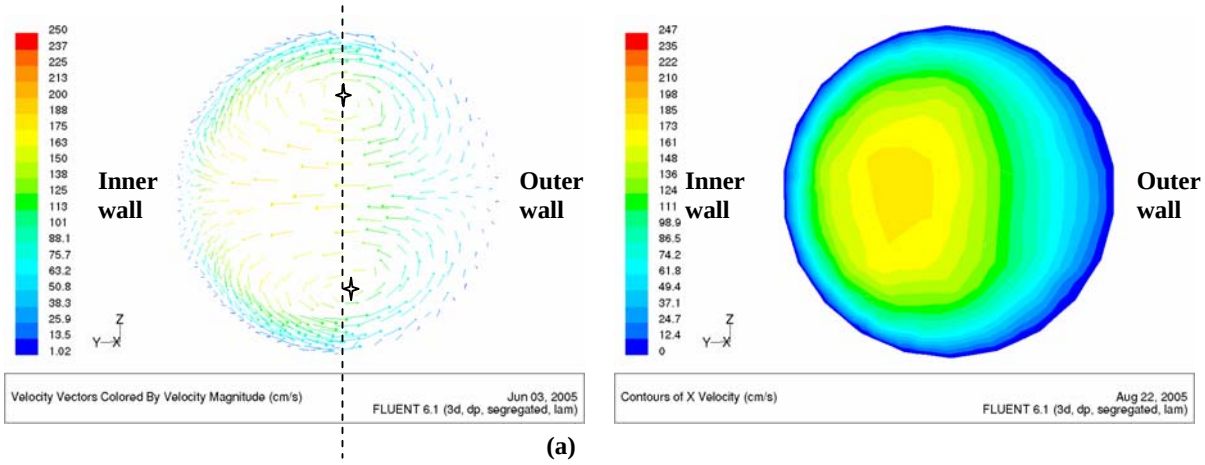

(a)

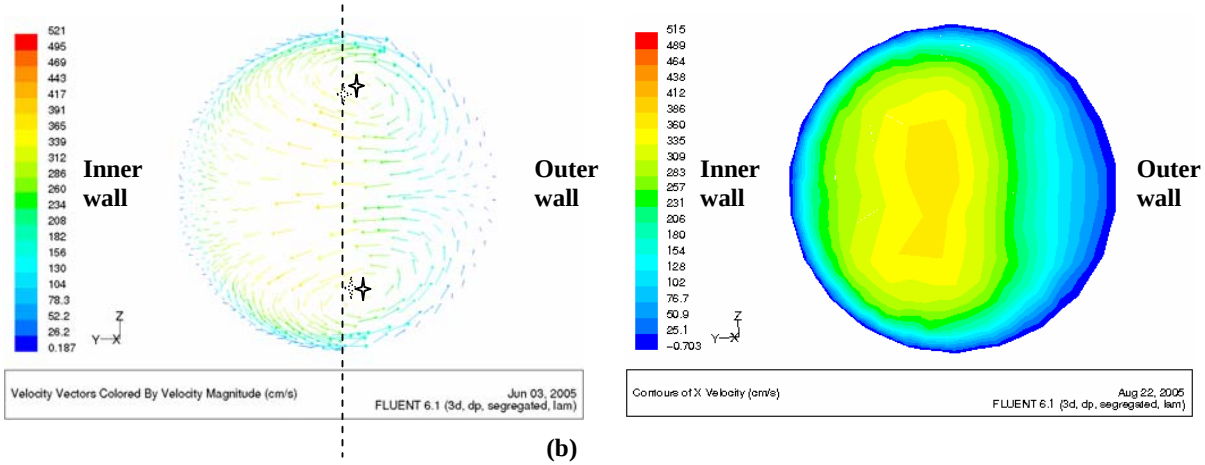

(b)

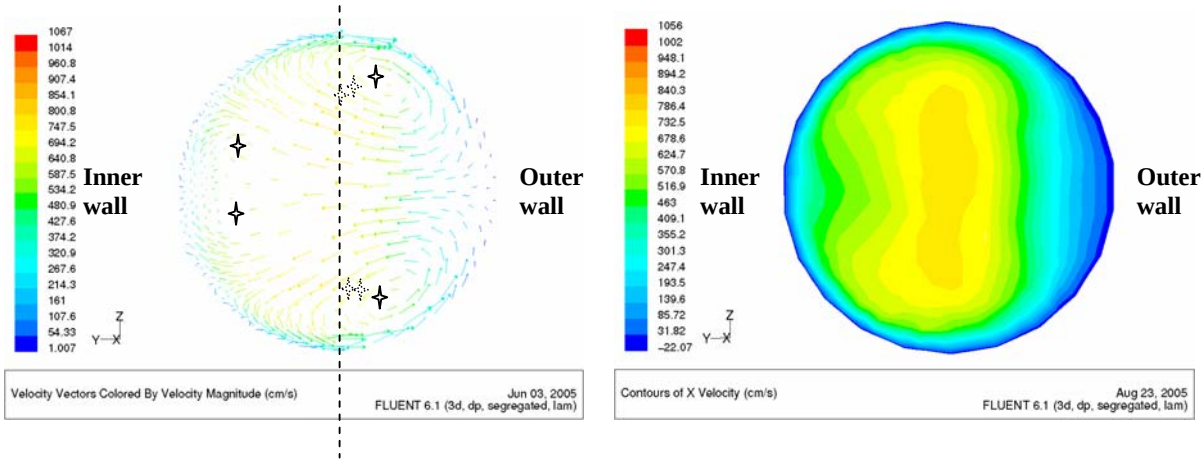

(c)

Fig. A.17: Velocity vectors and contours at g5-2-1 for C2 at (a) Re = 514, (b) Re = 1070, and (c) Re = 2194.

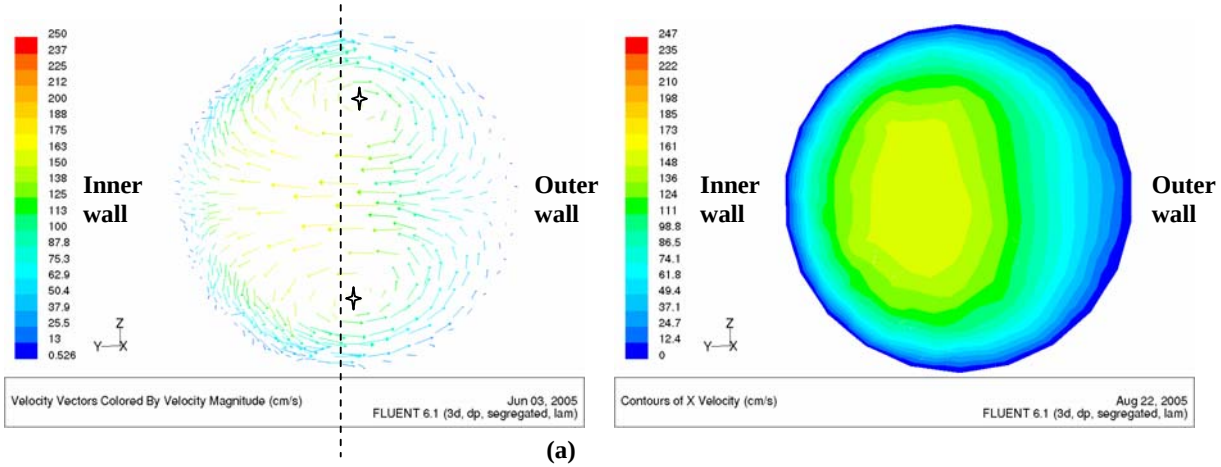

(a)

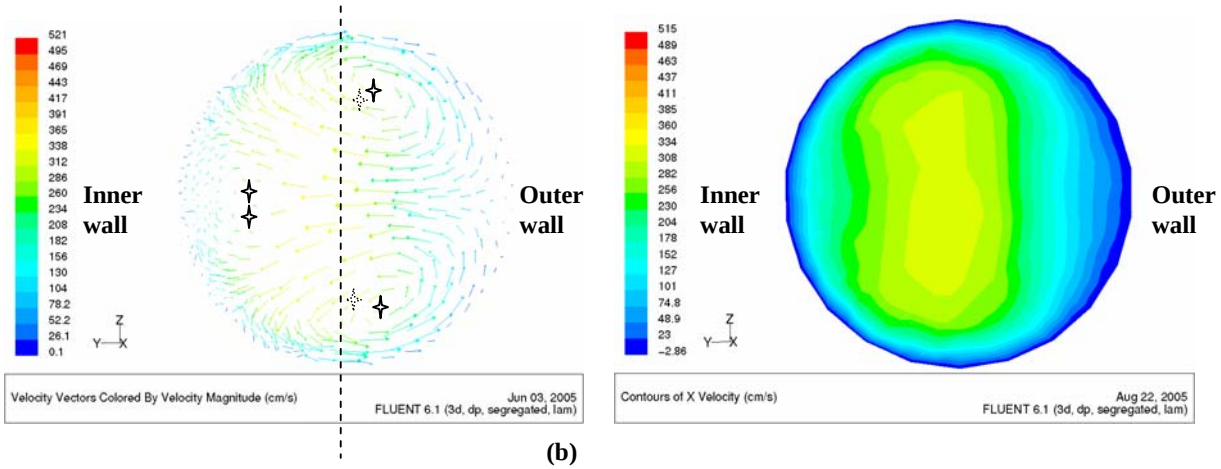

(b)

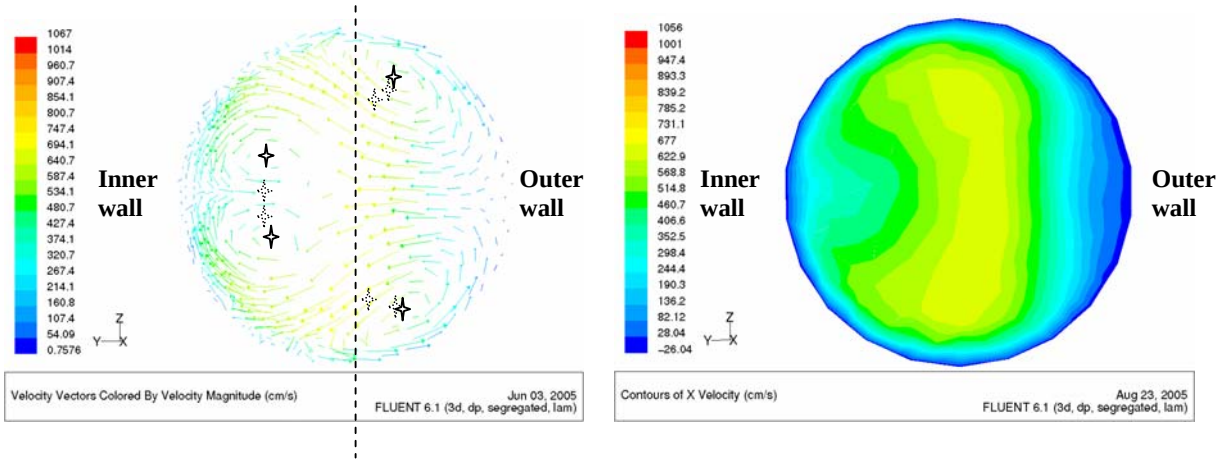

(c)

Fig. A.18: Velocity vectors and contours at g5-2-1 for C3 at (a) Re = 514, (b) Re = 1070, and (c) Re = 2194.

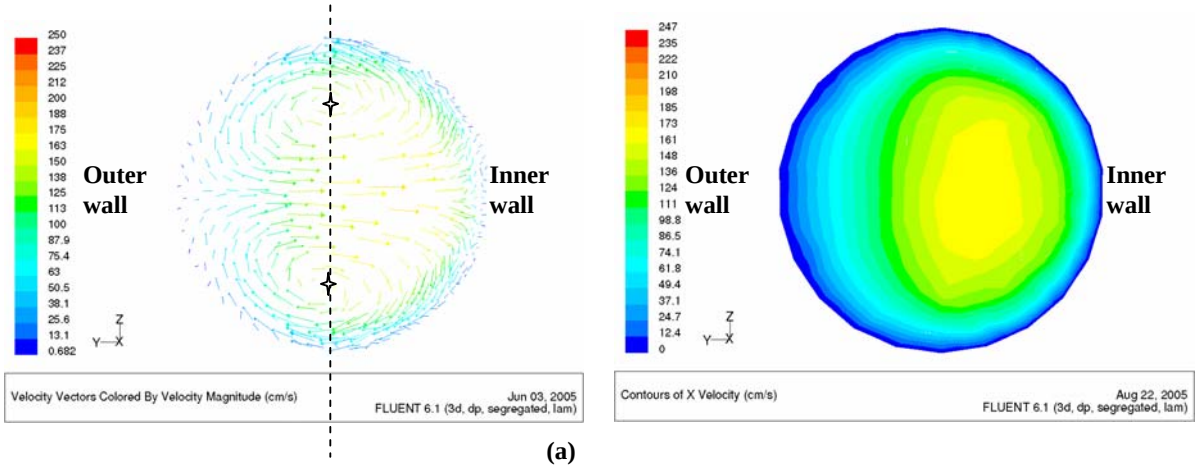

(a)

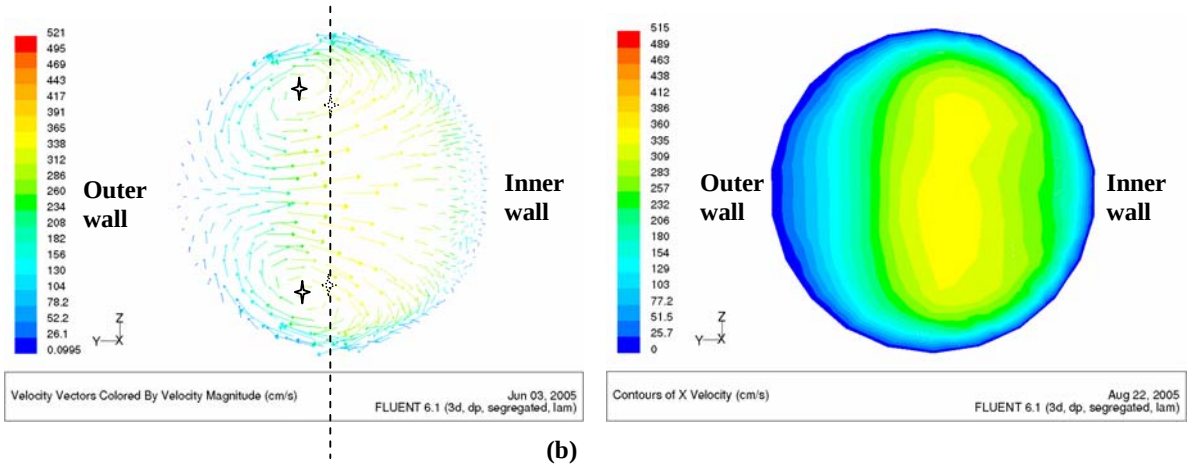

(b)

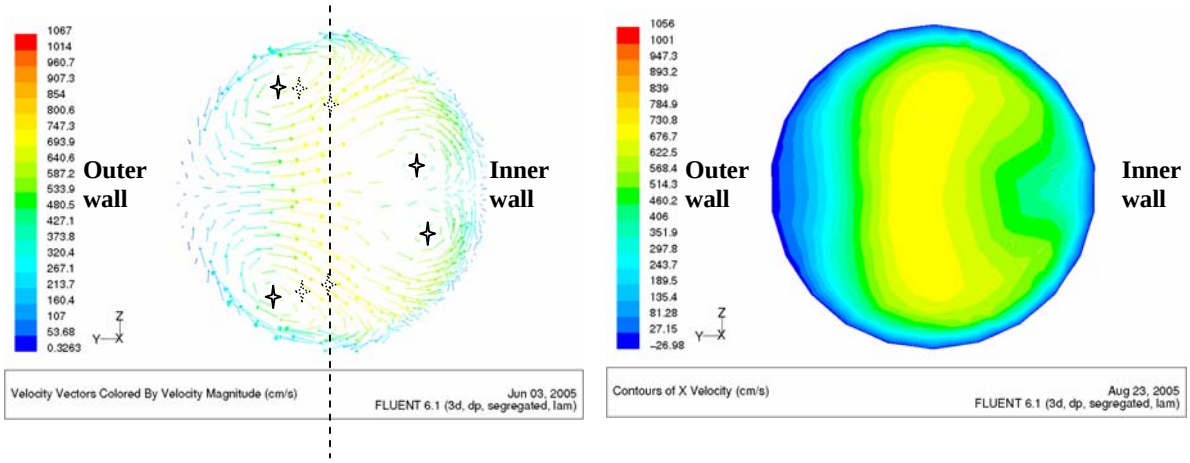

(c)

Fig. A.19: Velocity vectors and contours at g5-3-1 for C1 at (a) Re = 514, (b) Re = 1070, and (c) Re = 2194.

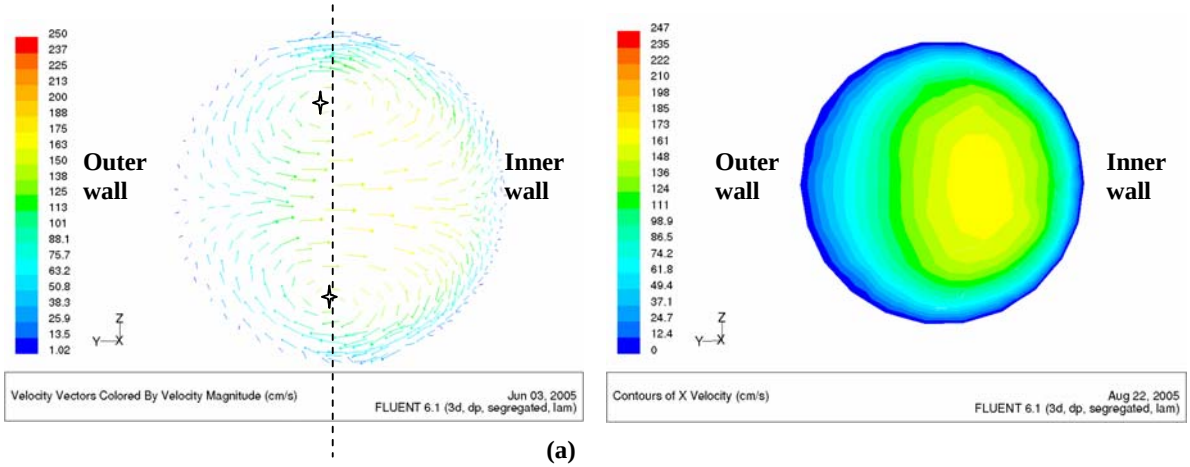

(a)

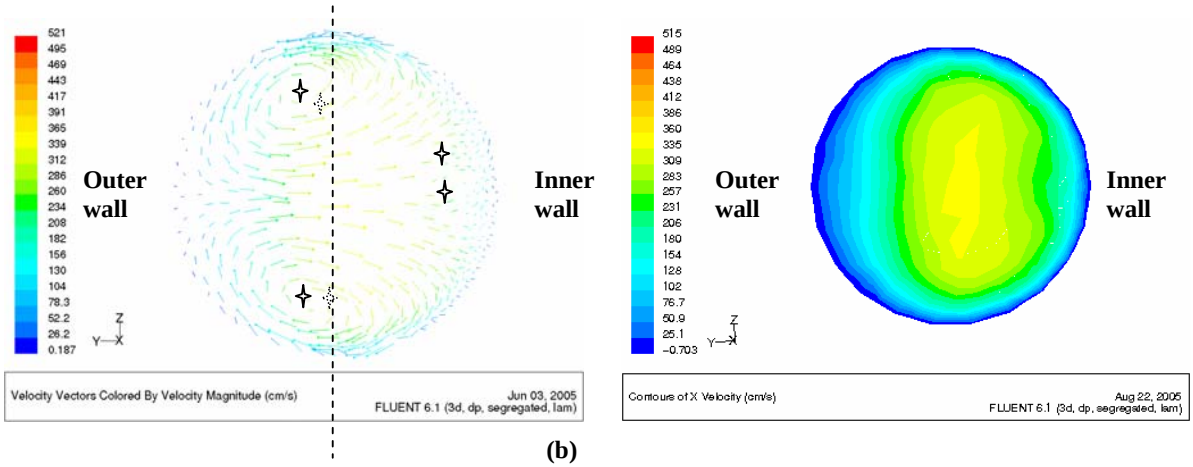

(b)

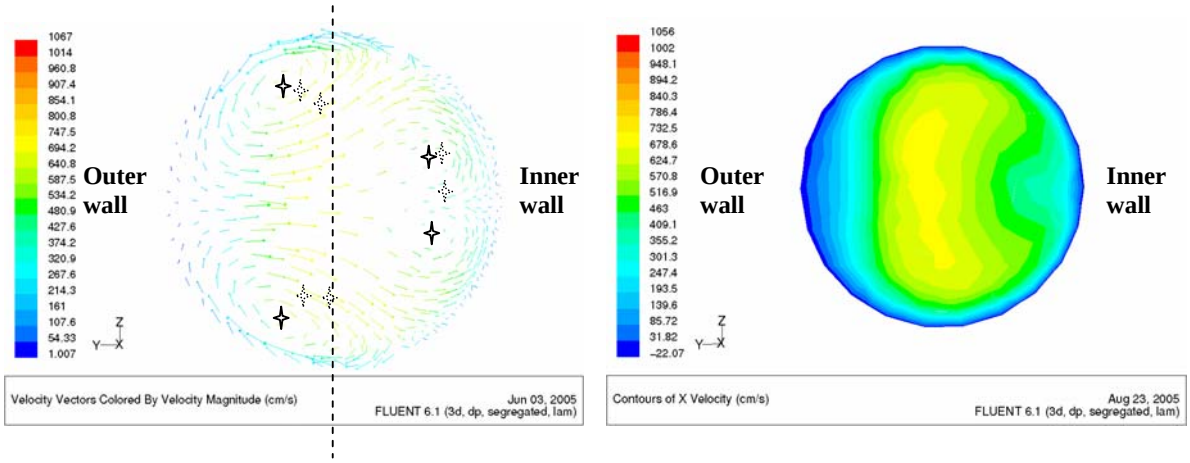

(c)

Fig. A.20: Velocity vectors and contours at g5-3-1 for C2 at (a) Re = 514, (b) Re = 1070, and (c) Re = 2194.

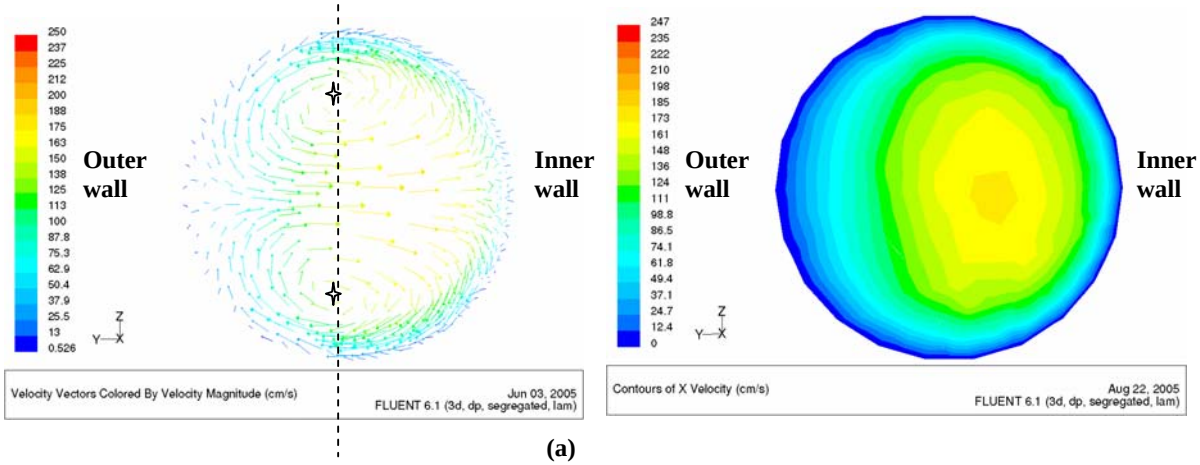

(a)

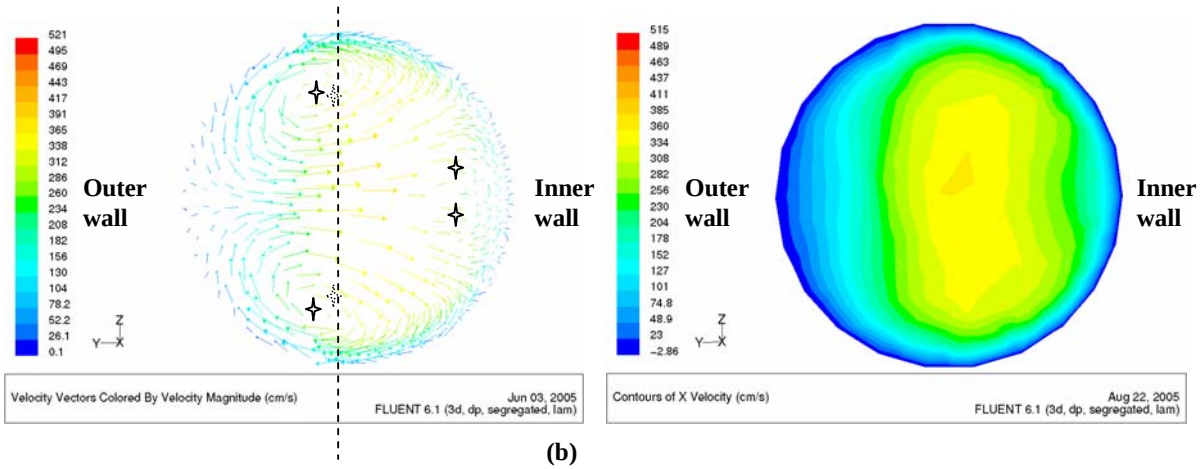

(b)

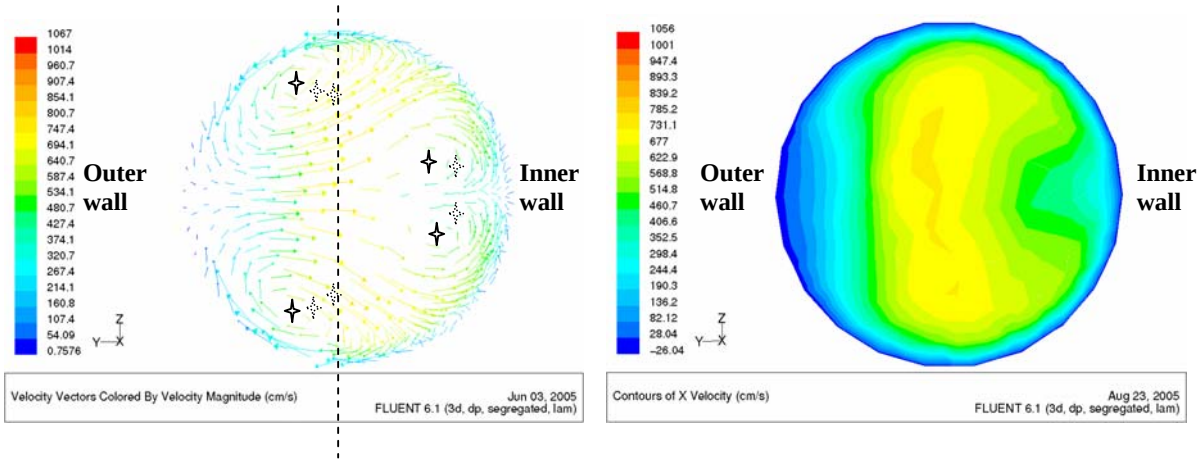

(c)

Fig. A.21: Velocity vectors and contours at g5-3-1 for C3 at (a) Re = 514, (b) Re = 1070, and (c) Re = 2194.

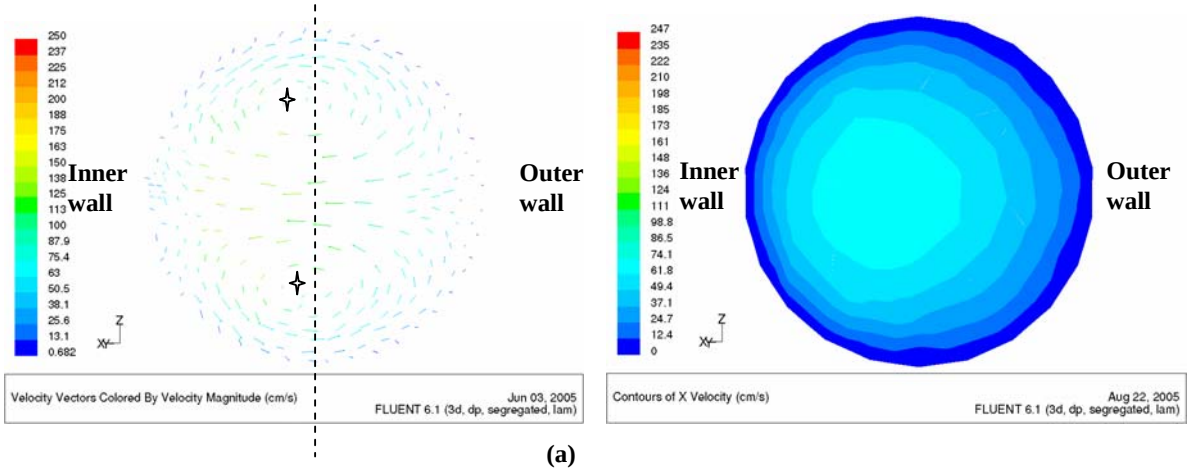

(a)

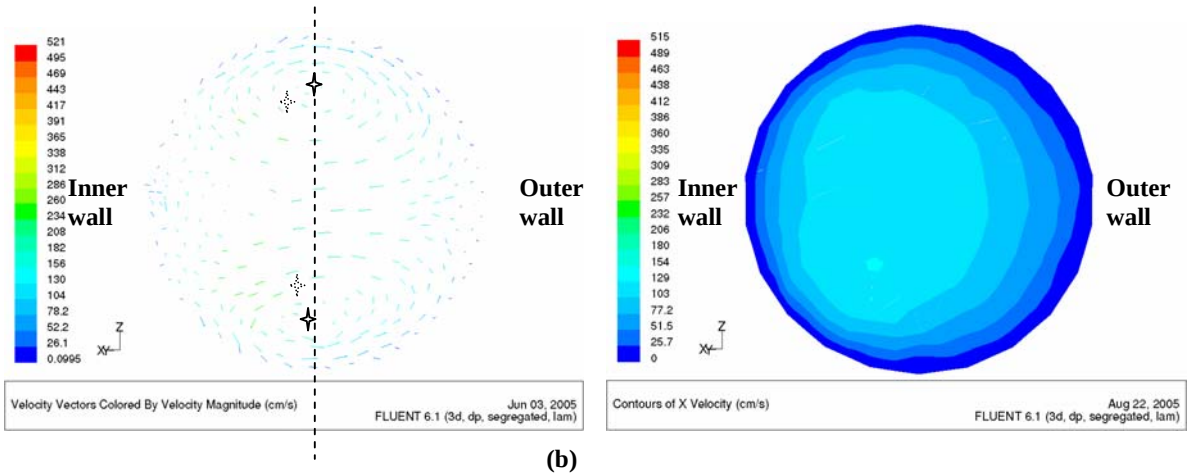

(b)

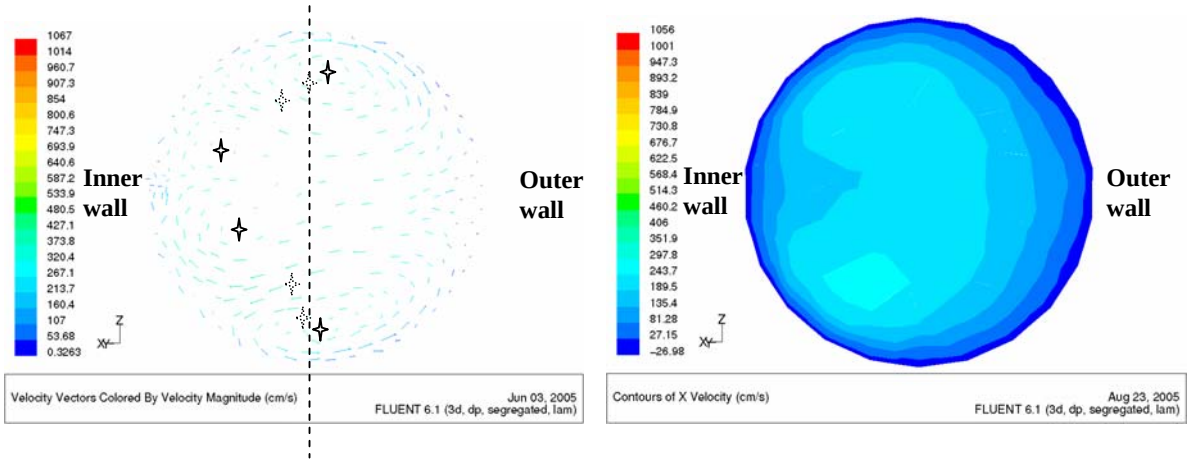

(c)

Fig. A.22: Velocity vectors and contours at g5-4-1 for C1 at (a) Re = 514, (b) Re = 1070, and (c) Re = 2194.

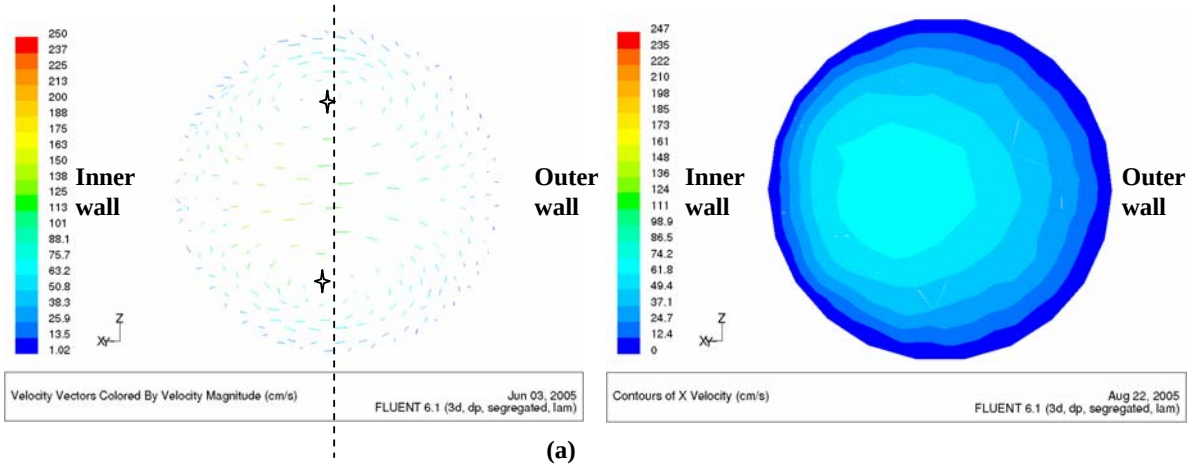

(a)

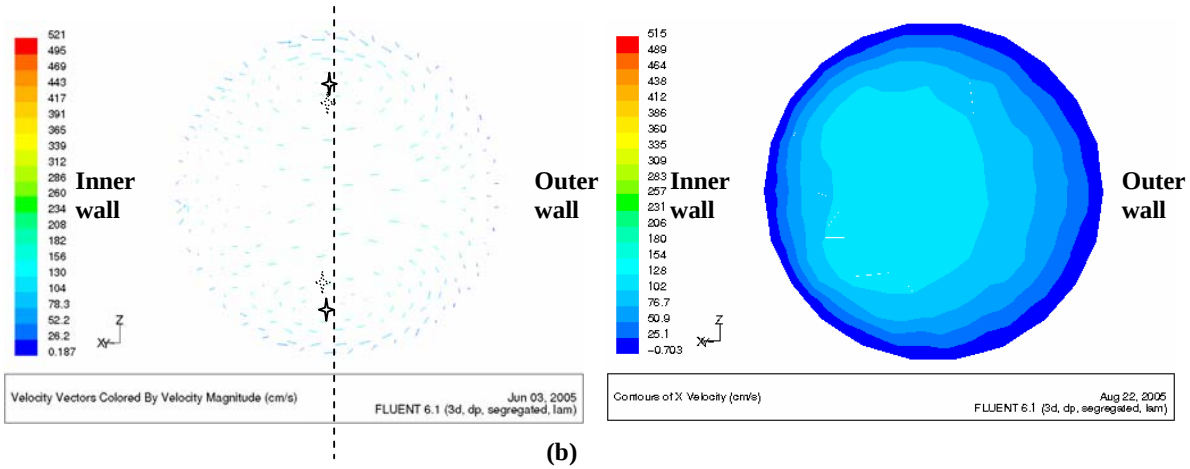

(b)

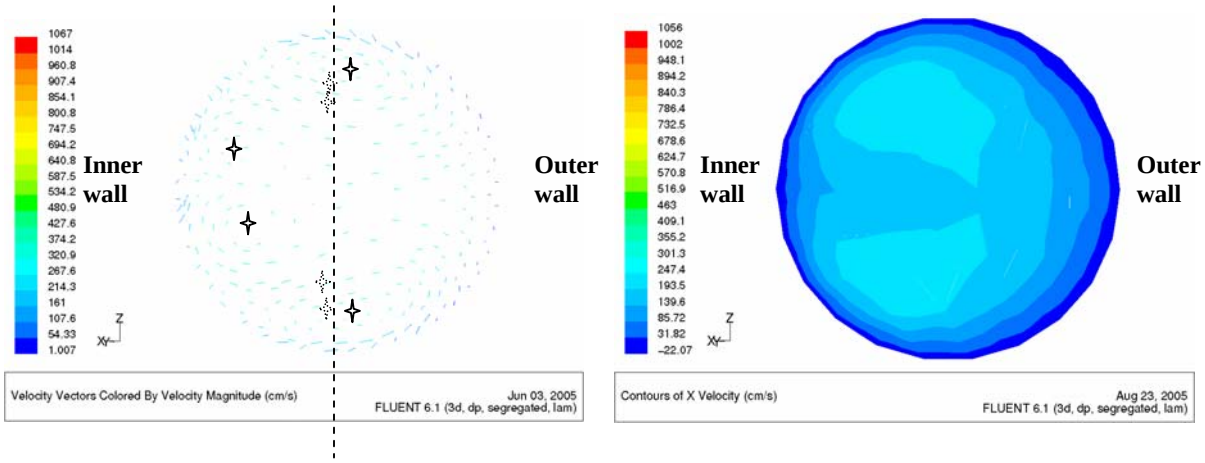

(c)

Fig. A.23: Velocity vectors and contours at g5-4-1 for C2 at (a) Re = 514, (b) Re = 1070, and (c) Re = 2194.

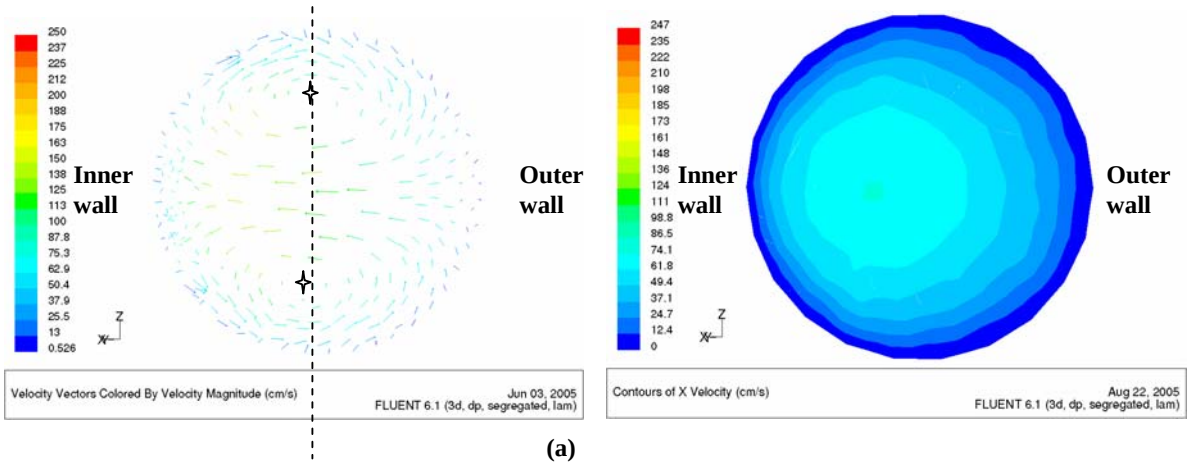

(a)

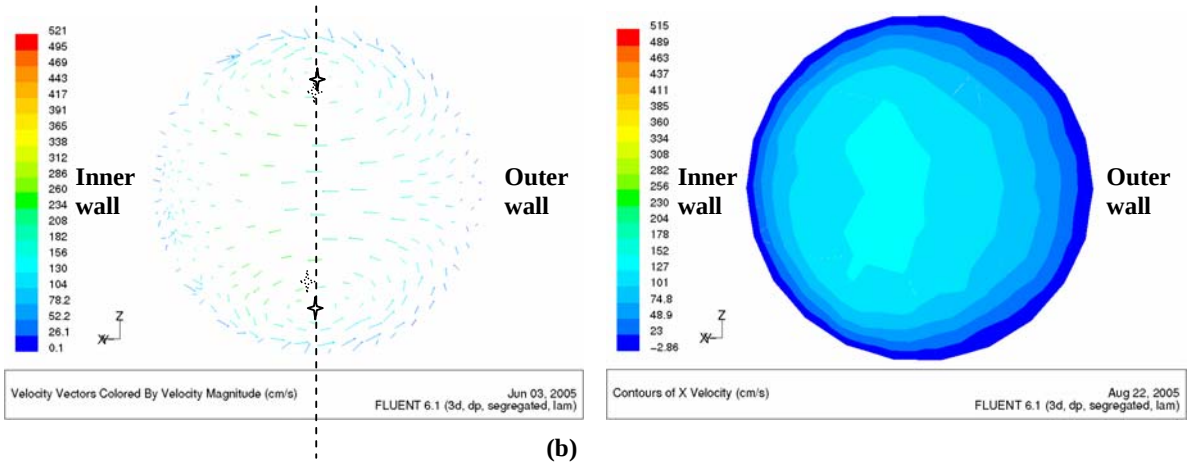

(b)

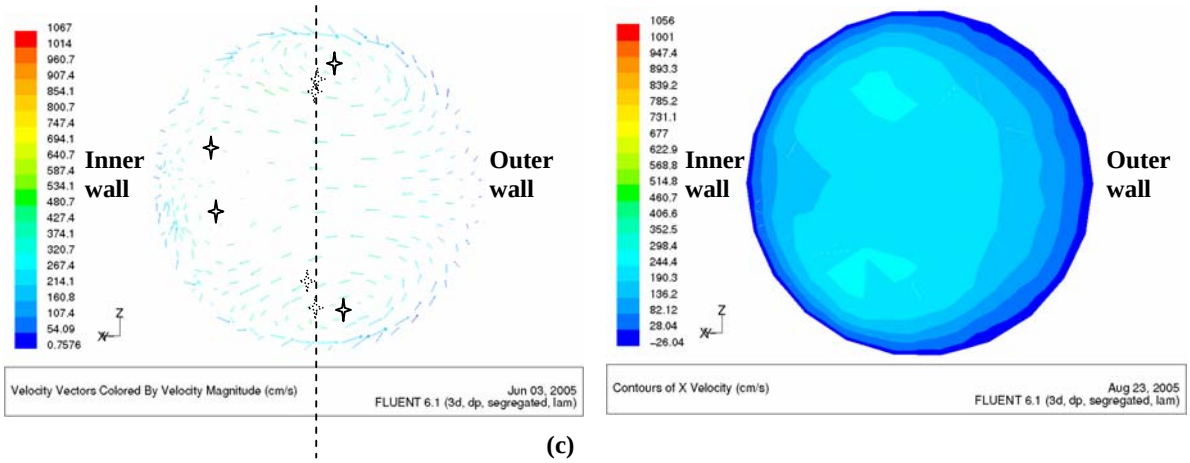

(c)

Fig. A.24: Velocity vectors and contours at g5-4-1 for C3 at (a) Re = 514, (b) Re = 1070, and (c) Re = 2194.